POLITECNICO DI TORINO

Ph.D in Electronics and Telecommunications Engineering
XXVII Cycle

Ph.D Thesis

GNSS Reflectometry for Land Surface Monitoring and Buried Object Detection

Supervisor:

Prof. Riccardo Notarpietro

Prof. Patrizia Savi

Candidate:

Yuekun Pei

December 2014

Abstract

Global Navigation Satellite System Reflectometry (GNSS-R) is attracting growing interest nowadays for several remote sensing applications. As a bistatic radar, the transmitter and the receiver are not co-located and in the special case of GNSS-R, the GNSS satellites are acting as transmitters and the receiver can be mounted either in a static position or onboard a aircraft or low orbit satellite. Various information about the surface from where the GNSS signals are reflected or scattered can be extracted by means of reflected signal strength, code delay, carrier phase delay, interference with direct GNSS signals and so on. Possible applications cover soil moisture retrieval, ice topography and thickness detection, snow depth estimation, vegetation coverage, sea state monitoring such as sea wind and surface roughness, sea salinity…

In this work, soil moisture retrieval was mostly focused on. Hardware including antennas and receivers was studied and designed. Our first strategy of soil moisture retrieval is to apply a single Left Hand Circular Polarization (LHCP) antenna for reflected signal reception. Therefore multiple types of antennas such as the helix antenna, the patch antenna and several commercial antennas were designed, simulated or tested in the anechoic chamber. Two receiver solutions were used in our group and both of them apply the SiGe GPS frontend. The first solution is a PC based one: the collection and store of the raw incoming reflected GPS signals were done by the NGrab software (designed by NAVSAS Group of Politecnico di Torino) installed in a standard PC. The other solution was developed in our group and it is operated by a single Hackberry board, which consists of power supply, storage subsystem and customized Linux Debian operating system. The light weight and small size enable this compact receiver to perform flight measurement onboard UAVs.

Both of the above mentioned receivers only store raw sampled data and no real time signal processing is performed on board. Post processing is done by Matlab program which makes correlations in both time and frequency domain with incoming signals using the local generated GPS C/A code replica. The so-called

Delay Doppler Map (DDM) is therefore generated through this correlation. Signal to Noise Ratio (SNR) can be calculated through Delay Waveform (DW) which is extracted from DDM at the Doppler frequency where the correlation peak exists. Received signal power can be obtained knowing the noise power which is given in a standard equation. In order to better plan a static measurement and to georeference specular points on the surface, programs for georeferencing specular points on either Google Maps or an *x-y* plane centered at the receiver position were developed. Fly dynamics in terms of roll, pitch and yaw influencing the antenna gain due to the variation of incident angles were also studied in order to compensate the gain to the received signal.

Two soil moisture retrieval algorithms were derived corresponding to two receiving schemes. The first one is for the receiving of only LHCP reflected signals. In this case, the surface is assumed to be perfectly smooth and the received signal is seen to consist of only coherent component caused by specular reflection. Dielectric constant can be retrieved from the processed SNR. Two measurement campaigns were carried out using this single LHCP system. The first campaign is a flight measurement overflown a big portion of rice fields when most of the fields were flooded. It was a test measurement on the SNR sensitivity to water/no-water surfaces and an attempt of dielectric constant retrieval was also performed. SNR showed good sensitivity to the surface water content and dielectric constant was also checked to be reasonable. The second campaign is in static positions and it includes two experiments. This campaign initially aimed at testing the sensitivity of the compact receiver to different surface moisture. Results of both SNR and retrieved dielectric constant showed to be coherent with the surface moisture changes.

The other retrieval algorithm is for the receiving of both LHCP and RHCP reflected signals concurrently. The cross polarization power ratio (LHCP/RHCP) is believed to be independent of surface roughness by several previous studies and this idea was also verified during the deriving process for either specular reflection case (only coherent component) or diffuse scattering condition (incoherent component). For diffuse scattering, three well known models were applied which are the Kirchhoff Approximation in stationary-phase approximation (Kirchhoff Geometrical Optics, KGO), Kirchhoff Approximation in Physical Optics

Approximation (KPO) and Small Perturbation Method (SPM). These three models cover different roughness surfaces from very rough (KGO) to slightly rough surfaces (SPM). All the derived results of cross polarization ratio for the three models were verified to be independent of surface properties and depend on only dielectric constant of soil and incident angle.

A new application of GNSS-R technique for the possibility of detection of buried objects was firstly investigated by our group. It has the potential use for man-made mines detection in the military field. Two measurement campaigns were carried out and the variation of the SNR level due to the presence of a metallic object was investigated. The first measurement campaign was performed in a static condition on a sandy terrain to check the functionality of the system. And the presence of the metallic object was detected also in the case of wet terrain. In the second measurement campaign, the antenna was moving along a given path and the possibility of detecting the object dimensions was highlighted. The results show the possibility of adopting this technique on board a remotely controlled UAV for metal object and even its dimension detection.

A measurement of snow depth attempting to relate it to reflected LHCP SNR is briefly presented and discussed in Chapter 7.

Acknowledgement

I would like to acknowledge all the support I have received during this research period, especially my supervisors: Riccardo Notarpietro and Patrizia Savi.

As my supervisor of Master of Science and Ph.D, Prof. Riccardo Notarpietro has given me the most support and guidance and without whom, this work cannot be done. He is firstly an open-hearted and energetic person who is also self-motivated, and these personalities encourage me and inspire me both for my study and life. Also as a scholar, he is creative and innovative and receptive of new ideas and advices.

Although Prof. Patrizia Savi has been my co-supervisor for only one year, I have known her since the beginning. She has a reputation for being kind and warm to students and I am fortunate to have the opportunity to carry on research with her. She is knowledgeable and resourceful and unlike the attitude to daily life, her requirement on research is high and strict. And her rigorous implementation of measurements is impressive and benefits me a lot.

I also want to show the deepest gratitude to my supervisors for their patience and forgiveness with the careless mistakes I have made and with the abstracted period I had.

My appreciation is also given to China Scholarship Council (CSC), which has supported me for the whole Master period and the first half of Ph.D. It provided me the opportunity to study abroad and supported me financially.

I am willing to extend the thanks to the regional project of SMAT-F2, which not only provided me the position of research fellowship, but also enables me to do the research in the relative field. And also to NAVSAS group, which has provided us several useful elements for the measurement instruments.

Last but not least, I'd like to thank all the excellent and intelligent members in our Lab: Sajid, Mubasshir, Yan and Muna, all my friends that care me and help me both here and home, all my families that never fail me and always trust me, and especially my wife, whose appearance has made my whole life ever lightful. Finally, I love everybody and this world.

Contents

List of figures

Chapter 1 Introduction

1.1 Global Navigation Satellite System

Global Navigation Satellite System, also known as GNSS, is a system with satellites that is used to provide autonomous geo-spatial positioning of a user's receiver anywhere in the world. It can be characterized as a highly precise, continuous, all-weather and near-real-time microwave (L band) technique with signals through the Earth's atmosphere. Each GNSS satellite continuously broadcasts radio signals in two or more frequencies in L-band (1-2GHz) with wavelength around 20 cm, the direct signals are used for navigation, positioning and timing [Jin, 2014].

Up to 2014, only the US's Global Positioning System (GPS) and the Russia's GLONASS are global operational GNSSs. China is also developing its own GNSS named Beidou Navigation System (BDS) to realize the global coverage by the year 2020. EU's Galileo positioning system is a GNSS that is scheduled to be fully operational by 2020 at the earliest. Besides, France, India and Japan are in the process of developing regional navigation systems.

1.2 GNSS-Reflectometry

GNSS Reflectometry is usually called for short as GNSS-R. Its main principle is to receive and further extract information from the GNSS signals reflected off the Earth surface. It works as a bistatic radar, in which the transmitter and the receiver are separated by significant distance, comparable to the expected distance to the target. The concept can be expanded that the receiver receives multiple signals simultaneously from different transmitters, in which case, it is multi static radar. General descriptions of GNSS-R and its principles and current applications are reported in these works: [Gleason, 2006], [Jin, 2010], [Cardellach, 2011], [Jin, 2011].

Comparing with the other existing remote sensing tools, GNSS-R has several

advantages:

- No additional transmitters are used, therefore the whole system consisting of only the receiver enables to be small size and low cost.
- Plenty of available signal sources, considering all the signals transmitted by satellites belonging to the above mentioned GNSSs.
- Applied L band signals have good penetration through atmosphere and are optimal for several applications, and the global coverage of GNSS satellites provides the technique to be nearly all-time and all weather condition operational.
- Wide range of applications can be achieved, such as soil moisture retrieval, sea state monitoring, ice topography and thickness detection and snow coverage study.

1.3 Soil moisture remote sensing with GNSS-R

Several active and passive remote sensing techniques operating in the microwave region of the electromagnetic spectrum have been developed, to monitor different important geophysical land parameters such as the soil moisture and the vegetation biomass. The importance of the soil moisture information as a desired input for several applications such as hydrology, climatology and agriculture has been well recognized. Soil moisture is a key component of the water cycle. It directly influences the amount of evaporation, infiltration, runoff, and the amount of water uptake by plants. Soil moisture creates energy fluxes between the land and the atmosphere, which impacts weather systems and may affect large populated areas. Moreover, the accurate monitoring of soil moisture serves as a factor in hydrological and vegetation monitoring and for better seasonal forecasting. However, it is often a lack parameter for numerous whether prediction models, since the monitoring of large area surface water resources is generally impractical via in situ observations, because of the large number of sites required and the high cost of monitoring equipment. Soil moisture influences the dielectric constant (i.e. relative permittivity) of the soil medium, and therefore it can be measured through signal reflection and surface emission. Due to these reasons, ground based, airborne and spaceborne remote sensors such as radiometers and radar systems

(scatterometers) for soil moisture investigation have been widely studied based on measuring dielectric constant of the soil. The monostatic radar systems measure rough surface backscattered signals and also derive soil moisture from the backscatter cross section, which is a function of the soil dielectric constant, incident angle and roughness. However, monostatic radars are generally less sensitive to soil moisture than radiometers due to the surface roughness affects.

Several airborne campaigns and ground based field experiments have proven that radiometers operating at L band are highly sensitive to soil moisture due to the large contrast between the dielectric constant of soil minerals and water. The work done by [Njoku, 1982] and [Wang, 1980] showed that L-band frequencies are optimal for sensing soil moisture in the top 0-2 cm surface layers, thanks also to the reduced atmospheric attenuation and better penetration of vegetation.

The Soil Moisture and Ocean Salinity (SMOS) mission of the European Space Agency (ESA) is an unprecedented initiative to globally monitor surface soil moisture using a novel 2-D L band interferometric radiometer concept, which senses the soil emissivity [Piles, 2010]. NASA also launched its own Soil Moisture Active Passive mission (SMAP), with onboard a radiometer and synthetic aperture radar operating at L band (1.20-1.41 GHz). The instruments are designed to make coincident measurements of surface emission and backscattered power, with the ability to sense the soil conditions through moderate vegetation cover.

GNSS-R as an Earth's surface remote sensing tool has been widely studied for various applications. More recently, soil dielectric constant and soil moisture retrieval have started to produce some results. Three different observing strategies were implemented for this kind of applications [Wan, 2012]:

(1) Multipath effect and its relation to soil moisture (see Figure 1-1 (a)): it uses a standard ground based nearly hemispherical RHCP antenna, to receive direct signal. The reflected signal originated from ground creates multipath effects, since it interferes with the direct signal. The total received signal amplitude has a sinusoid behavior with the change of sine of elevation angle (sin(E)). By measuring the received signal to noise ratio it is possible to retrieve soil moisture information [Zavorotny, 2010], [Larson, 2010].

(2) Interference Pattern Technique (IPT) (see Figure 1-1 (b)): usually a horizontal-pointing vertically polarized (VP) antenna is employed. This technique

consists of the measurement of the power fluctuations related to the signal resulting from the simultaneous reception (and interference) of the direct and the reflected GNSS signals. It is something similar to a multipath effect. In this case the two rays approach is adopted. Soil moisture retrieval is based on finding a specific 'notch' point from the interference pattern, versus satellite elevation ([Mironov, 2012(a)], [Mironov, 2012(b)], [Rodriguez-Alvarez, 2009], [Rodriguez-Alvarez, 2011(a)]).

(3) Bi-static method: this is based on the separate reception of direct and reflected signals using two different antennas and on the separate measurement of signal powers. Depending on the antenna configuration, three possible observing systems exploiting the bi-static geometry can be further identified:

(3.a) A down-looking LHCP antenna and an up-looking RHCP antenna (Figure 1-1 (c)): a LHCP antenna receives reflected GPS signal from the surface. The power reflectivity could be obtained either by using a bi-static radar equation [Masters, 2004] or from the power ratio between the reflected signal and the direct signal [Katzberg, 2005]. The reflectivity is then a function of dielectric constant of the soil, the elevation angle and the surface roughness. By properly choosing the surface roughness parameter (elevation is known from the direct signal) for a certain scattering model (see for example [Ulaby, 1982]) such as the Small Perturbation Method (SPM) and Kirchhoff Approach (KA), the dielectric constant can be retrieved.

(3.b) One RHCP up-looking antenna and two down-looking antennas with one RHCP polarized and the other LHCP polarized [Zavorotny, 2000(a)], [Egido, 2012], [Pierdicca, 2011] (Figure 1-1 (d)). With this configuration, it is possible to measure both the co-polar component of the terrain reflectivity, using LHCP signal, and the cross-polar component, using the RHCP antenna. The ratio of these two reflectivities was verified to be in good correlation with soil moisture and it was independent on the surface roughness.

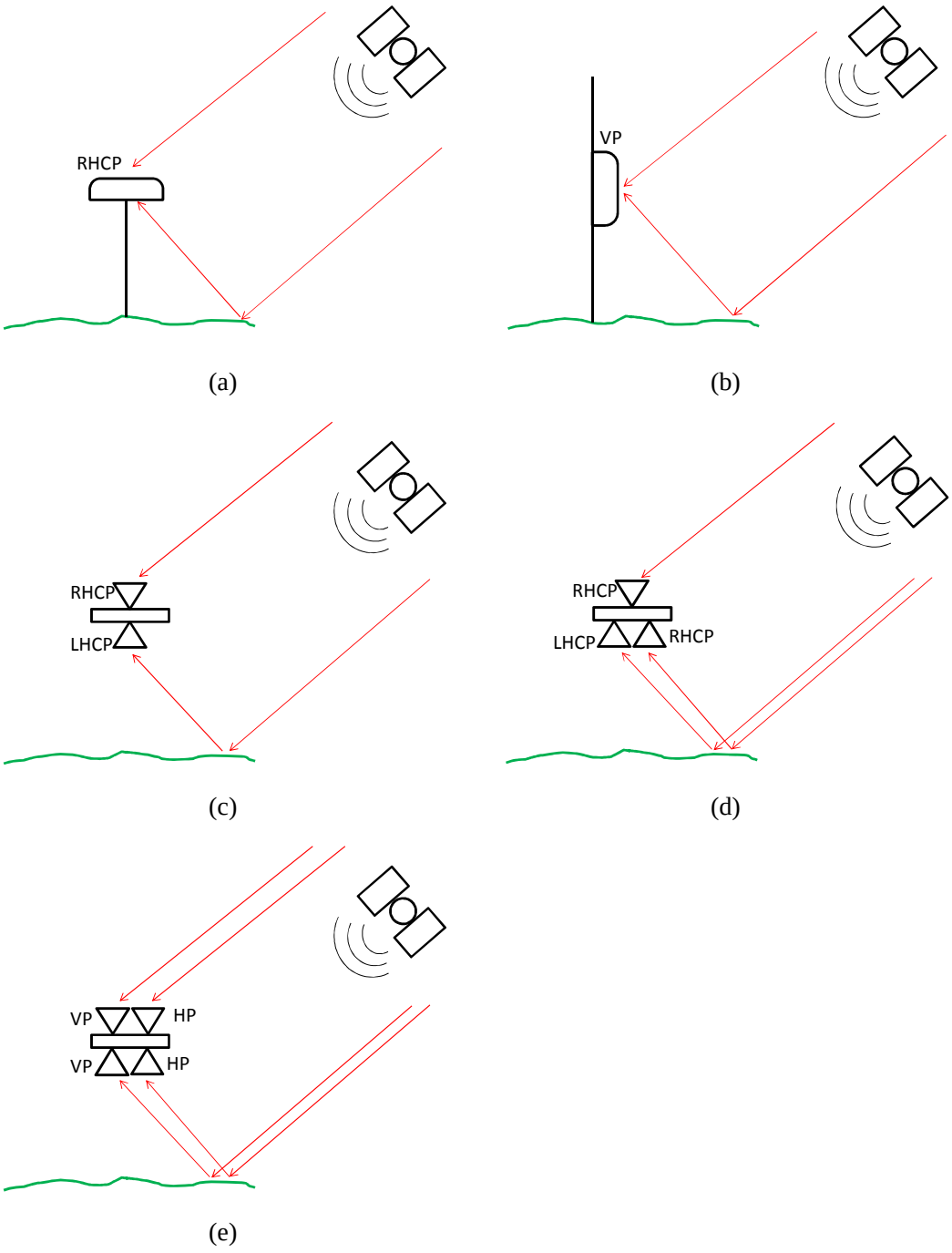

Figure 1-1 System schemes for different observing strategies

(3.c) A similar configuration to the one described in (3.a) but with vertically and horizontally polarized (HP) antenna for both the up and down-looking (Figure 1-1 (e)): this configuration was not specifically proposed for GNSS-R, it can be applied for a general bistatic radar measurement and therefore, it's also available

here. Simulation studies were given by [Ceraldi, 2003], [Ceraldi, 2005]. The ratio between the reflected and the direct power on the H polarization and the same ratio on the VP depend on the soil reflectivity on both the HP and VP and on surface roughness. If the power ratio between the two channels with orthogonal polarization is considered, the influence of the surface roughness cancels out. It was verified that the final expression holds under different scattering models, which means that it could be applied under a wide range of surface roughness. This dielectric constant retrieval approach is based on the use of the ratio of power densities scattered at *hh* and *vv* polarizations along the specular direction for different incident angles. Since the ratio is a function of both the elevation angle and the dielectric constant, a minimum least square technique was applied to better define the dielectric constant, by measuring at two different elevation angles at least.

The retrieval of the soil moisture from the dielectric constant at microwave band (especially in L band) has been widely investigated and several well accepted theoretical and empirical models have been established, such as [Wang, 1980], [Mironov, 2009], [Hallikainen, 1985] and [Dobson, 1985]. The information of soil texture in terms of percentage of clay and sand should be known and provided in input to such models. A further model described by [Topp, 1980] does not depend on any input information, since it models the relative permittivity as a third order polynomial function of soil moisture.

1.4 Other applications with GNSS-R

Apart from the application of soil moisture retrieval using GNSS-R, the technique was actually first used for the sea state monitoring, since [Hall and Cordey, 1988] proposed to use Earth reflected GNSS signals as a mean of sensing the ocean surface. The concept has been put forward as an alternative technique for ocean altimetry by scientists at the European Space Agency [Martin-Neira, 1993]. Later, the same principle was demonstrated as a useful tool to sense ocean roughness by [Garrison et al, 1998].

Comparing with other conventional scatterometers, the GNSS-R technique allows the receiver hardware to be small size, low cost and simplicity of design.

The work carried out by [Garrison, 2000] is to collect GPS reflected data over ocean on aircraft and on a balloon at altitudes of up to 25 km, and to study the relationship between the sea wind speed and the cross correlation shape of the received signal. [Zavorotny, 2000(b)] also did research in sea wind and developed a theoretical model which is based on a bistatic radar equation derived using the geometric optics limit of the Kirchhoff approximation. Other work has been done based on airborne instruments for sea wind and roughness study [Rius, 2002], [Garrison, 2002], [Cardellach, 2003], [Gleason, 2005], [Marchán-Hernández, 2008].

Altimetry is also an application that has been developed to provide measurements of ocean and ice sheet topography. [Katzberg, 1996] utilized GPS receiver and downward-point antenna for receiving ocean scattered signal to remove the effects of ionospheric delay to the satellite carried single frequency altimeter. [Martin-Neira, 2001] presented the PARIS concept and an original experiment on sea surface altimetry using GPS-reflected signals. The following study on sea surface altimetry was basically applying GPS-reflected signals [Lowe, 2002], [Ruffini, 2004], [Cardellach, 2008], [Helm, 2008], either based on code phase or carrier phase delay. Recently, [Dampf, 2013] realized the altimetry measurement based on Galileo E1/E5a/E5b signals, and achieved very accurate surface height results, thanks to the unique Galileo signal modulation code.

Snow thickness monitoring is another topic which can apply GNSS-R. As the snow thickness is related to the amplitude of the reflected signal as a function of the incident angle or relative amplitudes between different polarizations, the snow thickness can be retrieved from the GNSS reflected signals. [Gutmann, 2012] applied a GPS interferometric reflectometry method to monitor the snow depth, and the test results showed strong agreement between GPS snow depth estimates, a continuously operating scanning laser system and an airborne light detection and ranging (LIDAR) measurement. The work done by [Rodriguez-Alvarez, 2011(b)] used the Interference Pattern Technique (IPT) and a ground based reflectometer to study the snow effects, and developed an algorithm for the snow thickness.

Vegetation canopies have properties to attenuate microwaves and this effect has been widely studied for decades. Earlier studies such as [Ulaby, 1982] and [Ulaby, 1985] modeled the attenuation effect, and recent GNSS-R measurements were

carried out to study the relationship between the reflected signal strength and vegetation coverage attenuation in order to sense the vegetation growth. [Small, 2010] applied the GPS multipath technique and found out that vegetation height and water content are inversely correlated with the magnitude of ground reflected multipath. The work done by [Rodriguez-Alvarez, 2011(c)] using the IPT technique and the measurement of [Egido, 2012] with the bistatic radar equation method also gave their contributions to the vegetation coverage research.

Chapter 2 Basic principles of GNSS-R

2.1 GNSS signals

The basic principle of GNSS signals is to allow the user (receiver) to calculate the range between the receiver and the satellite at the time the signal is transmitted, and also receive the navigation message that is modulated to the carrier, including the ephemeris data, used to calculate the individual GNSS satellite in orbit at the time of signal transmission and the almanac data with the information about the time and status of the entire satellite constellation. The receiver requires to receive at least four GNSS satellites' signals simultaneously and to calculate the 3 dimensional positions of these four satellites, in order to solve its own position consisting of three unknown coordinates of position and one unknown time error between the receiver and the GNSS. This method, known as Pseudorange, compares the transmission delay between the received code with its locally generated replica.

Generally, GNSS applies a CDMA (Code Division Multiple Access) spread-spectrum technique where the low bit rate message data is encoded with a high rate "pseudo random noise" (PRN) sequence which is unique for each satellite. The PRN is a signal similar to noise which satisfied one or more of the standard tests for statistical randomness. Although it seems to lack any definite pattern, PRN consists of a deterministic sequence of pulses (1 and 0) that will repeat itself after its period. Therefore, to conclude, a GNSS signal usually consists of these three main components: Carrier, a radio frequency sinusoidal signal at a given frequency in L band; Ranging code, also called as PRN codes, allowing the receiver to determine the travel time of microwave from satellite to receiver; Navigation data, a binary coded message on the satellite ephemeris, clock bias parameters, almanac, satellite health status and other complementary information.

2.1.1 GPS signals

GPS satellites continuously broadcast two L band signals modulated with

ranging codes and navigation messages, which are L1 at 1.57542 GHz and L2 at 1.2276 GHz. Recently, new civil signals are being added to the satellite constellation as a major focus of the GPS modernization program, which are L2C, L5 and L1C. Figure 2-1 is a brief description of GPS L1 and L2 signal structures. The L1 carrier is modulated by coarse/acquisition (C/A) ranging code for civilian use and by a pseudo random precision range code (P code). The P code has higher chipping rate and is longer, it only repeats once a week. It can be encrypted as a so-called P(Y) code which is only available to military equipment with a proper decryption key. L2 signals are only modulated by P code. The L1 and L2 signals received from each GPS satellite can be expressed as follows [Jin, 2014]:

$$S_{L1}(t)=\sqrt{2P_{C/A}}D(t)C_{C/A}(t)\sin(2\text{®}\ f_1t+\text{¤}_1)+\sqrt{2P_{P1}}D(t)C_P(t)\cos(2\text{®}\ f_1t+\text{¤}_1) \quad (2\text{-}1)$$

$$S_{L2}(t)=\sqrt{2P_{P2}}D(t)C_P(t)\cos(2\text{®}\ f_2t+\text{¤}_2) \quad (2\text{-}2)$$

Where $P_{C/A}$ and P_{P1} are received signal powers of in-phase component modulated by C/A code and quadrature component modulated by P code of L1 signal. P_{P2} is the signal power received of L2 signal. $D(t)$ is amplitude modulation for L1 and L2 containing navigation information. $C(t)$ is ranging code modulation with either C/A code or P code, denoted by the subscripts C/A and P.

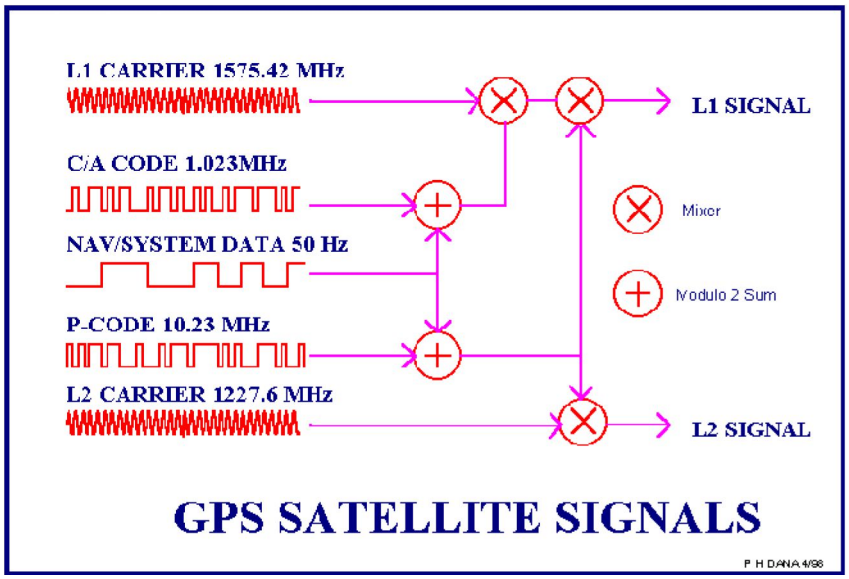

Figure 2-1 Signal structures of GPS L1 and L2 signals

2.1.2 Other GNSS signals

Other GNSS systems such as GLONASS, Galileo and Compass share some characteristics in common with GPS, but also have their unique properties. Considering that this work is done mainly based on GPS signals, the other GNSS systems are going to be described briefly here.

Like the GPS, GLONASS provides both high accuracy signal for military use and standard accuracy signal for civil use. Applied carrier frequencies are L1 (1602-1615.5 MHz) and L2 (1246-1256.5 MHz). The not single carrier frequency implies that GLONASS uses frequency division multiple access (FDMA) technique. The signals use similar direct sequence spread spectrum (DSSS) encoding and Binary phase shift keying (BPSK) modulation as in GPS signals, but all satellites transmit the same code and each transmits on a different frequency. FDMA is applied on both L1 and L2 band. New launched GLONASS-K satellite in 2011 introduced L30C signal with carrier frequency 1202.25MHz and CDMA modulation [Urlichich, 2011].

Galileo transmits 10 different navigation signals across three frequency bands: E5, E6 and E1-L1-E2 [Groves, 2008]. Basically it uses CDMA scheme for the ranging code and BPSK modulation. However, to increase the accuracy and to avoid the interference with other GNSS signals in the same band, binary offset carrier (BOC) modulation and alternate binary offset carrier (AltBOC) modulation scheme are also applied to some bands.

Compass is a Chinese navigation system and it's still in its development phase. It is foreseen to provide global navigation service upon its completion in 2020. Three carrier frequencies are used known as B1, B2 and B3 [Davoud, 2012]. CDMA is also applied as GPS and Galileo and mainly QPSK modulation is used on all the three bands [Grelier, 2007].

Table 2-1 shows a comparison between GPS, GLONASS, Galileo and Compass systems [Davoud, 2012].

Table 2-1 Comparison of GPS, GLONASS, Galileo and Compass

Characteristics	GPS	GLONASS	Galileo	Compass
First launch	February, 1978	October, 1982	December, 2005	April, 2007
Full operational capability	February, 1995	Jan, 1996-Dec, 2011	Up to 2020	Up to 2020
Funding	public	public	public & private	public
Nominal number of SV	24	24	27	27
Orbital planes	6	3	3	3
Orbit inclination	55 degree	64.8 degree	56 degree	55 degree
Semi-major axis	26,560 km	25,508 km	29,601 km	21,500 km
Orbit plane separation	60 degree	120 degree	120 degree	-
Revolution period	11h 57.96 min	11h 12.73 min	14h 4.75 min	12h 35 min
Geodetic reference system	WGS-84	PE-90	GTRF	CGS2000
Time system	GPS time, UTC (USNO)	GLONASS time, UTC (SU)	Galileo system time	Bei Dou System Time (BDT)
Signal separation	CDMA	FDMA	CDMA	CDMA
Number of frequencies	3-L1, L2, L5	One per two antipodal SV	3(4)-E1,E6,E5(E5a, E5b)	3-B1, B2, B3
Frequency [MHz]	L1: 1575.420	G1: 1602.000	E1: 1575.420	B1: 1575.420
	L2: 1227.600	G2: 1246.000	E6: 1278.750	B2: 1191.795
	L3: 1176.450	G3: 1204.704	E5: 1191.795	B3: 1268.520
Number of ranging codes	11	6	10	-

2.2 GNSS as a bi-static radar

Bi-static radar is a name referring to a radar system with transmitter and receiver not collocated. The transmitter and receiver are separated by a distance that is comparable to the expected target distance. In the contrary, radar in which the transmitter and receiver are collocated is called mono-static radar. As for GNSS-R, GNSS satellites usually act as transmitters and receiver is mounted on board aircraft, low orbit satellite or statically. As GNSS-R is used for surface remote sensing, the surface is therefore the desired “target” and the reflected signals contain information of the surface condition.

2.2.1 Geometry

The GNSS-R geometry as a bi-static radar is shown in Figure 2-2. Here GNSS

satellite is substituted by GPS satellite specifically since the whole work is done considering the GPS signals. As can be seen from the figure, the receiver with a certain distance above the surface can be equipped with two antennas: one up-looking RHCP antenna aiming at receiving the direct signal link and one down-looking LHCP antenna used for the reflected signal receiving, since the incident RHCP GPS signal is predominantly LHCP after specular reflection.

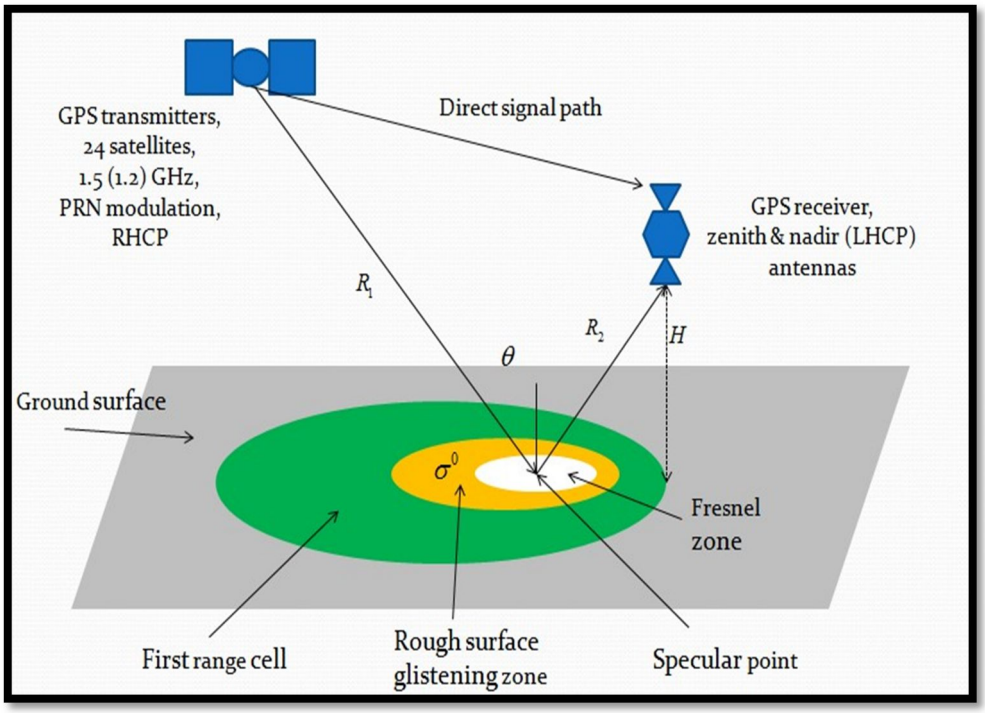

Figure 2-2 GNSS-R bi-static radar geometry

The specular point is in the place where specular reflection happens, characterized that the incident angle and the reflection angle are equal and in the same plane of the transmitter and receiver. When the surface is perfectly flat, the power is reflected by an active region called Fresnel zone coherently, and its size is determined that the differential phase change across the surface comparing with the specular point is limited to ® radians (half the wavelength of transmitted signal in length) [Beckmann, 1963]. The area of the Fresnel ellipse can be calculated when the distance between the surface and transmitter is much larger than the distance between the surface and the receiver (or vice verse). Thus, the semi-major axis a and the semi-minor axis b are determined by the incident angle ¯ and the minimum height of the transmitter or receiver H in the form [Katzberg and Garrison, 1996]:

$$a = \frac{\sqrt{2¢ H \cos(¯)}}{\cos^2(¯)} \qquad b = \frac{\sqrt{2¢ H \cos(¯)}}{\cos(¯)} \tag{2-3}$$

When the surface is rougher, more power will be scattered incoherently by an expanded active region surrounding the Fresnel zone, which is the so-called “glistening zone”. Therefore, for a moderately rough surface, received reflected signal consists of two components generally: a coherent part due to the specular reflection and an incoherent part caused by diffuse scattering. These two components are discussed in the following section.

As the reflection or scattering happens, the time delay comparing with the direct link and the frequency due to Doppler Effect change, in which case iso-range ellipses (lines of equal delay across the surface) and iso-Doppler hyperbolas (lines of equal Doppler frequency across the surface) can be mapped across the Earth. Figure 2-3 shows the delay and Doppler spreading across the surface.

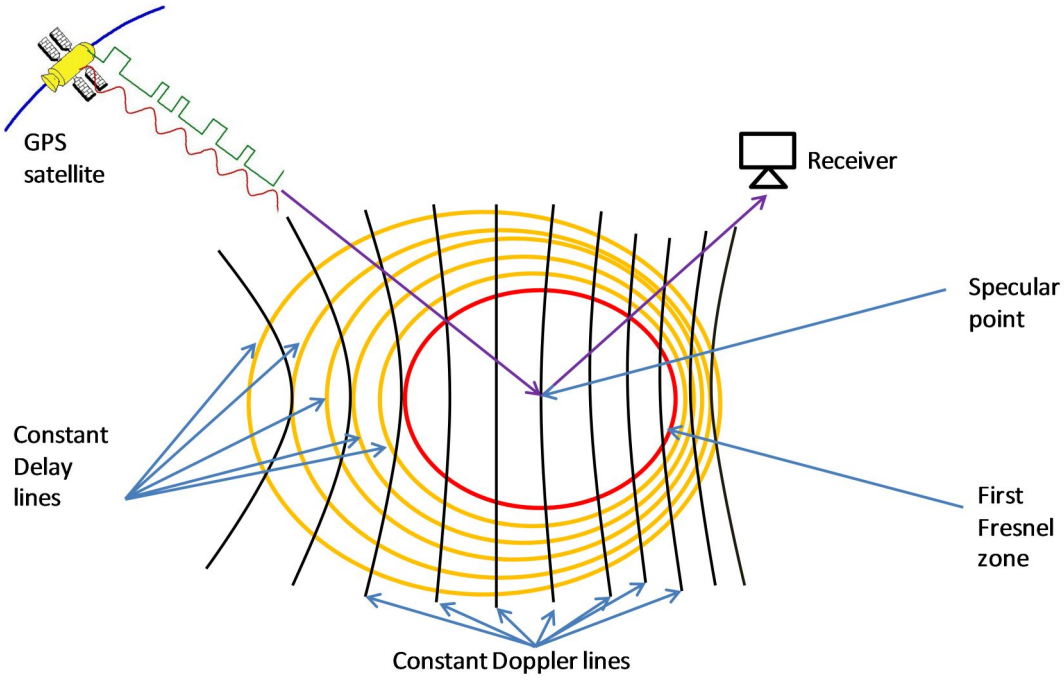

Figure 2-3 Delay and Doppler spreading across the surface

In the figure, lines of constant delay are those ellipses that are centered at the specular point, and lines of constant frequency result in hyperbolic shaped iso-Doppler lines of equal frequency cutting through the Fresnel zone (or glistening zone in a larger scale).

2.2.2 Bistatic radar equations

Unlike the monostatic radar, the bistatic radar has two or more routes for signal propagation form the transmitter to the receiver. However, the bistatic radar equation can be derived in the same way as the monostatic radar equation, and its general expression is [Griffiths, 2004]:

$$P^r = \frac{P^t G^t G^r \lambda^2 \sigma^0 A}{(4\pi)^3 R_1^2 R_2^2} \tag{2-4}$$

where P^r is received signal power, P^t is transmitted signal power, G^t and G^r are antenna gains of transmitter and receiver, respectively. λ is signal wavelength (about 19cm for GPS L1 signal). R_1 and R_2 represent the distances between specular point and transmitter or receiver. And σ^0 is the scattering coefficient per unit area of the surface A.

Eq. 2-4 is a general equation referring to the incoherent scattering, and it can be written in a form of integral of σ^0 within the glistening zone A which is shown in Eq. 2-5 [De Roo and Ulaby, 1994]

$$P_{qp}^i = \frac{P^t G^t}{4\pi R_1^2} \frac{G^r \lambda^2}{4\pi} \iint_A \frac{\sigma^0}{4\pi R_2^2} dxdy \tag{2-5}$$

where the superscript *i* indicates the incoherent power and the subscript *qp* denotes the polarization state: *q* polarization received and *p* transmitted. *q* and *p* denote VP or HP. In the case of specular reflection, the power is reflected coherently to the receiver, and the bistatic radar equation describing the coherent component in the GPS bistatic radar (RHCP transmitted, LHCP received) is [De Roo and Ulaby, 1994]:

$$P_{qp}^c = \frac{P^t G^t}{4\pi (R_1 + R_2)^2} \frac{G^r \lambda^2}{4\pi} R_{qp} \tag{2-6}$$

where the superscript *c* denotes the coherent component, R_{qp} is the power reflectivity of the surface. As Eq. 2-5, *q* and *p* denote vertical or horizontal polarization. The coherent power only exists for co-polarization scattering: $P_{qp}^c = R_{qp} = 0 \text{ if } p \neq q$. The power reflectivity R_{qp} is further a function of Fresnel

reflection coefficient of the equivalent smooth surface and attenuation factor due to the surface roughness effect:

$$R_{qp} = \left|\Gamma_{qp}\right|^2 P(z) \tag{2-7}$$

where Γ_{lr} is the Fresnel reflection coefficient and $P(z)$ is surface height distribution function which can be expressed in several ways. If a surface can be modeled well by a Gaussian height distribution with zero mean and variance $\pm^2$, the reflectivity becomes [Beckmann, 1963]:

$$R_{qp} = \left|\Gamma_{qp}\right|^2 \exp\left[-\left(\frac{4\pi\pm\cos^{-}}{a}\right)^2\right] \tag{2-8}$$

where $^{-}$ is the incident angle and a is the wavelength. As has been discussed in the previous section, for a general surface, reflected signal consists of both coherent power (specular reflection) and incoherent power (diffuse scattering), and it can be expressed:

$$P_{qp}^{r} = P_{qp}^{c} + P_{qp}^{i} \tag{2-9}$$

where P_{qp}^{r} is the total received power. When the surface is perfectly smooth, the diffuse scattering doesn't exist and the total received power contains only the coherent specular reflection. The determination of a "smooth" surface is indicated by the Rayleigh criterion:

$$\Delta h < \frac{1}{8}\frac{a}{\sin¥} \tag{2-10}$$

where Δh is the mean height of the irregularities within the First Fresnel ellipse and $¥$ is the grazing angle. The quantity $a/\sin¥$ is called the space wavelength. However, it has to be noted that the Rayleigh criterion supplies only a qualitative indication and uses only orders of magnitude, in reality there's no well defined dividing line between a smooth and a rough surface and therefore it's meaningless to find a more precise definition of the parameters [Beckmann, 1963].

The relationship between surface roughness and surface scattering is shown in Figure 2-4 as an example. For the specular surface shown by Figure 2-4 (a), the angular radiation pattern of the reflected wave is a delta function centered about the

specular direction. For the (slightly) rough surface which is shown in Figure 2-4 (b), the radiation pattern consists of both coherent component and incoherent component, the main power is again in the specular direction but with its magnitude smaller than the specular (a) case. For a very rough surface (Figure 2-4 (c)), the total power is diffuse scattered incoherently and the coherent component becomes negligible.

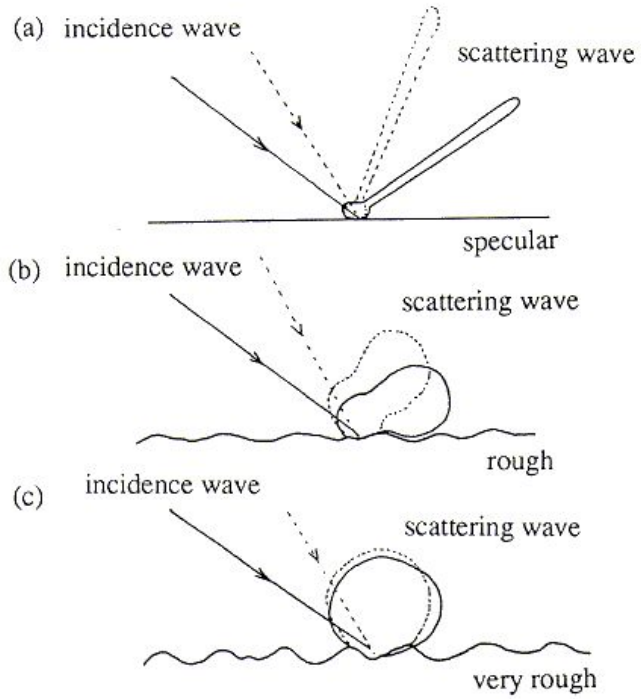

Figure 2-4 Surface scattering patterns versus different surface roughness
[Japan Association of Remote Sensing, 1996]

2.3 Surface scattering

2.3.1 Statistical description of a rough surface

The shape of a random rough surface can be generally described by the surface height distribution function and the surface height correlation function. These descriptions have been reported in many literatures ([Ulaby, 1982], [Pinel, 2013]) and hence, a brief introduction is given here.

For a surface whose height is given by $z = f(x, y)$, and its mean surface height is given by z_0, the surface height standard deviation is $\pm_h$. The type of surface height probability density function can be Gaussian, Lorentzian or exponential, etc.

Most of time, a rough surface can be characterized by a Gaussian height PDF, which gives the expression:

$$p_h(z) = \frac{1}{\pm_h \sqrt{2®}} \exp[-\frac{1}{2}(\frac{z - z_0}{\pm_h})^2] \tag{2-11}$$

where $p_h(z)$ is the surface height probability density function for Gaussian distribution.

The normalized surface height correlation function is the other descriptor of random rough surfaces. It describes the degree to which the height at one location is correlated to the height at another location, with respect to their horizontal distance $\vec{r}_d = \vec{r}_2 - \vec{r}_1$. The correlation comes to maximum if $\vec{r}_d = 0$. It is defined by:

$$°_h(\vec{r}_1, \vec{r}_2) = \langle z(\vec{r}_1) z(\vec{r}_2) \rangle = \lim_{X,Y \to +\infty} \frac{1}{XY} \int_{-X/2}^{+X/2} \int_{-Y/2}^{+Y/2} z(\vec{r}_1) z(\vec{r}_2) dxdy \tag{2-12}$$

where (X, Y) are the surface lengths with respect to *x* and *y* axis, respectively. For a stationary surface,

$$°_h(\vec{r}_1, \vec{r}_2) \equiv °_h(\vec{r}_d) = \langle z(\vec{r}_1) z(\vec{r}_1 + \vec{r}_d) \rangle \tag{2-13}$$

is satisfied, with the property $°_h(\vec{r}_d = 0) = \pm_h^2$, which is the RMS height (height standard deviation) and can be used to normalize the spatial correlation Eq. 2-12. The correlation length l is a characteristic value of the autocorrelation function, representing the scale of roughness of the surface, and it's determined by the length at which the normalized correlation function is equal to e^{-1}.

The root mean square (rms) slope is subsequently indicated as *m*, with $m = \left(-\pm_h{}^2 °''_h(0)\right)^{1/2}$, when the normalized autocorrelation function is Gaussian, the rms slope is equal to $m = \sqrt{2} \pm_h / l$

2.3.2 Scattering models

The studies of modeling scattering of electromagnetic field due to surface rough have been taken for decades ([Beckmann, 1963], [Ulaby, 1982], [Fung, 1994], [Ticconi, 2011]). Several well established models such as Kirchhoff Approximation, Small Perturbation model and the Integral Equation Method (IEM) have been

addressed in many researches. In this thesis, soil moisture retrieval algorithms derived for either specular reflection or diffuse scattering are illustrated in detail in Chapter 5, hence, only concise descriptions are given here.

Knowledge of scattering geometry and definition of bistatic scattering coefficient is necessary before applying the scattering models. Figure 2-5 shows the geometry of scattering.

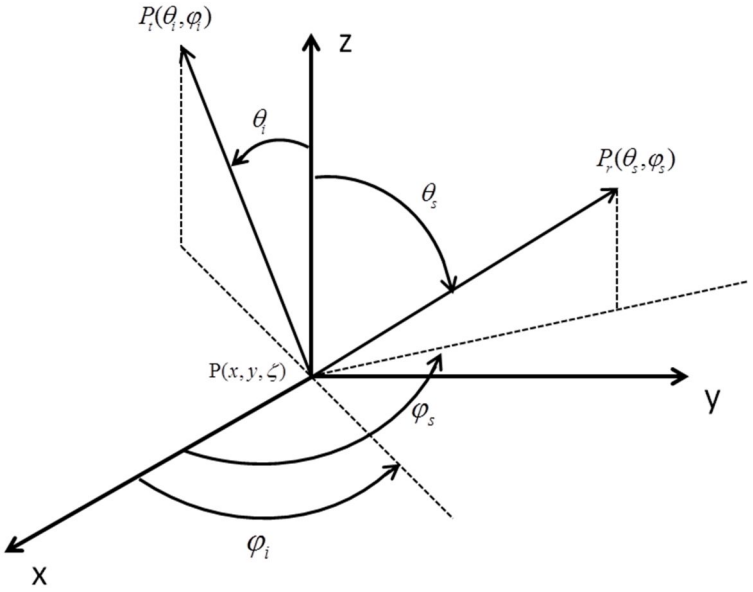

Figure 2-5 Geometry of scattering

$P_t(\theta_i,\varphi_i)$ and $P_r(\theta_s,\varphi_s)$ are transmitted and received power at direction (θ_i,φ_i) and (θ_s,φ_s) respectively. Subscripts of *i* and *s* denote incident and scattering. $P(x,y,\zeta)$ is the statistical property of surface height. It's then possible to define the bistatic scattering coefficient σ^o_{qp} (subscripts *q* and *p* denote scattering field at polarization *q* and incident field at polarization *p*), which is dependent on the microwave frequency, polarization, incidence and observing directions and is in terms of the incident and scattering field E^i_p and E^s_q as follows [Ulaby, 1982]:

$$\sigma^o_{qp}(\theta_i,\varphi_i,\theta_s,\varphi_s)=\frac{4\pi R^2\left|E^s_q\right|^2}{A_0\left|E^i_p\right|^2} \tag{2-14}$$

where the bistatic scattering coefficient is given as the ratio of the total power scattered by an equivalent isotropic scatterer in direction (θ_s,φ_s) to the product of the incident power density in direction (θ_i,φ_i) and the illuminated area.

The Kirchhoff Approximation (KA) model is one of the first models applied

and is employed for moderate to rough surfaces. In the Kirchhoff approach, the total fields (incident and scattered) at any point on the surface are approximated by the fields that would be present on an infinitely extended tangent plane at that point. The reflection is therefore considered to be locally specular.

Following this tangent plane approximation, the total field at a point on the surface is assumed equal to the incident field plus the field reflected by an infinite plane tangent to the point, and the detailed expression is given in [Ulaby, 1982]. In order to get analytic solution from this approximation, further additional simplifying assumptions should be applied, such as the stationary-phase approximation (Geometric Optics, GO) for surface with large standard deviation of surface heights (with respect to wavelength) and scalar approximation (Physical Optics, PO) for surfaces with small slopes and a medium or small standard deviation of surface heights (See [Tsang, 2000] and [Tsang and Kong, 2001] as review).

The small perturbation method (SMP) is based on formulating the scattering as a partial differential equation boundary value problem and to find a solution in terms of plane waves that matches the surface boundary conditions. It is a good model for small slopes statistics.

The bistatic scattering coefficient for either a horizontally or vertically polarized incident wave is given [Ulaby, 1982], [Ticconi, 2011]:

$$\pm_{qp}^{o} = 8\left|k^2 \pm \cos\bar{}_i \cos\bar{}_s \sim_{qp}\right|^2 W(k_x + k\sin\bar{}_i, k_y) \tag{2-15}$$

where

$$k_x = -k\sin\bar{}_s \cos\ddot{}_s \tag{2-16}$$

$$k_y = -k\sin\bar{}_s \sin\ddot{}_s \tag{2-17}$$

$$W(k_x, k_y) = \frac{1}{2\circledR}\int_{-\infty}^{\infty}\int_{-\infty}^{\infty} \circ(u,v) e^{-jk_x u - jk_y v} du dv \tag{2-18}$$

$\pm$ is the variance of surface heights and $\circ(u,v)$ is the surface correlation coefficient; $\sim_{qp}$ are coefficients that depend on polarization, incident and scattering angle, and on complex relative dielectric constant $£_c$ of the

homogeneous medium below the interface.

The Integral Equation Method (IEM) is a relatively new method trying to provide good predictions for a wide range of surface profiles and to bridge the gap between KA and SPM, and thus it covers all roughness scales [Fung, 1994]. This method is relatively complicated in its general form and computationally expensive, but quite accurate, and this is the reason why it has been used extensively in the microwave region in recent years.

The general expression is very complicated and the bistatic scattering coefficient $\pm_{qp}^{o}$ is given by a sum of three terms:

$$\pm_{qp}^{o} = \pm_{qp}^{k} + \pm_{qp}^{kc} + \pm_{qp}^{c} \tag{2-19}$$

which are the Kirchhoff fields, the interaction between Kirchhoff and complementary fields (cross term) and complementary fields. Exact expressions of these three terms are reported by [Fung 1994]. A single equation of bistatic scattering coefficient is given in the case that the surface height is moderate in terms of the incident wavelength ($k\pm < 2$, as an indicative threshold value reported by [Fung, 1994]), and that only single scattering contributions are selected (multiple-scattering terms are neglected) in the expressions of $\pm_{qp}^{k}$, $\pm_{qp}^{kc}$ and $\pm_{qp}^{c}$ by [Ticconi, 2011]:

$$\pm_{qp}^{o} = \frac{k^2}{2} e^{-\pm^2 (k_z^2 + k_{sz}^2)} \sum_{n=1}^{\infty} \frac{\pm^{2n}}{n!} \left| (k_z + k_{sz})^n f_{qp} e^{-\pm^2 k_z k_{sz}} + \frac{(k_{sz})^n F_{qp}(-k_x, -k_y) + (k_z)^n F_{qp}(-k_{sx}, -k_{sy})}{2} \right|^2 * W^{(n)}(k_{sx} - k_x, k_{sy} - k_y) \tag{2-20}$$

The Small Slope Approximation (SSA) was also brought in mid 1980s to unify KA and SPM [Voronovich, 1996]. The SSA is applicable regardless of the wavelength of radiation, on the condition that the slopes of the roughness are small compared to the angles of incidence and scattering [Jin, 2014]. The SSA is restricted to single-scattering phenomena and the non-local small-slope approximation is a modification of the SSA for situations in which multiple scattering from points situated each other at significant distance becomes important [Berginc, 2002].

Chapter 3 Hardware receiver

3.1 Antennas

Antenna characterizations are important for GNSS-R research. Therefore, carefully choosing or designing an appropriate antenna is highly required. Based on the reflection theory shown in the previous chapter, for moderate rough surface, reflected GNSS signals are predominately LHCP corresponding to its transmission polarization of RHCP. Hence, an L1 band (for GPS L1 signal) LHCP antenna is of our requirement for LHCP reflection signal measurement (dual polarization of both LHCP and RHCP is preferred for some advanced measurement). The other needs that should be met include the cross polarization level, which should be lower than -17dB [Egido, 2012]; the half power beam width (HPBW), which should be wide enough for signal collection of multiple satellites (for our research), and a purely circular polarization for either LH or RH, which requires the axial ratio (AR) to be lower than 3 dB.

A lot of studies and simulations have been taken for sever types of antennas, including a prototype of helix antenna, simulations of patch antennas and choosing and testing of several commercial antennas.

3.1.1 Helix antenna

The design specifications of the helix antenna are:

- About 10 dB of maximum gain
- 20 MHz bandwidth centered on 1575 MHz
- LHCP
- HPBW is about 60 degrees

Both 4-turn and 5-turn helix antennas are simulated through High Frequency Structure Simulator (HFSS), and a helix antenna with 4 turns was built as shown in Figure 3-1. The spacing equals to 50 mm, the diameter equals to 65 mm and the dimension of the ground plane is 150 mm*150 mm [Ren, 2012].

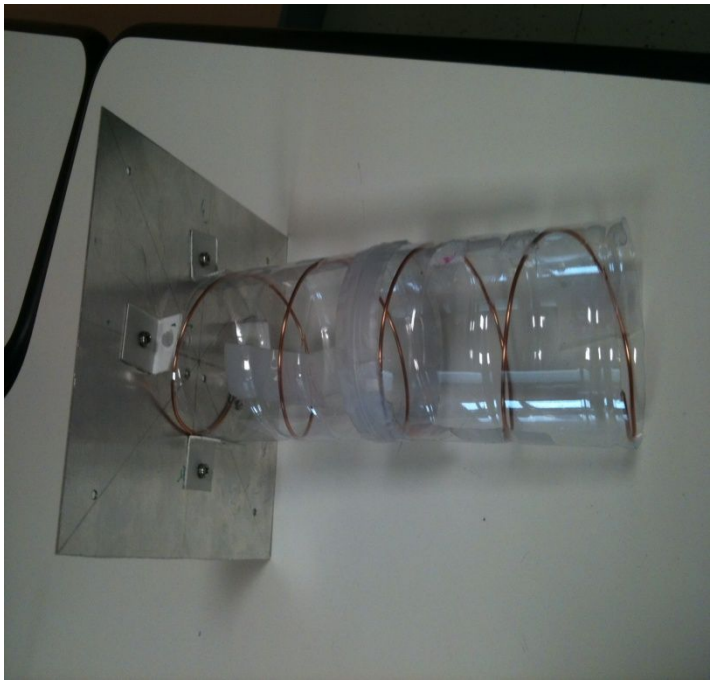

Figure 3-1 Built helix antenna with 4 turns

The helix antenna was tested in anechoic chamber, the measured results comparing with simulation results of radiation patterns at 1575 MHz are shown in Figure 3-2.

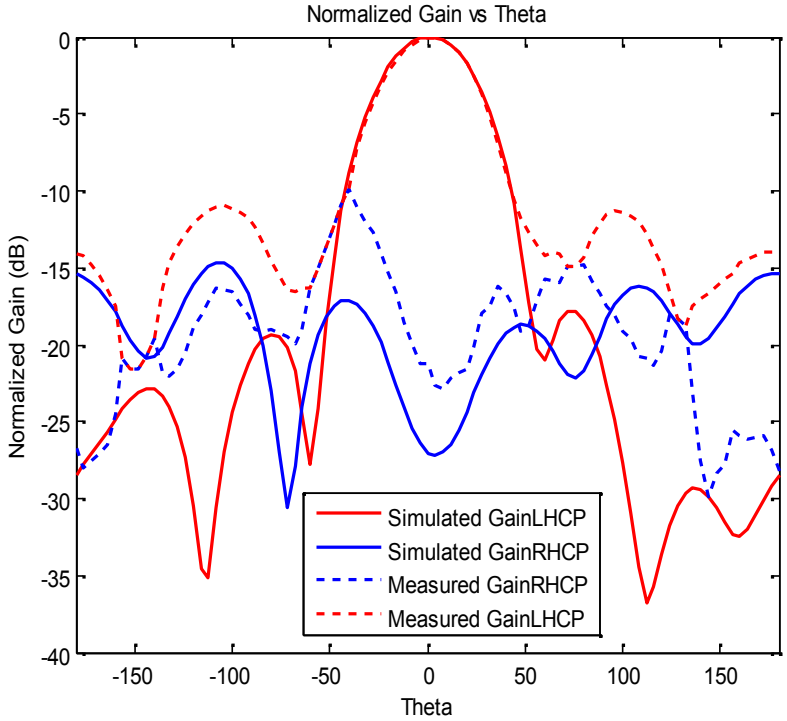

Figure 3-2 Radiation patterns of helix antenna

Since for both simulated and measured radiation patterns, the two planes (A and B or E and H planes) are nearly symmetric, only one plane from each of simulation and measurement is plotted in the same figure for comparison. The measured radiation patterns are in good agreement with simulated ones considering the main lobe and are coherent with the specifications in these aspects: about 11 dB of maximum gain, 50 degrees of HPBW and good cross polarization level (lower than -15 dB within HPBW). The measured AR with simulated one is shown in Figure 3-3, seen from which, the circular polarization is achieved.

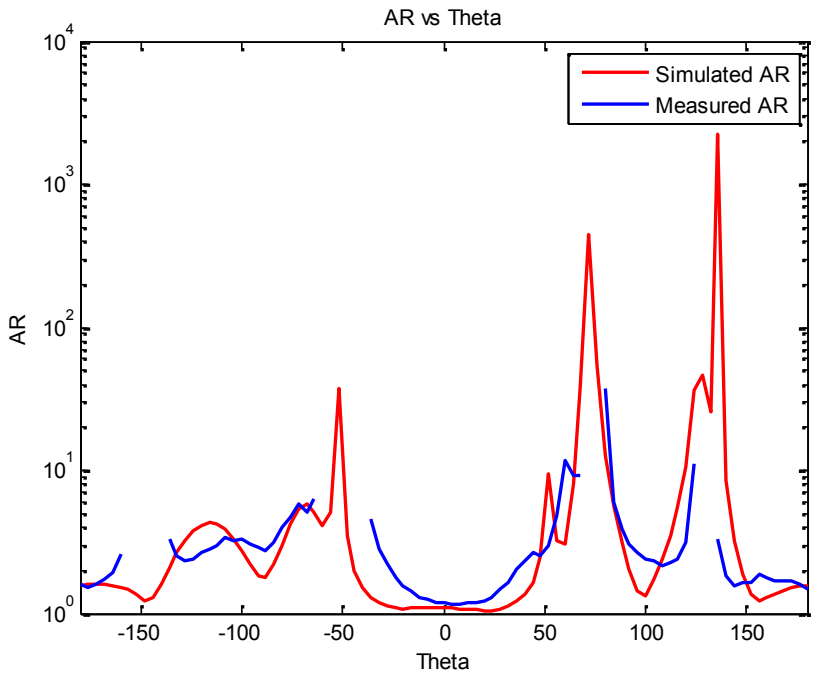

Figure 3-3 Simulated and measured AR of helix antenna

However, due to helix antenna's big dimension, it has limited use for our measurement campaigns especially for flight measurements.

3.1.2 Patch antenna

The main motivation of design and simulation of a dual port patch antenna is to meet the cross polarization requirement which is usually not satisfied by commercial ones [Jia, 2014]. The basic design idea is to use a 3dB branch coupler as feeding network to provide dual polarization. By adding another patch for coupling above the radiating patch antenna, which is called the parasitic patch, it becomes a dual port stacked patch antenna. Two kinds of patch models have been

simulated and will be realized very soon. One is full FR4 model: the three layers (feeding network layer, active patch layer and parasitic layer) are all using FR4 material. The other one is called the hybrid model: the parasitic layer uses Roger 5880 and the rest still utilized FR4 material. The model structure is shown in Figure 3-4.

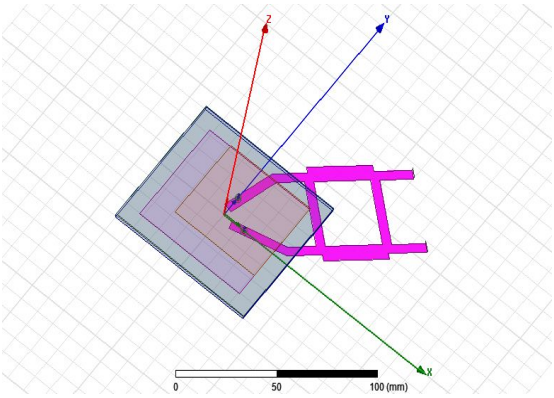

Figure 3-4 Structure of the dual polarization patch antenna

The simulation results of the hybrid model are shown in the following as an example. One of these two models will be manufactured in the near future.

S parameters are shown in Figure 3-5. Return loss achieves -34 dB for port 1 and -37 dB for port 2. Port 1 achieves -14 dB return loss with bandwidth 240 MHz (1.43-1.67 GHz) and it's the same for port 2.

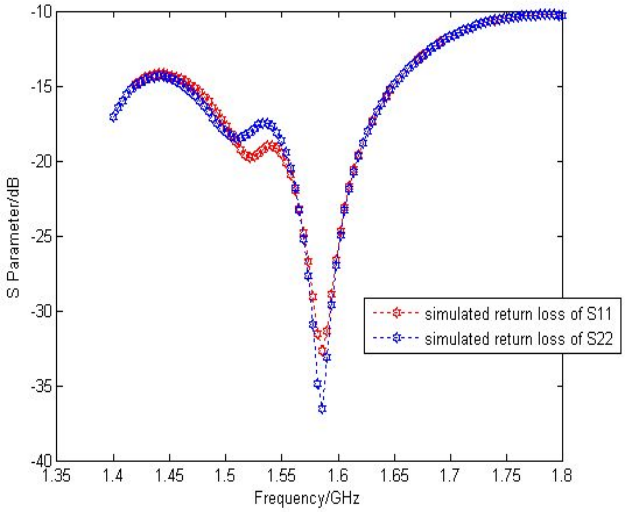

Figure 3-5 S parameters of hybrid model

Figure 3-6 shows the AR values for both LH and RH channels. The blue line

indicates the 3 dB AR value and it can be seen that the range in which AR is below 3 dB is roughly from -90 degree to +50 degree. The antenna has fairly good circular polarization.

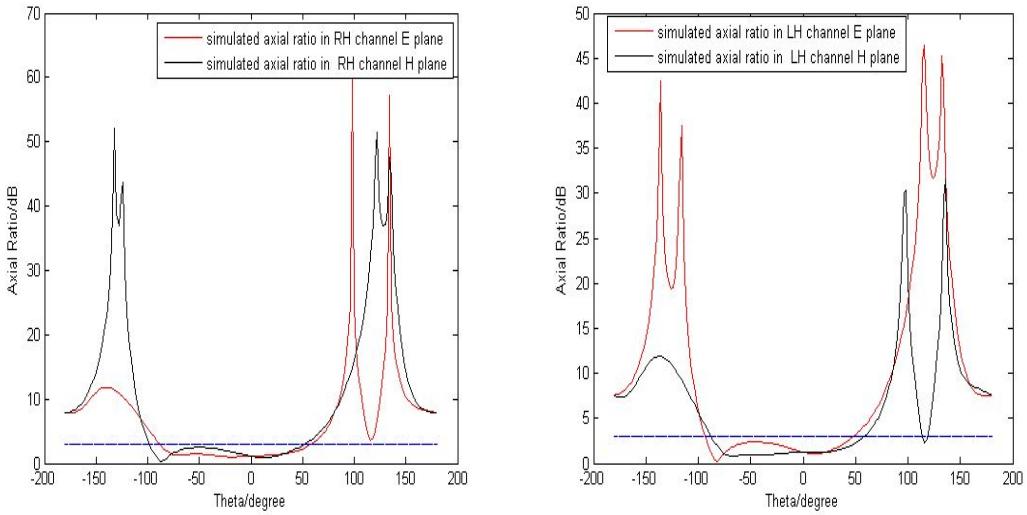

(a) (b)

Figure 3-6 Axial ratio (a) in LH channel, (b) in RH channel

The simulated radiation patterns for RH channel gain and LH channel gain in the theta pattern at center frequency 1.575GHz are shown in Figure 3-7. As shown, the proposed antenna possesses broad pattern coverage and high cross polarization at the low angles.

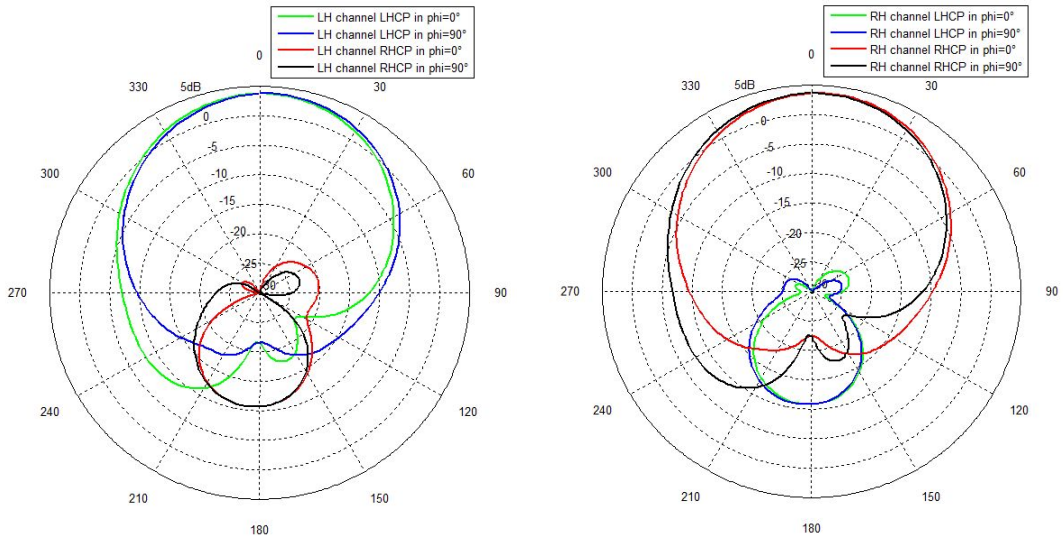

(a) (b)

Figure 3-7 Radiation patterns in (a) LH channel, (b) RH channel

3.1.3 Commercial antennas

In the framework of the regional project SMAT-F2, we were also provided the possibility to look into market for antennas that meet the needs of GNSS-R measurements, especially for the LHCP antennas. For most of the measurements presented in this thesis, the antenna shown in Figure 3-8 (a) was applied. It is a dual polarization (LHCP/RHCP) antenna working in GPS L1/L2 band produced by Antcom Corporation [Antcom Corperation] with the data sheet presented in Figure 3-8 (b).

(a)

FREQUENCY:	L1: (1575.42 ±12) MHz		L2: (1227.60 ±12) MHz	
RADIATION PATTERN:	HEMISPHERICAL			
POLARIZATION:	RHCP/LHCP		RHCP/LHCP	
VSWR:	< 1.5:1		< 1.5:1	
IMPEDANCE:	50 ohms		50 ohms	
ANTENNA GAIN (dBic):	Free Space	4 ft G.P.	Free Space	4 ft G.P.
@ 90 ° (ZENITH):	+ 4.7	+ 3.5	+ 3.3	+ 4.9
@ 10 ° Elevation:	- 1.8	- 2.0	- 3.8	- 3.6
@ 20 ° Elevation:	- 0.3	+ 0.8	- 2.0	- 0.1
@ 30 ° Elevation:	+ 1.4	+ 1.8	- 0.5	- 1.8
@ 60 - 90 ° Elevation:	> 3.9	> 2.8	> 2.7	> 3.0
BEAM WIDTH (3dB):	114 Deg.	139 Deg.	106 Deg.	75 Deg.
AXIAL RATIO:	2 dB		2 dB	
LIGHTNING PROTECTION:	DC GROUNDING			
LNA GAIN:	33 dB		35 dB	
LNA NOISE FIGURE:	3.0 dB		3.0 dB	
LNA P1dB Out:	+13 dBm		+13 dBm	
LNA DC POWER:	2.5V/20mA, 3V/29mA, 3.3V/35mA, (2.5-24)V/<50mA			
POWER HANDLING	1 Watt CW, Optional: 10 Watts 1 Microsec Pulse (-AL-)			

(b)

Figure 3-8 Antcom dual polarization RHCP/LHCP L1/L2 GPS (a) antenna, (b) data sheet

Recently, as the need for making static measurements on both LHCP and RHCP reflected signals simultaneously grows, another two identical antennas that were produced by Antcom were purchased. The picture of the antennas and standard datasheet are shown in Figure 3-9.

They are also dual polarization RHCP/LHCP L1/L2 GPS antennas, and are active antennas enclosed on a 2 inches squared radome (53 mm x 53 mm) and are equipped by a LNA capable to provide a 33 dB gain. Datasheets show slightly

different radiation patterns considering free space case (no ground plane (G. P.)), a circular 3'' G. P. (7.6 cm diameter), a circular 4 ft G. P. (1.2 m diameter). For our particular application a G. P. is necessary, but it cannot be too big, because the antenna should be mounted below the receiver in one bay slot. Therefore, considering the 3'' G. P. solution, we can see that the maximum gain is 4.7 dB, which provides an HPBW of 114°. In this case the antenna should be capable to collect reflected signals coming with an elevation angle greater than 33°.

Cross polarization isolation is a key parameter which makes such kind of antenna very attractive. The datasheet indicates that a 2dB AR is available for both polarizations.

(a)

FREQUENCY:	L1: (1575.42 ±12) MHz			L2: (1227.60 ±12) MHz		
RADIATION PATTERN:	HEMISPHERICAL					
POLARIZATION:	RHCP/LHCP			RHCP/LHCP		
VSWR:	< 1.5:1			< 1.5:1		
IMPEDANCE:	50 ohms			50 ohms		
ANTENNAGAIN (dBic):	Free Space	3 in G.P.	4 ft G.P.	Free Space	3 in G.P.	4 ft G.P.
@ 90 ° (ZENITH):	+ 3.7	+ 4.7	+ 3.1	- 1.7	+ 3.3	+ 4.5
@ 10 ° Elevation	- 2.9	- 1.8	- 1.9	- 7.3	- 3.8	- 3.5
@ 20 ° Elevation	- 1.3	- 0.3	+ 0.6	- 6.2	- 2.0	- 0.8
@ 30 ° Elevation	0.0	+ 1.4	+ 1.7	- 5.2	- 0.5	+ 1.4
@ 60 - 90 ° Elevation:	> 3.0	> 3.9	> 2.4	> - 3.2	> 2.7	> 2.2
BEAMWIDTH(3dB):	108 Deg.	114 Deg.	143 Deg.	100 Deg.	106 Deg.	74 Deg.
AXIALRATIO:	2 dB			2 dB		
LIGHTNINGPROTECTION:	DC GROUNDING					
LNA GAIN OPTION	33 dB			35 dB		
LNA NOISE FIGURE:	3.0 dB			3.0 dB		
LNA P1dB Out:	+13 dBm			+13 dBm		
LNA DC POWER:	2.5V/20mA,3V/29mA,3.3V/35mA,(2.5-24)V/<50mA					
REJECTION@ (-50/+50)MHz	-41 dB / -59 dB			-40 dB / -40 dB		
@ (-100/+100)MHz	< -65 dB			< -65 dB		
POWERHANDLING	1 WattCW, Optional: 10 Watts 1 microsecPulse (-AL-)					

(b)

Figure 3-9 Antcom dual polarization RHCP/LHCP L1/L2 GPS (a) twin antennas, (b) data sheet

However, measurements that utilized these two antennas seemed to give

unreasonable and random results, therefore, characterizations of one of these two antennas were done again in the anechoic chamber. And results demonstrated a disagreement with the official data sheet. Here only the radiation pattern measurement results on one cut (the other orthogonal cut has similar behavior) at L1 frequency are given as references, which are shown in Figure 3-10.

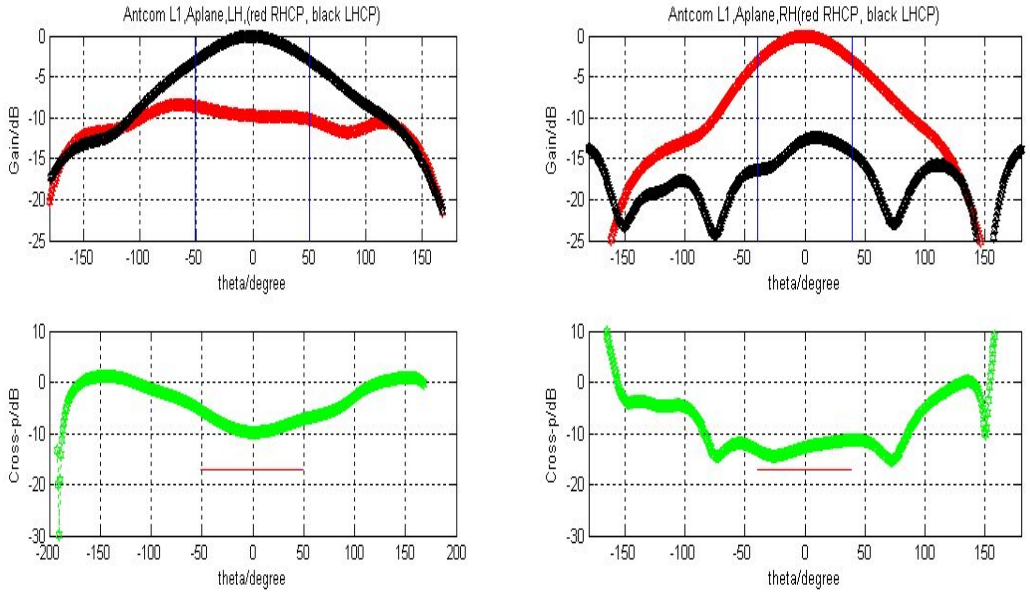

(a) (b)

Figure 3-10 (a) Radiation pattern for LHCP channel in the upper part and cross polarization level in the lower part. (b) Radiation pattern for RHCP channel in the upper part and cross polarization level in the lower part

In Figure 3-10, the distance between the two vertical blue lines in the upper part of (a) and (b) indicates the HPBW aperture, and the red horizontal line in the lower part of (a) and (b) is the reference line of -19dB of cross polarization isolation that the antenna is required to achieve. As shown in Figure 3-10, the cross polarization level is far different from the data sheet (barely meets the requirement) and in both channels the antenna is more directive (HPBW<=100°) than what is described in data sheet. Therefore, it can be said that these antennas are not so ideal for our research, and further verification is to be continued.

3.2 SiGe frontends

Another important hardware choice concerns the Radio Frequency Front End

circuit (see Figure 3-11). The SiGe GN3S Sampler v2 was developed by the [GNSS @ Colorado Center for Astrodynamics Research].

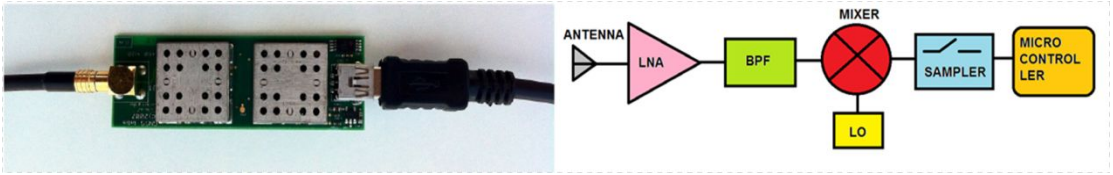

Figure 3-11 SiGe GN3S Sampler v2 (left) and its structure scheme (right)

It is composed of two main integrated circuits. The first one is an Application Specific Integrated Circuit (ASIC), which basically amplifies the incoming radio frequency (on the L1 GPS bandwidth), filters it, down-converts it from the GPS carrier frequency to an intermediate frequency of 38.4 MHz and samples it (sampling rate 8.1838 MHz, which can provide up to 8 samples per each code chip of the modulating C/A code). Two bits for representing both the In-phase and the Quadra-phase samples of the signal component are used and are sent to the second circuit, the microcontroller, which transfers in real time the ASIC generated samples into an USB bus.

Basically, the system we developed is a Software Defined Radio device. Even if the other steps of signal processing are performed following a pure software approach, a device to store and to post-process all the samples of the raw signal available is necessary. In this case, we developed two different solutions, which are presented in the following sections.

3.2.1 PC based receiver

This solution is based on the use of a Laptop PC which is directly connected to the frontend through the USB port (see Figure 3-12). The raw data sampled and transferred by the frontend are collected and recorded by the N-Grab software, which is developed and provided by NAVigation Signal Analysis and Simulation group (NAVSAS) of Politecnico di Torino.

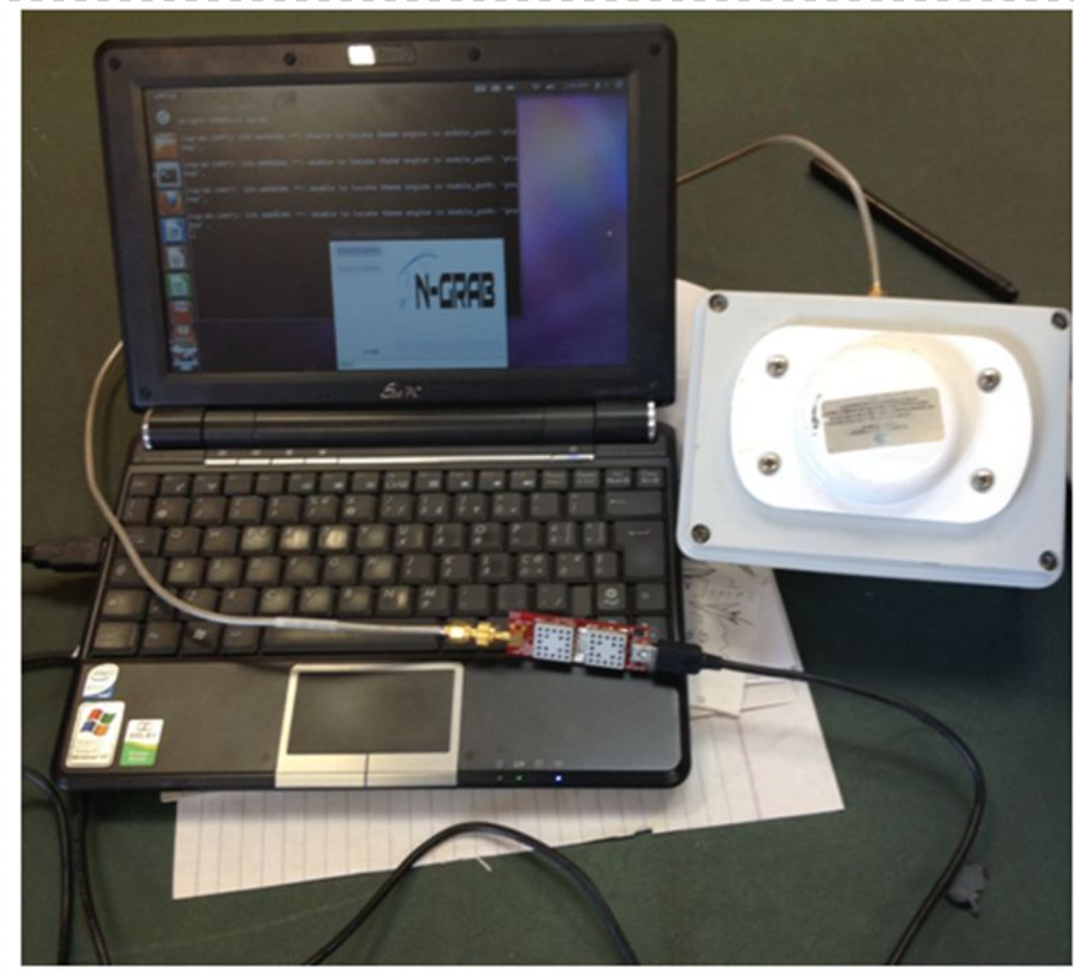

Figure 3-12 Structure of PC based receiver

This configuration can be easily extended to support two different frontends, with one of them connected to an up-looking RHCP antenna, in order to allow the collection also of the direct GPS signals for positioning purposes and for geo-referencing specular reflection points into the terrain, and even for the potential possibility to calibrate the reflected signal. Also in this case, a fully software GPS receiver solution can be easily adopted, implementing all the standard closed loop signal processing steps to the digital samples of the received raw signal (see for example the NGene software receiver, developed by the NAVSAS Group [Fantino, 2009]).

3.2.2 HackBerry board based receiver

A more stand alone, compact and trendy solution, was based on a System on Chip (SoC) device able to store a large amount of raw samples available during a

single measurement: the Hackberry A10 Development Board [Developer Shop by Miniand], (see details of this board in Figure 3-13).

System	• 1.2GHz Cortex A8 ARM Core (Running @ 1.0GHz) • MALI400MP OpenGL ES 2.0 GPU • DDR3 1333 9-9-9 1GB • 1080p Hardware-accelerated Video playback • 4GB NAND Flash Controller
I/O	• 2 SDIO interfaces (SD 3.0, UHI class) are Broken Out • 1 x SD Card Slot • 3 x USB 2.0 Downstream Standard Ports via GL850G Host Controller • 1 x USB-OTG Interface (USB-OTG can be reconfigured as USB 2.0 Host, automatically) • 1 x UART (3.3v TTL 4-pin header) • 1 x IR Receiver • Power Button, Reset Button, Recovery Button
Digital Audio/Video Output	• HDMI (1080p) • HDMI Digital Audio Out
Analog Audio output	• 3.5mm 2 Pole Headphone • 3.5mm Mic In
Analog Video output	• 3.5mm Composite AV • 3.5mm Component Y/Pb/Pr
Power	• AXP209 PMU • NEMA 2-pin power adapter included Input AC100-240V-0.4A 50/60Hz Output DC5v 1.2A • Battery Functionality is not broken out
Network Connectivity	• 10/100 Ethernet (MII compatible) • RTL8188CUS WiFi b/g/n USB Module

Figure 3-13 Characteristics of the Hackberry A10 Development board.

The entire system was implemented on an electronic board (100mm x 80mm). Thanks to its lightness, small dimensions and independency from external power source, it can be easily used as a payload for a small Unmanned Aerial Systems (UAS), remotely and/or automatically controlled. Some internal subsystems - including the storage device, the oscillator, the power supply (it can be powered by an external battery which is also able to provide the required current to the Antenna's Low Noise Amplifier), the Ethernet LAN and the USB management - were customized in order to better suit the performance of the frontend. A customized version of the operating system based on Linux Debian was also developed for the HackBerry board processor. The entire device was able to operate via the SSH protocol using either the Ethernet LAN port or a wireless connection (an internal WiFi transmitter is available). This is extremely useful in order to access the onboard firmware which contains several user setup parameters.

The board, the front-end and the antenna were finally integrated into a single box, as shown in Figure 3-14.

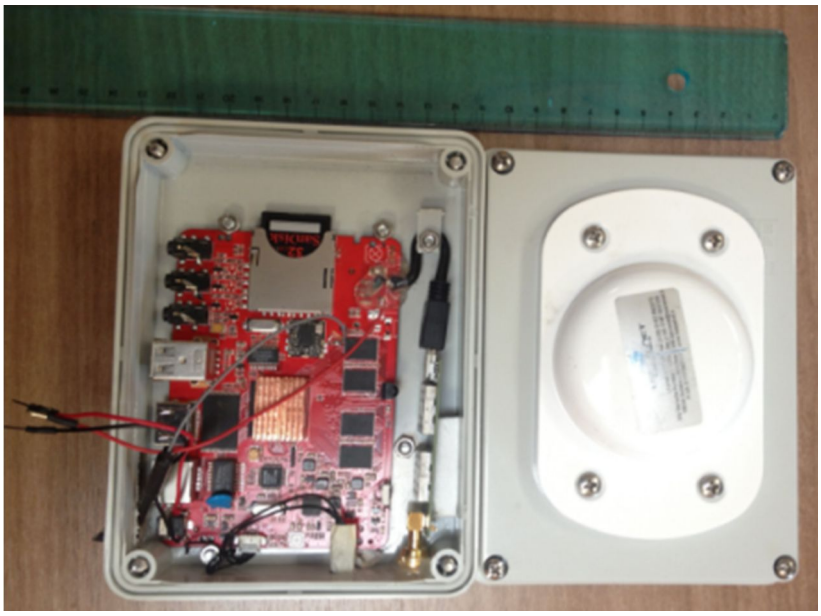

Figure 3-14 Integration of Hackberry board and SiGe frontend in a single compact box

This second solution was adopted from static position only in order to test its effectiveness. After the board being switched on, the operating system boot takes around 40 sec. Data can be acquired for a certain user defined time interval (less than 40 sec) or up to when the on board RAM is full. The data acquired are then automatically downloaded into an on-board SD card. The performances of the Hackberry Dev 10 are not adequate for the processing steps explained in Chapter 4, acquired data are currently post-processed by a standard PC.

In the framework of SMAT F2 and in cooperation of ISMB and NAVSAS group, another new compact receiver is under development and it is to be used for flight measurement on soil moisture, its prototype has been produced and details are reported in [Gamba, 2013].

Chapter 4 Prediction and processing programs

4.1 Satellite prediction and georeferencing

GNSS-R applies the bistatic radar geometry. Therefore, the position of the specular point which is of our interest is determined by both the positions of the transmitter (GNSS satellite) and the receiver. The knowledge of a coordinate system and Earth representation is necessary for georeferencing specular point. The Earth-centered Earth-fixed (ECEF) frame has its origin at the center of the ellipsoid modeling the Earth's surface, and it is roughly at the center of mass. In this frame, all axes remain fixed with respect to the Earth and z axis always points along the Earth's axis of the rotation from the center to the North Pole. The ECEF frame is important in navigation because the user wants to know their position relative to the Earth, so it is commonly used as both a reference frame and a resolving frame [Groves, 2008].

The ECEF frame enables the user to know its position with respect to the center of the Earth. However, for most of the cases, users want to know the position relative to the Earth surface. A type of ellipsoid is usually used to model the irregular Earth surface and the World Geodetic System 1984 (WGS84) is one of the main standards. The ellipsoid is the simplest geometric model which best fits the entire Earth surface [Misra and Enge, 2001] and it's also the reference for measurements of the geoid and terrain surfaces.

The geoid is a model of the Earth's surface that extends the mean sea level equipotential to include the land masses. All points on the geoid have the same gravitational potential and the force of gravity acts everywhere perpendicular to the geoid. The height of the geoid with respect to the ellipsoid is denoted N (see Figure 4-1). The current WGS84 geoid model is known as the Earth Gravity Model 1996 (EGM96).

The height of a body above the geoid is known as the orthometric height (also known as elevation) or the height above mean sea level and is denoted H shown in Figure 4-1. h represents the terrain height with respect to the ellipsoid. The

orthometric height is related to the geodetic height by [Groves, 2008]

$$H \approx h - N \tag{4-1}$$

Typical GPS measurements (initial results without correction and adjustment) give the receiver height with respect to the ellipsoid which is the geodetic height, but orthometric height is more useful and often used for many applications. Maps tend to express the height of the terrain and features with respect to the geoid, for instance, the Google Earth [Stillman, 2009], which is used for planning our static measurements. Knowing in advance whether the height provided by the GPS receiver or a certain map is geodetic height or orthometric height is important for georeferencing specular point on the Earth's surface.

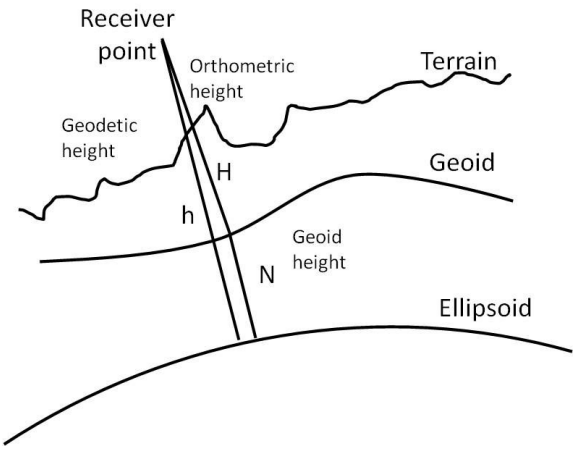

Figure 4-1 Height, geoid, ellipsoid and terrain

For our measurement campaigns including flight measurement and static measurements which are demonstrated in Chapter 5, georeferencing of specular points was done in the ECEF coordinate frame, by assuming the surface is locally flat (regardless of the curved Earth surface) and the surface height remains the same with that of the receiver projection position. This method is accurate enough in our case since the receiver was relatively low (less than 800m from the surface) with respect to the radius of the Earth and the specular points didn't separate far from the projection of the receiver. The flight measurement was equipped with onboard GPS receiver which provided ECEF coordinates for both transmitters (GPS PRNs) and receiver and georeference is easy to implement. For other static measurements, locations were planned by utilizing Google Earth. Surface elevation was given by the orthometric height along with longitude and latitude. Therefore,

the total receiver height (surface orthometric height + receiver height over surface, or in other words the receiver orthometric height) was converted to geodetic height first and then its latitude, longitude and altitude with respect to WGS84 were further converted to ECEF frame for georeferencing specular points.

4.1.1 Skyplot

Skyplot shows the positions of satellites in terms of elevation and azimuth. The elevation is presented by the concentric rings nested within one another. The outside ring is 0° and the middle of the plot is a 90° elevation (see Figure 4-2) The azimuth is the direction angle with respect to North (0°) measured clockwisely.

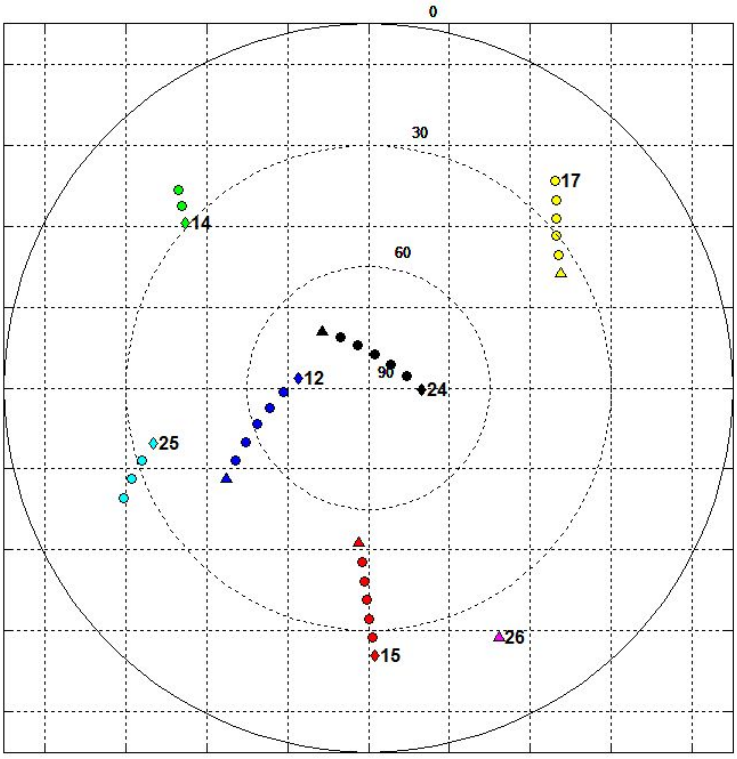

Figure 4-2 Skyplot of GPS satellites on July 25, 2014, from 10.00am to 11.00am, with time interval of 10min

Figure 4-2 shows an example of skyplot of GPS satellites on a certain day. Each series of points represents a certain PRN. The points marked with “triangle” indicate the first point of the desired time sequence whiles the points marked with “diamond” are the last points.

This skyplot was plotted based on a series of text files (each for a given time) which are outputs of a Java program and are extracted from the site

www.calsky.com. Each text file consists of information of PRN number, azimuth and elevation angels, and ECEF coordinates. This information makes it useful not only for skyplot, but also for georeferencing specular points for static measurements.

4.1.2 Georeferencing specular points on Google Maps

Thanks to the Google Maps API [Google Maps API], specular points can be georeferenced on Google Maps by overlapping specular points on the extracted Google Maps images at a given location and at a given zoom. Figure 4-3 shows an example of specular points mapped on Google Maps. The location is the meadow of Piazza d'Armi of Turin, Italy and the time is the same as that in Figure 4-2. The receiver projection position is depicted by the big red triangle in the center of the figure and the receiver height above the surface is assumed to be 20m. The coordinate system applied in Figure 4-3 is Universal Transverse Mercator (UTM).

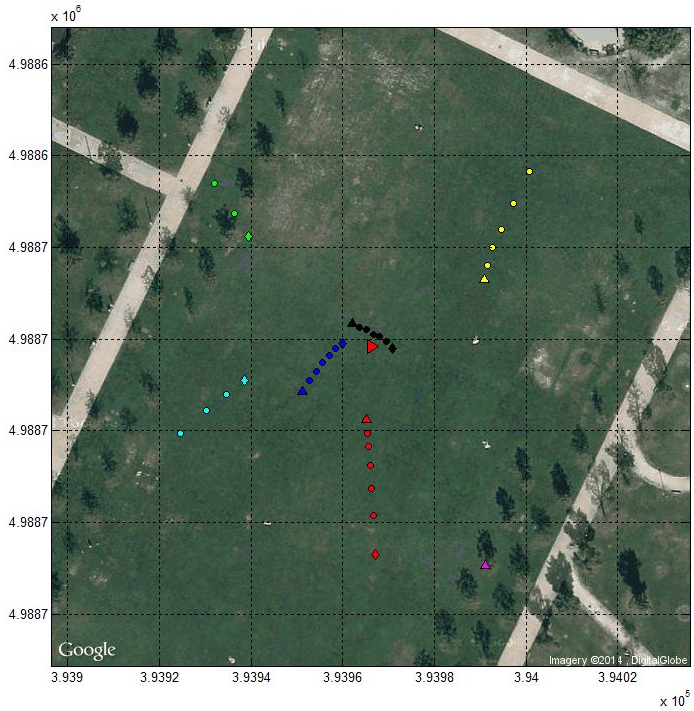

Figure 4-3 Specular points mapped on Google Maps

The mapping of specular points on Google Maps is useful when the receiver is high for example for flight measurements, since it provides the possibility to know the surface condition or coverage such as rivers, lakes, fields and buildings in order to better understand the reflection results.

4.1.3 Specular points on *x-y* plane with Fresnel zone

For some static measurements, especially when the receiver is only a few meters high above the ground, to know only the specular point position is usually not sufficient, the Fresnel zone coverage is sometimes crucial if the change of surface condition (soil moisture or roughness) is required or the measurement needs to be well controlled.

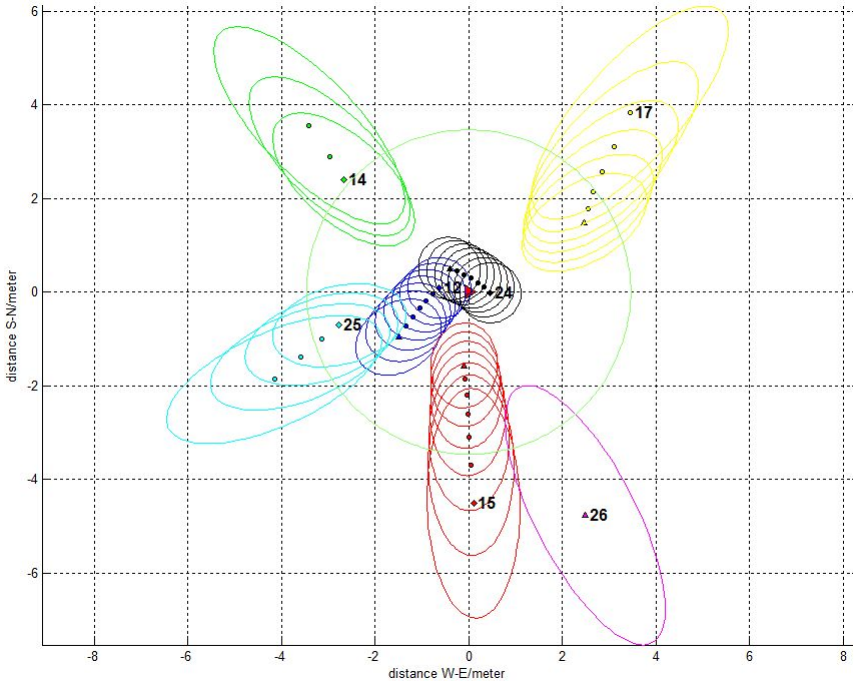

Figure 4-4 Specular points mapped on *x-y* plane with Fresnel zones and antenna footprint

Figure 4-4 shows an example of georeferencing specular points on *x-y* plane with Fresnel zones and antenna footprint. The simulated time and location are the same as those of Figure 4-3 but with the only difference of a 2 m antenna height above the ground. The receiver projection is in the origin represented by the big red triangle. Specular points are similar with those shown in Figure 4-3, but with their corresponding Fresnel zones surrounding them. The antenna footprint is depicted by the light green circle. The *x* axis represents the distance in meter in West-East direction whilst the *y* axis represents the distance in South-North direction.

The antenna footprint will change accordingly if the antenna changes its pointing direction in azimuth or elevation, which makes it useful for planning a measurement aiming at receiving reflection signals from certain PRNs.

4.1.4 Flight dynamics influence on antenna gain

Unlike the static situation where the incident angle to the antenna changes slightly and eventually during time, for a flight measurement, the incident angle of the reflected signal to the down looking antenna changes dramatically due to the flight dynamics in terms of yaw, pitch and roll (see Figure 4-5).

Therefore, this affect should be taken into account and an appropriate compensation of antenna gain should be implemented such as to avoid introducing further errors to the post processing phase.

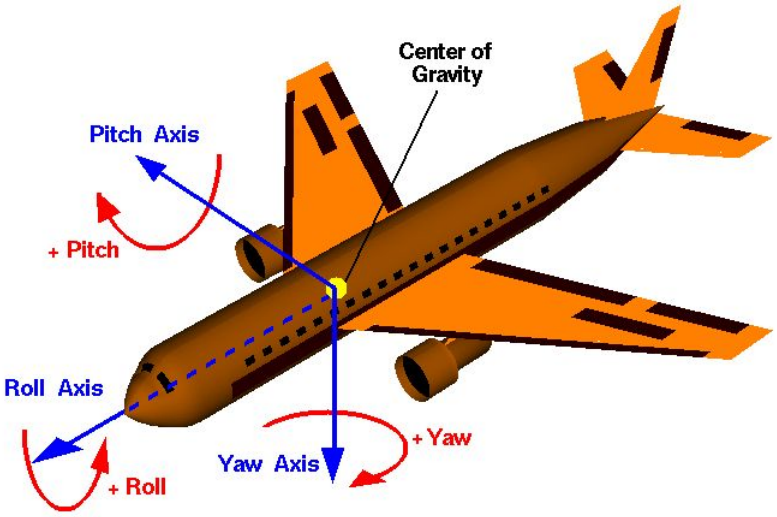

Figure 4-5 Flight dynamics- roll, pitch and yaw [Glenn Research Center, 2014]

The whole process of aircraft rotation in pitch, roll and yaw can be considered to be coordinate transformation. In the standard state (pitch, roll and yaw are 0°), vectors of roll (*x*), pitch (*y*) and yaw (*z*) axis can be defined in the ECEF frame given the aircraft position. After the rotations, new vectors of *x*, *y* and *z* can be obtained by multiplying the rotation matrixes, which are:

$$R_z(\sim)=\begin{pmatrix}\cos\sim & -\sin\sim & 0\\ \sin\sim & \cos\sim & 0\\ 0 & 0 & 1\end{pmatrix},\ R_y(\ )=\begin{pmatrix}\cos & 0 & \sin\\ 0 & 1 & 0\\ -\sin & 0 & \cos\end{pmatrix},\ R_x(¥)=\begin{pmatrix}1 & 0 & 0\\ 0 & \cos¥ & -\sin¥\\ 0 & \sin¥ & \cos¥\end{pmatrix} \quad (4\text{-}2)$$

where ~, and ¥ represent the yaw, pitch and roll rotation, respectively. The incident angle to the antenna is then straight forward as the angle between the antenna to the specular point vector and the new yaw axis (only in the case that the antenna pointing direction is parallel to the yaw axis).

Thanks to the Nimbus group who has provided a test flight data covering all the useful information including the flight dynamics, a trail of antenna gain compensation was implemented. Figure 4-6 shows the Nimbus UAV which performed the test flight.

Figure 4-6 Nimbus UAV

Figure 4-7 (a) shows traces of flight projection and specular points of PRN 25. Figure 4-7 (b) is the calculated incident angles to the down looking antenna after taking into account flight dynamics. Figure 4-7 (c) depicts the actual gain the antenna provided for different incident angles concerning the radiation pattern of the helix antenna shown in Figure 3-1. And Figure 4-7 (d) finally provides the gain compensation that should be given, considering the maximum gain of the helix antenna to be 10 dB.

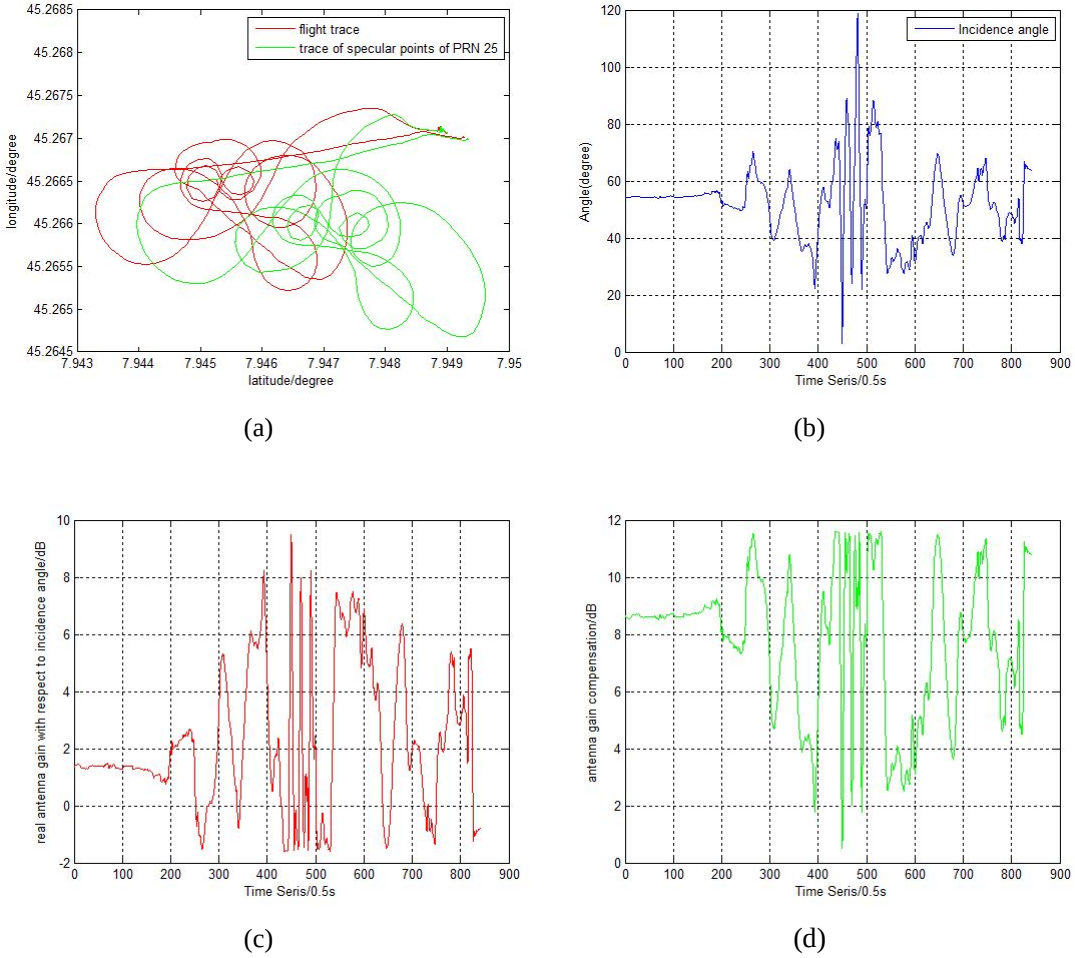

(a) (b)

(c) (d)

Figure 4-7 Antenna gain compensation results for Nimbus test flight

4.2 Signal post processing of raw data

4.2.1 Basic principles

The structure of GPS signals is briefly described in Chapter 2 and the two types of receivers are demonstrated in Chapter 3. The post processing is a software-defined-radio approach and is all done by Matlab installed in a standard PC. No matter which receiver was applied, recorded data were the same format of binary raw data with sampling frequency of 8.1838MHz and intermediate frequency of 38.4MHz since the same type of frontend was used.

Typically, to process a direct GPS signal, the incoming signal must be correlated with a locally generated replica C/A code with the appropriate phase offset and Doppler frequency shit and this process has been expressed in many literatures

such as [Misra and Enge, 2001]. In the case of reflected signal processing, it becomes sometimes simpler at least for this research by now, due to the reason that only the reflected signal power is of interest and other information such as navigation messages, carrier phase, delay and Doppler frequency can be ignored…

A flow diagram of this correlation process for 1ms (also known as coherent integration) is shown in Figure 4-8.

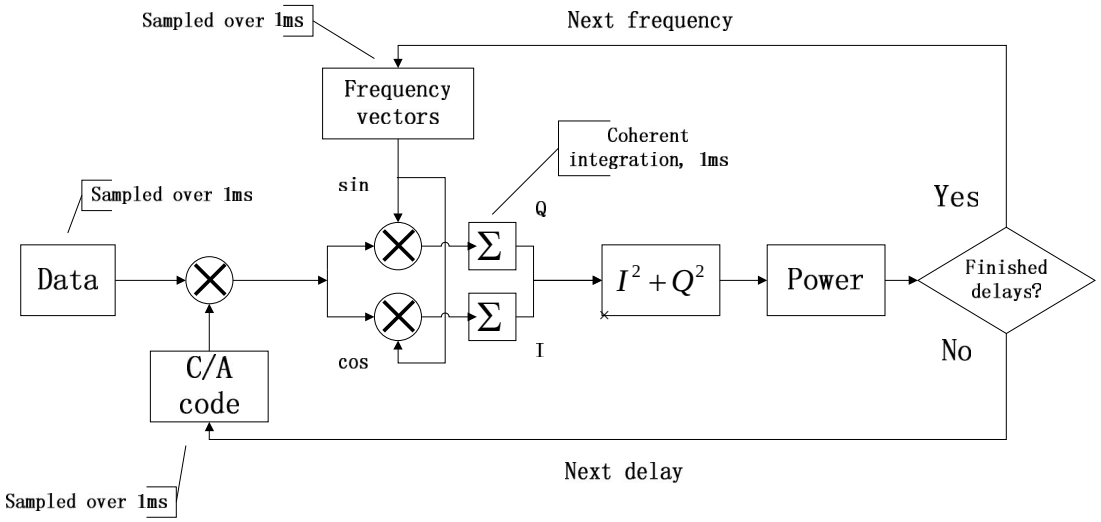

Figure 4-8 Flow diagram of basic correlation process for 1ms

The raw sampled data are collected by the receiver, the GPS C/A code sequence and the inphase and quadrature frequency vectors are all generated and sampled over the coherent correlation interval of 1ms. The code sequence (delay) consists of 8184 samples, as the sampling frequency is 8.1838MHz, and the frequency shift range is set to be from -10 kHz to +10 kHz, with 1 kHz step. The output at each delay and frequency bin is the single look signal power.

The flow diagram shown in Figure 4-8 is known as serial search, it is easy to realize but time consuming because it gets a single value of correlation function at each trail and the total time required is proportional to number of bins to explore. To speed up the processing and to reduce the complexity of serial search, the so called parallel search is used in our practice which is depicted in Figure 4-9.

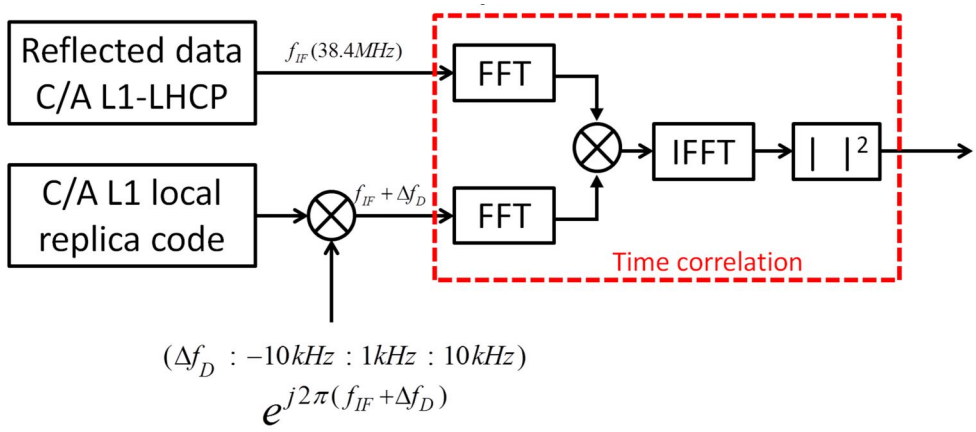

Figure 4-9 Flow diagram of correlation using parallel search

The parallel search method shown in Figure 4-9 uses Fast Fourier Transforms (FFT) to perform correlations at all delays for a given frequency in one step. The operations are illustrated as following.

- A set of 8184 samples of the incoming signal and of the local code is buffered
- The FFT of the sample sets is evaluated
- The transformed sequences are multiplied
- The IFFT is evaluated in order to estimate the correlation function
- The output of IFFT is squared in order to get the correlation power

To scan over all the steps of frequency shift, the correlation power for each delay and frequency bin can be generated and can be shown in a 3-D figure which is the so-called Delay Doppler Map (DDM) illustrated in the following section.

4.2.2 Delay Doppler Maps and Delay Waveforms

The correlation power mapped in a grid including the delays and Doppler frequencies is called the Delay Doppler Map. An example is given in Figure 4-10, the peak correlation power has been normalized to 1, which is seen to be the signal power, and the surrounding blue noisy background is noise power distributed in other delays and frequencies.

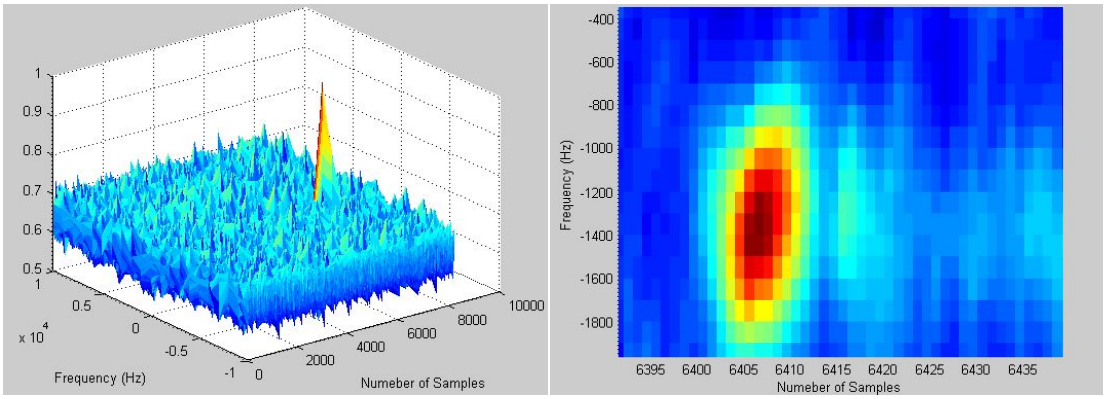

(a) (b)

Figure 4-10 Delay Doppler Map. (a) 3 Dimensional DDM. (b) 2 Dimensional DDM of (a) observed from z axis

Delay Waveform (DW) is the returned power profile as a function of delay only, with the frequency set to a constant value (normally the value at the specular point). A direct signal will have a sharp triangle shape, as a result of the GPS correlation process. However, a reflected signal will sometimes exhibit a spreading in delay as power is detected at different delays over the glistening zone. DW can be obtained from DDM by extracting the delay row at the Doppler frequency where the correlation peak presents. Figure 4-11 gives an example of Delay Waveform.

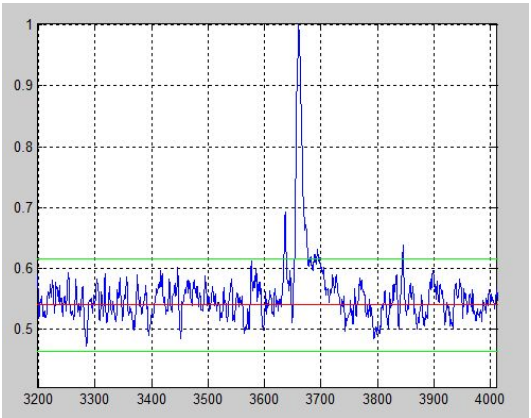

Figure 4-11 Delay Waveform

The red lines in Figure 4-11 implies the average noise floor calculated in the region of 8 samples before and 24 samples after the peak, while the two green lines show a region of noise floor plus and minus 3 times of the noise standard deviation, where nearly all the noise power should fall in theoretically assuming the noise is Gaussian noise. The calculation of noise floor is used for evaluating the signal to noise ratio (SNR) which is illustrated in Section 4.2.4.

It should be noted that, in order to get more precise DW, the coarse search DDM shown in Figure 4-10 is not used directly for extracting DW. A refined search DDM is calculated by reducing the frequency step to 100 Hz (21 or less frequency steps which are centered at the frequency where the peak appears in a coarse search DDM). DW is further extracted from this refined search DDM.

4.2.3 Non coherent integration

As shown in Section 4.2.1, a coherent integration (normally 1 ms, determined by the length of the GPS PRN code sequence) must be performed to get DDM and DW. Coherent means that the signal is processed using both its in-phase and quadrature signal components, with the possibility of computing a carrier phase angle based on these two values. However, all phase information is lost when the signal power magnitude is computed using the square of the in-phase I and quadrature Q signal components, as shown in Figure 4-9. It is believed that the phase of the signal received has been observed to be unpredictable and not related to the transmitted GPS carrier phase and the signal power magnitude only is the primary observable.

Generally, due to the attenuation of signal power caused by surface reflection and the presence of fading noise introduced by surface scattering, 1 ms of integration is not enough to get the correlation peak, consecutive 1 ms coherent correlations must be averaged. This process is known as the non coherent integration. Figure 4-12 shows the diagram of this process.

This necessitates that the whole process shown in Figure 4-9 be repeated over several consecutive milliseconds of raw data. For every trial delay and Doppler frequency, consecutive milliseconds are summed together as illustrated in Figure 4-12. This has the effect of mitigating the fading or speckle noise caused by the random scattering and results in a better estimate of the true signal power.

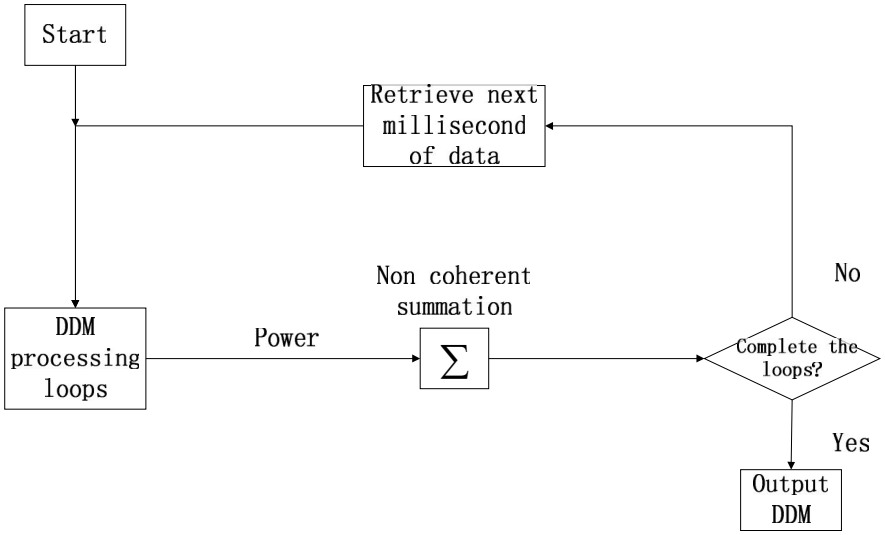

Figure 4-12 Diagram of non coherent integration over consecutive 1 ms

Carefully choosing of an appropriate non coherent integration time is important since SNR will be influenced by the choice of a too long or too short non coherent integration time. There is not a defined rule governing the choosing but it should only be determined by the specific application and by its own situation. In this thesis, 500 ms of non coherent integration time is used since it's examined to be long enough to eliminate the effects of speckle noise and short enough to have good resolution of the surface by multiple experiments.

4.2.4 SNR and received signal power

As shown from the DW in Figure 4-11, the total peak power is normalized to 1 and the average noise floor is evaluated represented by the red line. The processed absolute SNR (the ratio between the pure signal and the noise powers) is then simply expressed as

$$\Phi_{peak} = \frac{1 - \overline{P_N}}{\overline{P_N}} \tag{4-3}$$

where Φ_{peak} is the absolute Signal to Noise ratio and $\overline{P_N}$ is the average noise value (see Figure 4-13)

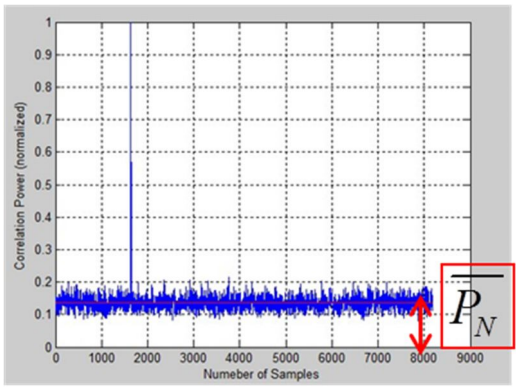

Figure 4-13 Average noise floor $\overline{P_N}$ in Delay Waveform

The SNR of the received signal for a given delay and a given Doppler frequency can be written as:

$$\Phi\left(\tau, \hat{f}\right) = \frac{G_D \cdot P_S \cdot \Lambda^2\left(\tau - \tau\right) \cdot S^2\left(\hat{f} - f\right)}{P_N} \tag{4-4}$$

where P_S and P_N are signal and noise power before despreding. Ambiguity functions Λ and S represent the "attenuation" due to power correlation misalignments, in delay and frequency, G_D is the so called processing gain (~ 30.1 dB) due to the de-spread of the GPS C/A code, P_N is the input noise power. This can be expressed as

$$P_N = kT_N B_w \tag{4-5}$$

where k is the Boltzmann's constant, k=1.380×10-23 J/K, T_N is the estimate of the receiver noise equivalent temperature (which can be approximated as $T_N = (NF - 1)290$), NF (dB) is the receiver noise figure (it can be estimated in the range of 1.0-2.5 dB) and $B_w = 1/T_I$ is the signal bandwidth determined by the coherent integration time T_I (1 ms in our case). The input noise power can be approximated as $P_N = -176.3dBW$.

For the case of peak SNR Φ_{peak}, the attenuation factor due to the ambiguity function $\Lambda^2\left(\tau - \tau\right) \cdot S^2\left(\hat{f} - f\right)$ is close to 1. Therefore, Eq. 4-4 can be simplified and transformed as:

$$P_S = \frac{\Phi_{peak} \cdot P_N}{G_D} \tag{4-6}$$

As Φ_{peak} can be calculated from DW using Eq. 4-3, P_N and G_D are known parameters, the received signal power P_S can be obtained.

Chapter 5 Soil moisture retrieval and measurements

5.1 Dielectric constant

The dielectric properties of moist soils are important in determining the microwave scattering and absorption by a soil medium [Dobson and Ulaby, 1986]. In general, a soil medium can be treated as a volume consisting of variable fractions of soil solids, aqueous fluids, and air. Soil solids are characterized by the distribution of particle sizes (texture) and the mineralogy of their constituent particles (particularly the clay fraction). Ideally, an eloquent model formulation would account for the observed effects of various soil components on the complex dielectric behavior of the soil-water-air system as a function of frequency. Such factors would include soil bulk density (compaction), soil composition (particle size distribution and mineralogy), the volume fraction of soil water components, the salinity of the soil solution, and temperature [Dobson, 1985].

An example of the frequency response of soil dielectric properties is shown in Figure 5-1.

There are two ways to describe the wetness of soil, which are determined by percentage by dry weight or by volume basis,

$$m_v = \frac{V_w}{V_t} = \frac{V_w}{V_{dry}} = \frac{W_w}{W_{dry}} \frac{°_b}{} cm^3 \cdot cm^{-3} \tag{5-1}$$

$$m_g = \frac{W_w}{W_{dry}} \times 100\% = 100 \frac{m_v}{°_b} (\%) \tag{5-2}$$

where W_w is the weight of the water in the sample; W_{dry} is the weight of the solid part of the sample; V_w is the volume of the water; V_{dry} is the volume of the solid part of the sample; V_t is the total volume of the sample, assuming it's equal to the volume of the solid part as the water takes place of the air and doesn't increase the total volume; $°_b$ is the density of the sample mixture.

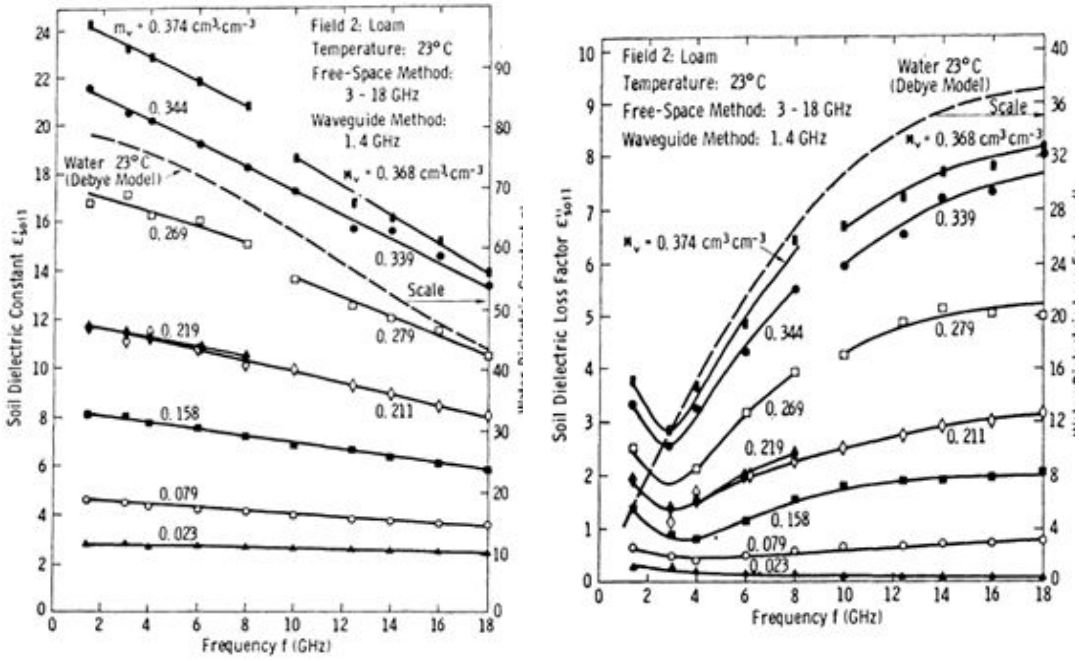

a) b)

Figure 5-1 Measured a) real part and b) imaginary part of the dielectric constant as a function of frequency with volumetric wetness as a parameter [Dobson and Ulaby, 1986]

Because the dielectric constant of moist soils is proportional to the number of water dipoles per unit volume, the preferred measure for soil moisture is volumetric which is expressed in Eq. 5-1.

The empirical model shown by [Hallikainen, 1985] is used to calculate the soil moisture staring from the dielectric in function of coefficients depending on the frequency and on the soil composition. It's known as polynomial expressions and is generated for ε' and ε'' as a function of m_v for each frequency and soil type. At each frequency, the individual polynomials are then combined into a single polynomial that expresses ε, as a function of m_v, *S* and *C*, where *S* and *C* are the sand and clay textural components of a soil in percent by weight, respectively. A few soil types with different compositions of sand, silt and clay are listed in Table 5-1.

Table 5-1 Soil texture composition of different soil samples

Soil Type	Soil Texture (%)		
	Sand	Silt	Clay
Sandy Loam	51.51	35.06	13.43
Loam	41.96	49.51	8.53
Silt Loam	30.63	55.89	13.48
Silt	17.16	63.84	19
Silty Clay	5.02	47.60	47.38

The general form of the polynomial is,

$$£ = (a_0 + a_1 S + a_2 C) + (b_0 + b_1 S + b_2 C) m_v + (c_0 + c_1 S + c_2 C) m_v^2 \qquad (5\text{-}3)$$

Some research has been done to provide the coefficients of the polynomial above at each frequency and shown great agreement between the measured $£_m$ and the predicted one $£_c$ using Eq. 5-3 with some given coefficients at each frequency.

For the study of remote sensing in the L-band, we consider the coefficients in the row of frequency 1.4 GHz. The polynomials for the dielectric constant then are,

$$\begin{aligned} £' &= (2.862 - 0.012S + 0.001C) \\ &+ (3.803 + 0.462S - 0.341C) m_v + (119.006 - 0.5S + 0.633C) m_v^2 \end{aligned} \qquad (5\text{-}4a)$$

$$\begin{aligned} £'' &= (0.356 - 0.003S - 0.008C) \\ &+ (5.507 + 0.044S - 0.002C) m_v + (17.753 - 0.313S + 0.206C) m_v^2 \end{aligned} \qquad (5\text{-}4b)$$

Figure 5-2 is the different permittivity characteristics (both real part and imaginary part) obtained in function of m_v for different soil decomposition (Sand, Loam, Organic, Ferromagnetic and Clay)

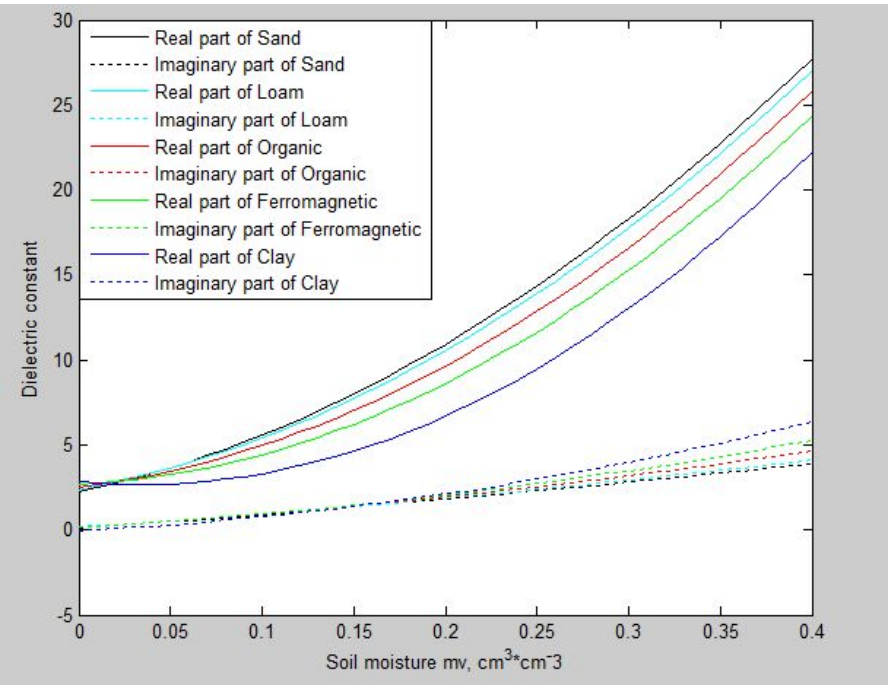

Figure 5-2 The dielectric constants versus volumetric water content for 5 different types of soil at 1.4 GHz.

It can be seen from Figure 5-2 that at L band (1.4 GHz) both real and imaginary part of the dielectric constant grow with the increase of soil moisture for all the 5 types of soils. Moreover, the real part has very apparent increase while on the contrary, the imaginary part doesn't tend to change much.

5.2 Dielectric constant retrieval through LHCP

5.2.1 Retrieval process

The retrieval process basically aims to establish the link between received LHCP reflected signals and dielectric constant of the soil. As the dielectric constant is strongly influenced by soil moisture and there're already several mature models which have built their relationship, such as the empirical model of [Hallikainen, 1985] described in the previous section, the retrieval of dielectric constant is the key component to the retrieval of soil moisture. For specular reflection case, the reflected GPS signals are predominately LHCP [Masters, 2004], especially for higher elevation of satellite (smaller incident angle). Therefore, Section 5.2 only concerns the retrieval of dielectric constant from reflected LHCP signals, assuming

a perfectly smooth surface, regardless the surface roughness and incoherent components.

The retrieval starts from the fundamental theories of electromagnetic waves. The electric fields of LHCP and RHCP can be expressed as a combination of two orthogonal linear polarizations, such as horizontal and vertical polarizations:

$$\mathbf{E}_l = |E_l|(\vec{x} + j\vec{y}) \tag{5-5}$$

$$\mathbf{E}_r = |E_r|(\vec{x} - j\vec{y}) \tag{5-6}$$

where $\mathbf{E}_l$ and $\mathbf{E}_r$ are the electric field vectors of LHCP and RHCP. Subscripts l and r denote LHCP and RHCP, respectively. And the same definition of subscripts is used in the following equations. $|E_l|$ and $|E_r|$ are the magnitudes of LHCP and RHCP fields. $\vec{x}$ and $\vec{y}$ are unit coordinate vectors and represent the two orthogonal linear polarizations' directions. In this thesis, they are fixed to be horizontal and vertical polarizations, respectively. Since any field can be represented by two circularly polarized components-LHCP and RHCP, the total reflected field of RHCP transmitted GPS signal is a combination of LHCP and RHCP fields, shown in:

$$\mathbf{E} = |E_r|(\vec{x} - j\vec{y}) + |E_l|(\vec{x} + j\vec{y}) \tag{5-7}$$

which can be rewritten in another form:

$$\mathbf{E} = (|E_l| + |E_r|)\vec{x} + j(|E_l| - |E_r|)\vec{y} \tag{5-8}$$

As $\vec{x}$ and $\vec{y}$ represent horizontal and vertical polarizations, the magnitudes of horizontal and vertical polarizations are obtained:

$$|E_h| = |E_l| + |E_r| \tag{5-9}$$

$$|E_v| = |E_l| - |E_r| \tag{5-10}$$

where the subscripts of *h* and *v* denote horizontal and vertical polarizations. The equation of power density and field strength is expressed as:

$$\sqrt{P} = |E| / \sqrt{Z_0} \tag{5-11}$$

Therefore, the relationship of power density between circular polarizations (RHCP, LHCP) and linear polarizations (horizontal and vertical polarizations) are:

$$\sqrt{P_l} = \frac{1}{2}(\sqrt{P_h} + \sqrt{P_v}) \tag{5-12}$$

$$\sqrt{P_r} = \frac{1}{2}(\sqrt{P_h} - \sqrt{P_v}) \tag{5-13}$$

Our interest and measurement are in reflected LHCP signals, which can be expressed as:

$$\sqrt{P_{lr}{}^r} = \frac{1}{2}(\sqrt{P_h{}^r} + \sqrt{P_v{}^r}) \tag{5-14}$$

where the subscript *lr* represent RHCP transmitted and LHCP received signal. The following subscripts are defined in the form which is coherent with the explanation of Eq. 2-5. The superscript *r* denotes "received" power. Moreover, as demonstrated in [De Roo and Ulaby, 1994], for specular reflection, the coherent power exists only for co-polarized scattering, which means:

$$P_{qp} = \Gamma_{qp} = 0 \text{ if } p \neq q \tag{5-15}$$

where subscripts *p* and *q* denote vertical or horizontal polarizations and Γ is Fresnel reflection coefficient. This means that cross-polarization components of $P_{hv}{}^r$ and $P_{vh}{}^r$ don't exist and Eq. 5-14 can be written as:

$$\sqrt{P_{lr}{}^r} = \frac{1}{2}(\sqrt{P_{hh}{}^r} + \sqrt{P_{vv}{}^r}) \tag{5-16}$$

The Fresnel reflection coefficients for *hh* and *vv* are already well known as:

$$\Gamma_{hh}(¥) = \frac{\sin ¥ - \sqrt{£_r - \cos^2 ¥}}{\sin ¥ + \sqrt{£_r - \cos^2 ¥}} \tag{5-17}$$

$$\Gamma_{vv}(¥) = \frac{£_r \sin ¥ - \sqrt{£_r - \cos^2 ¥}}{£_r \sin ¥ + \sqrt{£_r - \cos^2 ¥}} \tag{5-18}$$

where Γ is the Fresnel reflection coefficient, $£_r$ is the relative dielectric constant.

¥ = 90° − ¯ is the grazing angle, and ¯ is the incident angle. Therefore, combining the definition of bistatic radar equations for coherent component shown by Eq. 2-6, Eq. 2-8 and power density relation shown in Eq. 5-16, the equation expressing the relation of received LHCP power and Fresnel coefficients of *hh* and *vv* is obtained:

$$\sqrt{P_{lr}^{\ r}} = \frac{1}{2}\sqrt{\frac{P^t G^t}{4\pi (R_1+R_2)^2}\frac{G^r \lambda^2}{4\pi}}\sqrt{\exp\left[-\left(\frac{4\pi\sigma_h \cos\theta}{\lambda}\right)^2\right]}\left(\left|\Gamma_{vv}\right|+\left|\Gamma_{hh}\right|\right) \quad (5\text{-}19)$$

Considering the specular reflection on a perfectly smooth surface, the surface roughness attenuation expressed by $\exp\left[-\left(4\pi\sigma_h \cos\theta/\lambda\right)^2\right]$ can be neglected and be approximated as 1. Further, the incoherent component doesn't play a role in specular reflection and therefore the total received LHCP power is the coherent component of LHCP (in Eq. 2-9, the P_{qp}^{i} component is 0). As the total received signal power P_S can be obtained by post processing shown by Eq. 4-6, the final expression linking received signal power and dielectric constant is:

$$P_{lr}^{\ r} = P_S = \frac{1}{4}\frac{P^t G^t}{4\pi (R_1+R_2)^2}\frac{G^r \lambda^2}{4\pi}\left(\left|\Gamma_{vv}\right|+\left|\Gamma_{hh}\right|\right)^2 \quad (5\text{-}20)$$

where Fresnel reflection coefficients of *hh* and *vv* are given in Eq. 5-17 and Eq. 5-18, which are functions of dielectric constant and grazing angle.

By combining Eq. 5-17, 5-18 and 5-20, the only unknown parameter is ε_r and it is solvable. However, the solved ε_r is a real number indicating the modulus of the complex dielectric constant consisting real and imaginary parts:

$$\varepsilon_r = \varepsilon_r' + j\varepsilon_r'' \quad (5\text{-}21)$$

To separate the real and imaginary parts, one possible solution is to consider one of the dielectric models, for instance the model of [Hallikainen, 1985] shown by Eq. 5-4a and 5-4b. By pre-choosing the soil composition parameters S and C in Eq. 5-4a and 5-4b, and combining Eq. 5-17, 5-18, 5-20, 5-21, 5-4a and 5-4b, three unknowns of ε_r', ε_r'' and soil moisture m_v can be all solved.

5.2.2 Fight measurement

5.2.2.1 Description

A flight measurement campaign was performed in collaboration with the NAVSAS group of Politecnico di Torino to acquire data from a rice field region of Piedmont, Italy. The aircraft and the down-looking LHCP antenna are shown in Figure 5-3. The receiver was mounted on an aircraft flying at about 700 m above ground level at a speed of around 200 km/h. The geometry of this flight measurement is shown in Figure 5-4.

Figure 5-3 The aircraft used (left panel) and down-looking LHCP antenna (right panel)

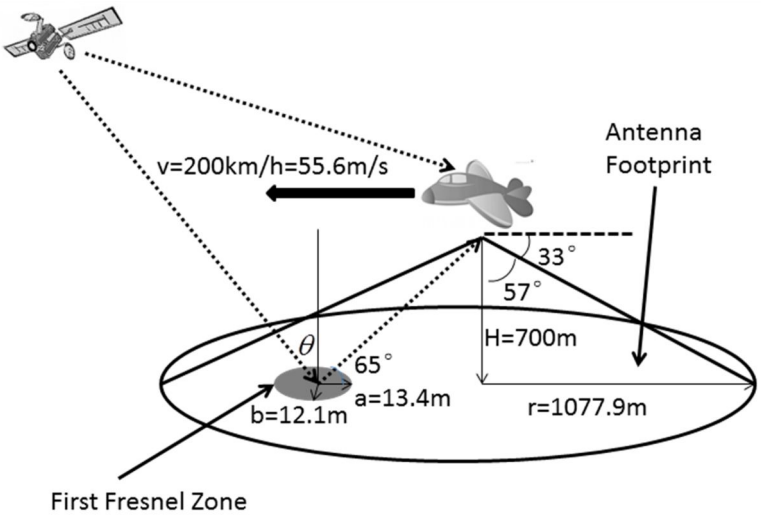

Figure 5-4 Flight measurement geometry

As shown in Figure 5-4, The area of the first Fresnel zone (highlighted in grey) due to a signal received from a GPS satellite with an elevation angle of 65° can be estimated at around 510 m^2 following the equations given by Eq. 2-3 for the evaluation of semi-major and semi-minor axis of the Fresnel ellipse. The antenna

footprint dimension during the entire flight was estimated to be around 3 km^2 which is depicted by the big black ellipse and therefore, all the coherent contributions to the received power coming from the first Fresnel zone can be always detected.

During the flight, direct GPS signals were received by a zenith-pointing RHCP antenna and reflected GPS signals by a nadir-pointing LHCP antenna. The receiver system configuration is shown in Figure 5-5.

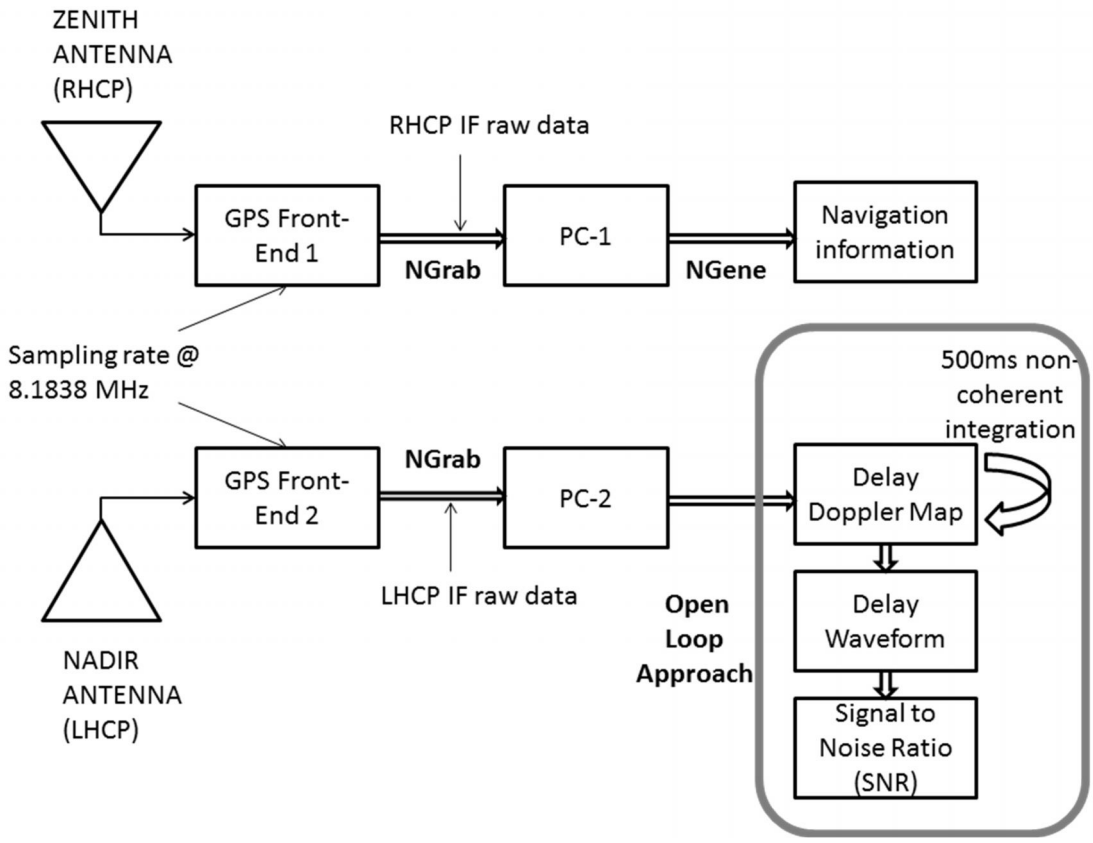

Figure 5-5 Flowchart of system configuration

The hardware descriptions are given in Chapter 3 and the PC based receivers were applied. The so called “Open Loop Approach” represented by grey box in Figure 5-5 is explained in Chapter 4 and a 500 ms of non coherent integration time was chosen for this measurement.

A video camera for visual inspection of flooded fields was also mounted on board the aircraft. Some rice fields were flooded during the measurements, creating an ideal scenario to study reflection signatures. Two flights were performed: a test flight and a final flight (denoted by yellow and red, respectively, in Figure 5-6).

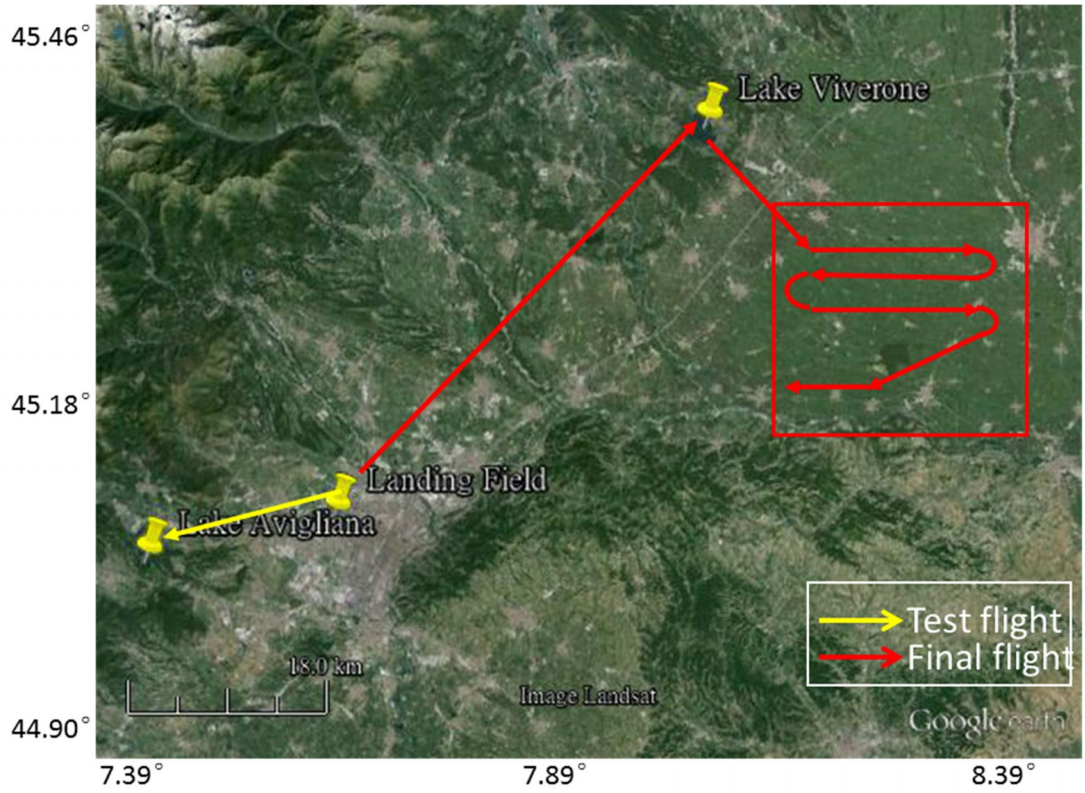

Figure 5-6 Entire flight plan: the red box marks the over-flown rice fields

In the northern portion of the flight path (shown by red line), a lake (Viverone Lake) was over-flown. Data taken from reflections occurring on the lake surface were used to calibrate the received power, since not all the system parameters (transmitter and receiver antenna's gain, transmitted power, receiver noise…) were accurately known. Fixing the dielectric constant of the water to be constant to 80 (in the L band, for fresh water at 25°C it is equal to 78.5 [Ulaby, 1986]), Fresnel reflection coefficients and power reflectivity values were directly evaluated, allowing the system parameters to be estimated and corrected, especially the receiver noise power (see Eq. 4-6 and Eq. 5-20). The received signal power and dielectric constant over the rice fields were then calculated and derived referenced to the calibrated system parameters.

Prediction of the satellites in view during the flight is an important task for selecting the optimal flight route. The predicted skyplot was analyzed and all satellites with elevation lower than 33° were discarded because, for these satellites, the specular reflections did not fall within the LHCP nadir-looking antenna footprint (the half-power beam width of the antenna used is about 114°). As an

example, one of the skyplots evaluated for the flight is shown in Figure 5-7.

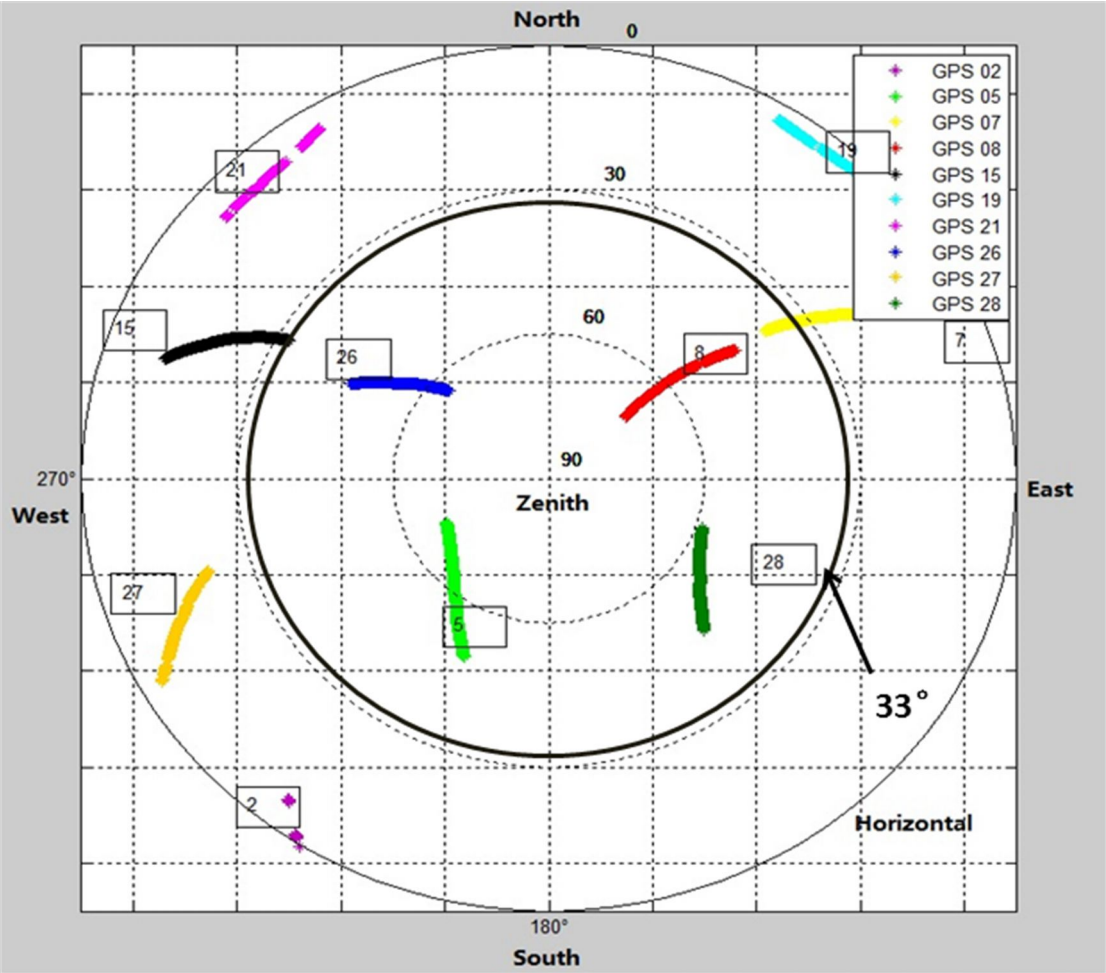

Figure 5-7 Predicted skyplot of GPS satellites positions during the flight period

In Figure 5-7, all predicted GPS satellite positions are shown, but only four satellites (PRN 5, 8, 26 and 28) providing a potentially useful reflection signature were available, whose positions fell inside the 33° mask depicted by solid black circle in the figure.

5.2.2.2 Results

SNR values obtained overflying several areas are shown in Figure 5-8 and Figure 5-9. The solid line indicates the flight track, while dotted lines are the corresponding tracks of specular points available from different satellites. During the overall flight, reflections from signals transmitted by PRN 5, 8, and 26 were continuously available and provided useful reflected signatures.

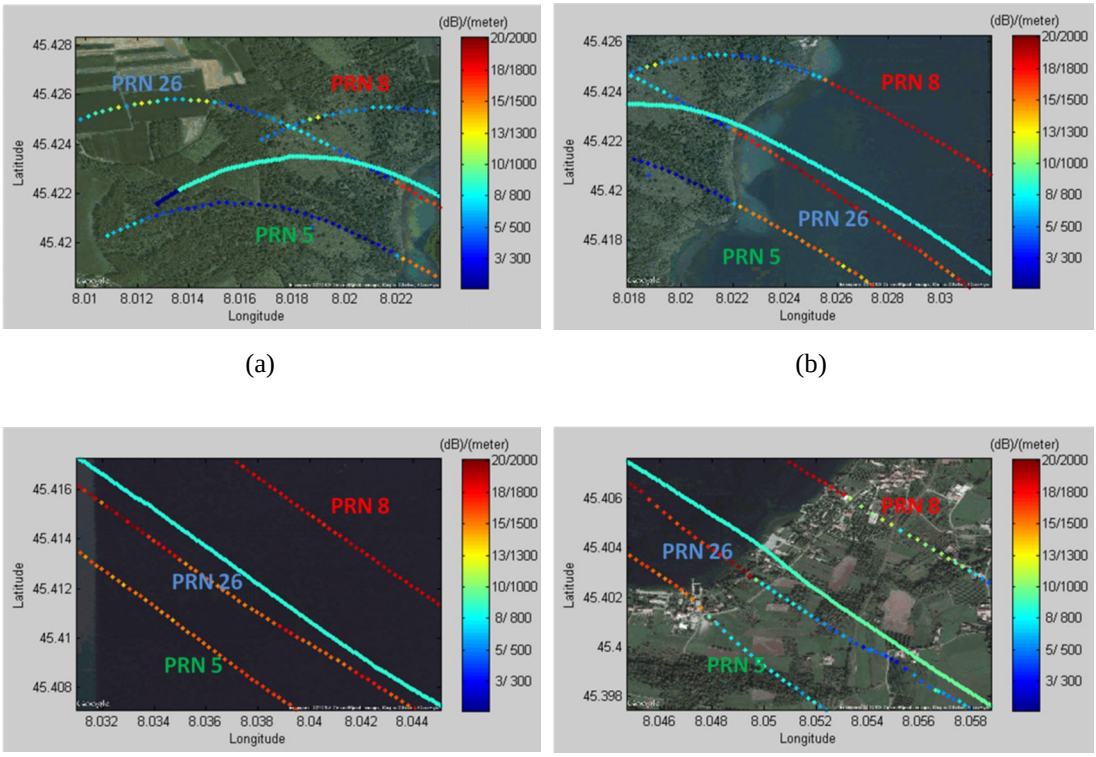

Figure 5-8 SNR values (in dB) measured from three different available reflections overflying Lake Viverone.

In particular, reflections occurred over the lake surface and used to calibrate the system are depicted in Figure 5-8. The four images show the SNR time series values (in dB) measured for each of the useful reflected signals in view. An abrupt SNR change in proximity to the transition between ground and water is noted. In fact, during the Lake Viverone overflight, stable (18 – 20 dB) and very similar SNR values were observed from the three available signals, in contrast to occasions when specular reflection points were over land.

An example of the SNR time series over rice fields is shown in Figure 5-9, co-located again on the Google map. Figures 5-9 (a) to (e) are representative of overflight of five adjacent rice fields. For all these figures, quantitative values of SNR (dB)/flight height (m) are provided in the legend. It is interesting to note the high sensitivity of the receiver to different wet conditions: a dynamic of 15 – 20 dB is recorded. Note also the high coherency between signals acquired by two satellites whose tracks were very close to each other (see the two specular point tracks to the north). The change in positional displacement of the specular

reflection points for signals coming from the three different satellites shown in Figure 5-9 (d) is due to the variation in flight height from about 800 to 1200 m.

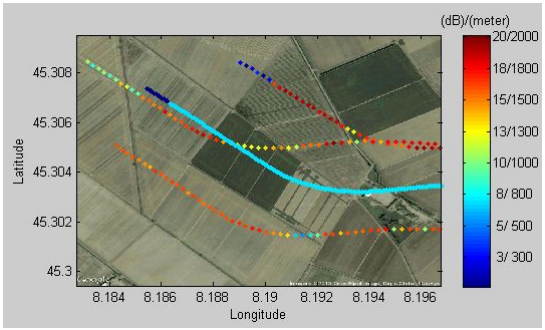

(a)

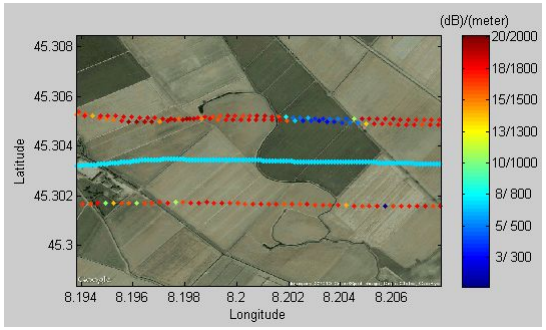

(b)

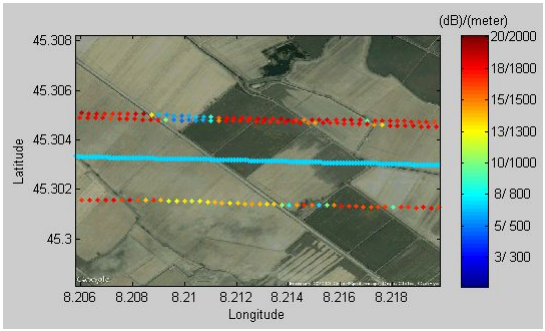

(c)

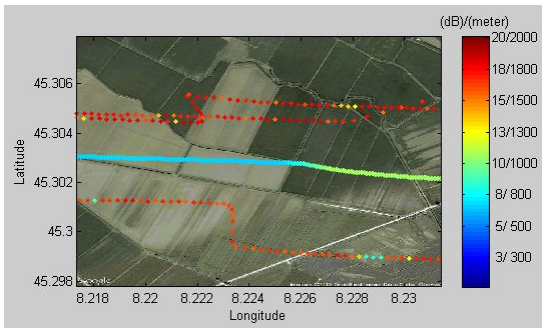

(d)

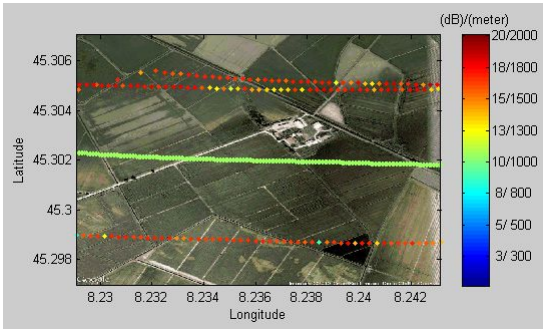

(e)

Figure 5-9 Processed SNR from specular tracks overflying rice fields. The unbroken line is the projected flight path (colours provide information on flight altitude).

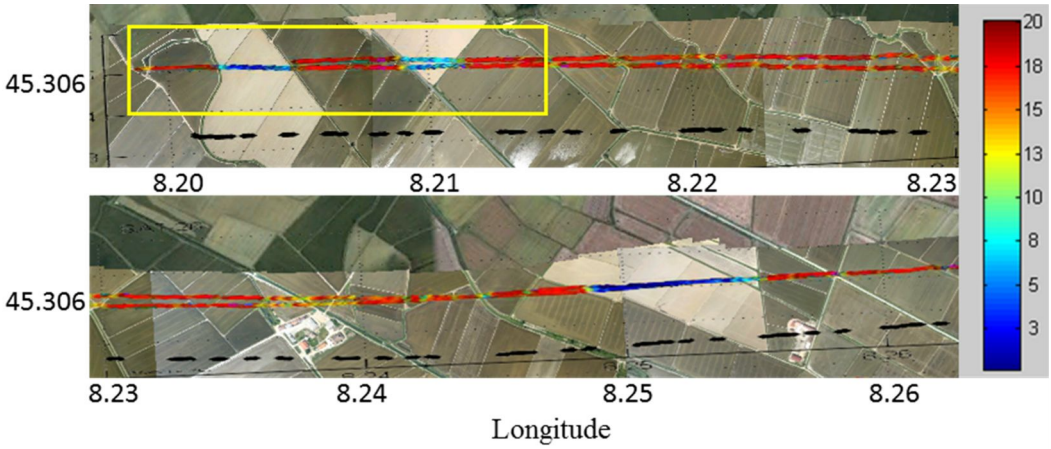

Figure 5-10 SNR time series superimposed on an image taken by the co-located video camera. Yellow inset corresponds to ground portions shown in Figure 5-9 (b) and (c)

The evidence for different soil moisture levels is provided in Figure 5-10. The upper and lower images show two adjacent images taken by the video camera co-located to the LHCP GPS antenna. Here, SNR time series are co-located and superimposed on the image. Ground portions completely filled by water can easily be recognized in the image (sun glitter is evident). Reflections over these parcels (darker in the image) are characterized by higher SNR values in contrast to reflections occurring over dry parcels (brighter background in the image). The black dotted line denotes the flight route. The ground portion within the yellow inset is that shown in Figure 5-9 (b) and (c).

On account of the calibration procedure applied to the collected data, an initial attempt to estimate relative dielectric constant was made through the retrieval method illustrated in Section 5.2.1 for LHCP reflected signals. Note that the goal of this measurement initiative was to investigate the sensitivity of this technique to water changes on the ground. The flight was performed over lake surfaces and rice fields almost completely covered by water. For this reason, the effects of soil roughness on received power were ignored. And also the retrieved dielectric constants were solved from equations of Eq. 5-17, Eq. 5-18 and Eq. 5-20 as a real value without separating the real and imaginary parts.

Results related to the ground portion within Figure 5-10 (yellow inset) and to the wider over-flown area identified in Figure 5-9 (a-e) are shown respectively in Figures 5-11 and Figure 5-12 (a-e).

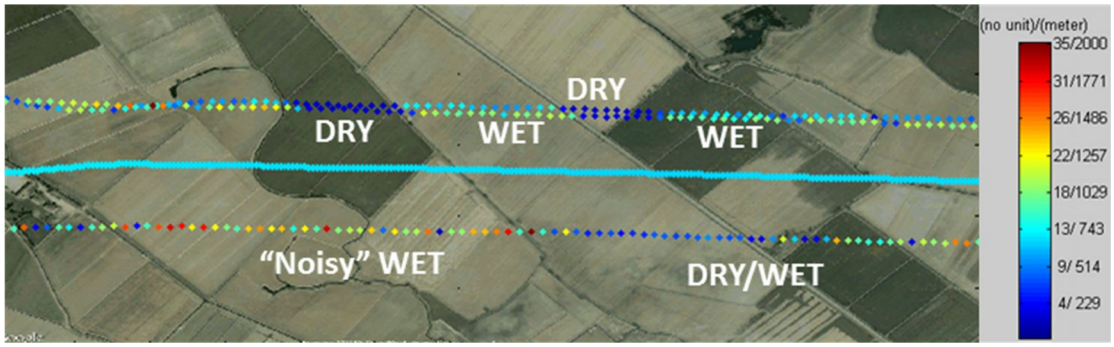

Figure 5-11 Estimated relative dielectric constant of the ground parcels shown in Figure 5-10 (yellow inset).

In this case, colors are associated with both the dielectric constant (left-hand figures in the legend) and flight height (right-hand figures). The numbers obtained after inversion appear to be too small. Since we were not sure of the water saturation level of the rice fields (even though sun glitter evidenced the presence of water), dielectric constants less than 80 appear to be reasonable. Variations justify the absence/presence of water information and a good correlation between dielectric constant values and field flooding status was obtained.

All the SNR results show to be quite sensitive to the water content of the terrain and can readily be used to detect and monitor areas where water is present or not. Retrieved dielectric constant values are coherent with the surface moisture condition (flooded or not) and due to the lack of in-situ soil moisture measurements, only the trend of dielectric constant change was verified to match the real time surface moisture and its accuracy hasn't been tested.

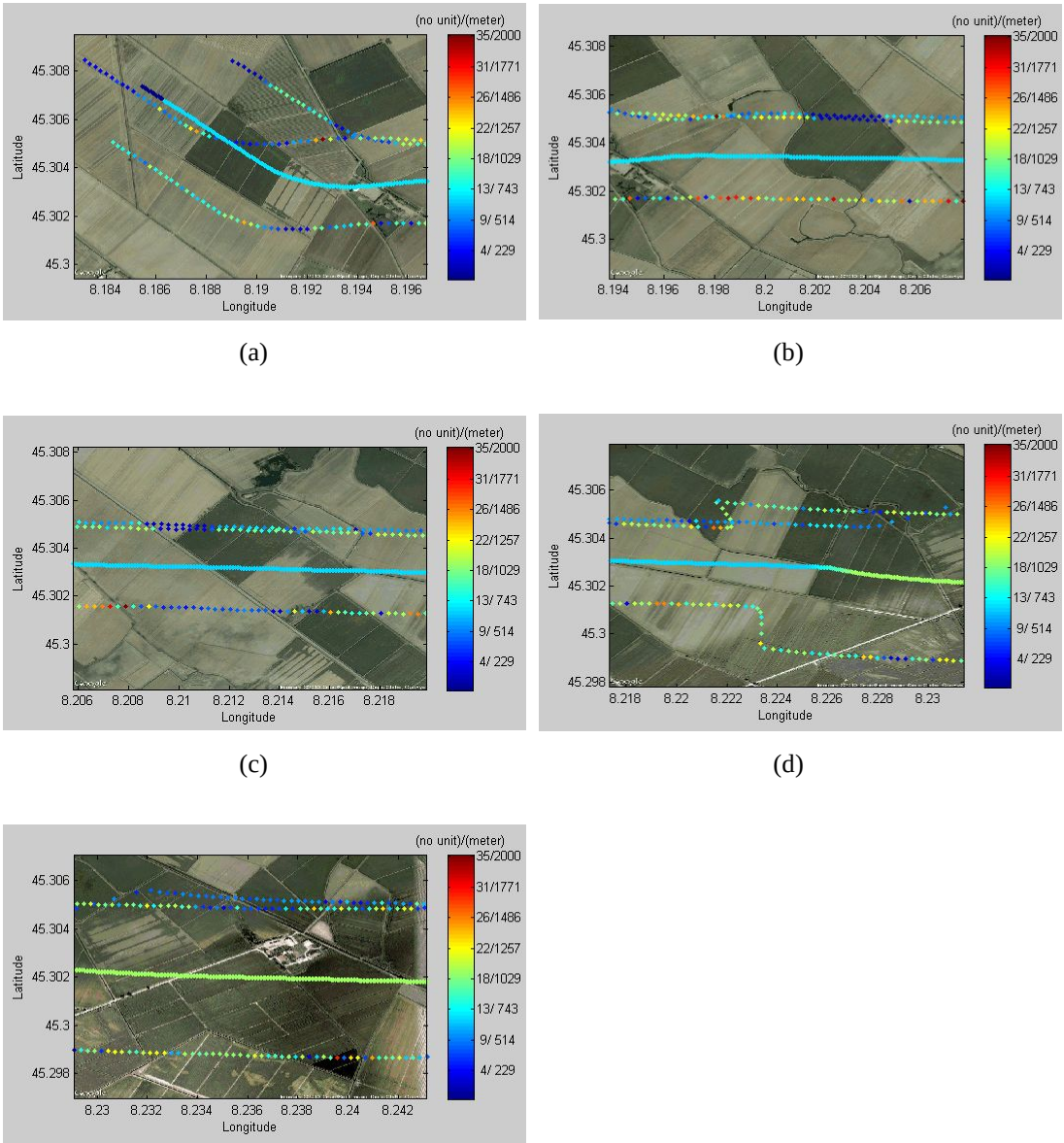

(a) (b)

(c) (d)

(e)

Figure 5-12 Estimated relative dielectric constant of rice fields corresponding to Figure 5-9

5.2.3 Static measurements

5.2.3.1 Description

As described in Chapter 3, a more compact solution of the receiver previously described capable to be installed on-board UAVs was designed and developed, and it's the Hackberry board based receiver. In what follows, preliminary results of two test campaigns carried out from static positions will be described. In both cases, the receiver was placed at about 3 m from a sandy terrain. The measurement geometry

was depicted in Figure 5-13

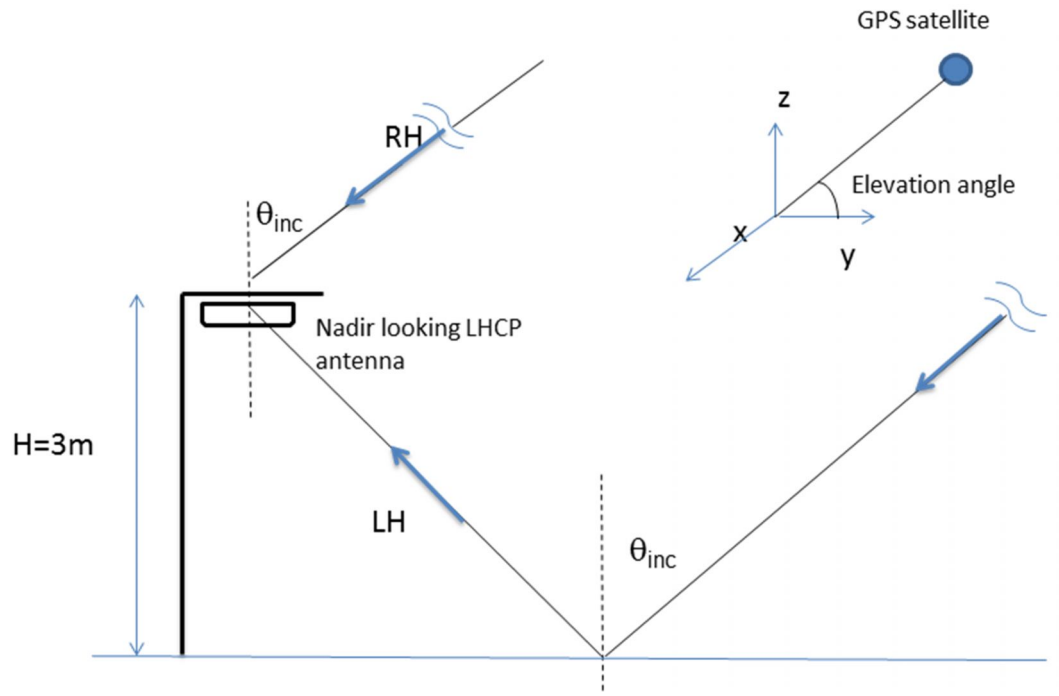

Figure 5-13 Static measurement geometry

These experiments were planned in order to verify the sensitivity of the receiver (in terms of estimated SNRs level) to different soil moisture levels, relative dielectric constant values were also retrieved using the same method (shown in Section 5.2.1) as applied by the flight measurement. Starting from a given condition (dry soil in the first experiment, wet soil in the second), the terrain was moistened. In these experiments, surface dielectric constant was also estimated with the assumption to neglect soil roughness, and this would probably introduce some errors according to the not-perfectly-smooth surface under investigated. The two experiments were performed during the 2013 summer (a] 11st July and b] 16th July). The measurement setup is shown in Figure 5-14.

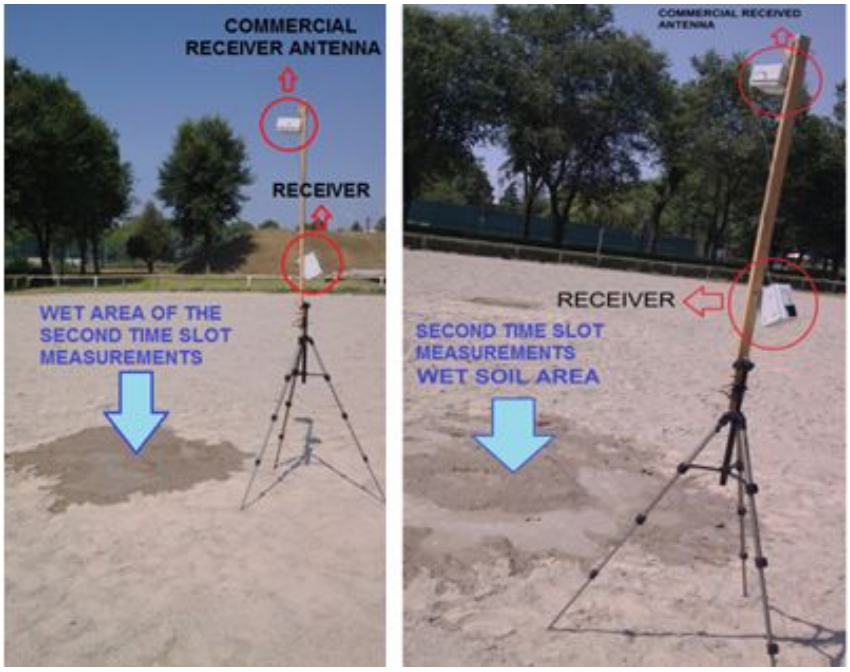

Figure 5-14 Experiment setup in static positions using the Hackberry board based receiver

5.2.3.2 Static measurement a]

During the a] experiment, three consecutive 40 s data acquisitions were performed. In the first time slot the terrain was almost dry, in the second time slot we started to moist it and in the third wet to soaking wet. Figure 5-15 shows the relative positions of specular reflection points for each GPS satellite in view and wet soil area (in blue region).

In Figure 5-15, the black circle is the LHCP receiving antenna footprint projected onto the ground. Green circles are the First Fresnel zone areas related to the first position of each specular reflection point. The wet area was between the points related to signals coming from GPS PRN 24 (black dots) and PRN 15 (green dots). The variation of the position of the specular points is shown with a sample time of 5 min, (the bold dot corresponds to the first specular point).

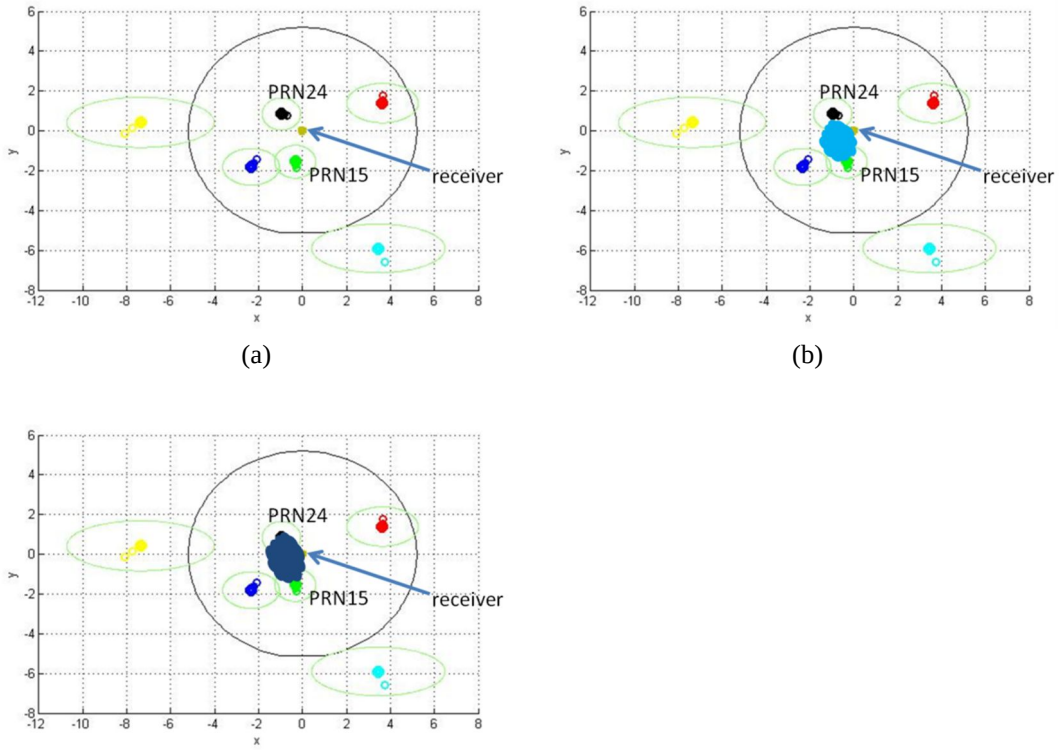

(a) (b)

(c)

Figure 5-15 Relative positions of specular points and wet soil area for the a] experiment. (a) First time slot: dry soil, (b) second time slot: wet soil, (c) third time slot: soaking wet soil.

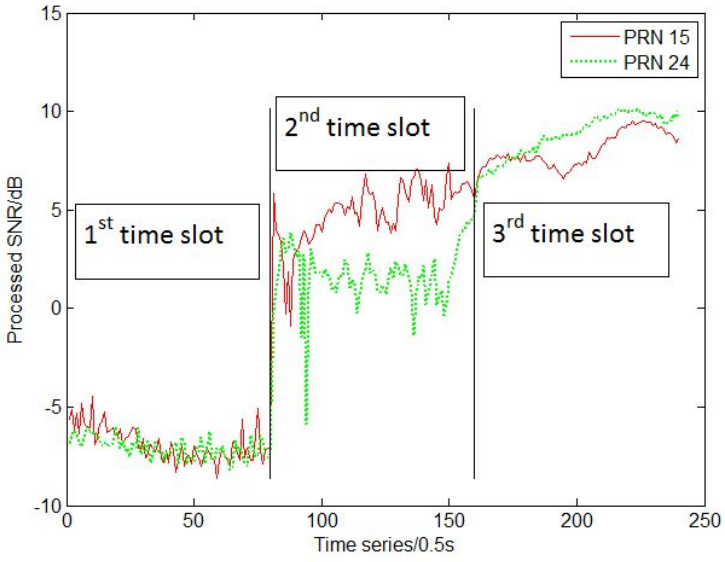

Figure 5-16 SNR time series of a] experiment, red line indicates signal from PRN 15 and green for PRN 24

Figure 5-16 shows the SNRs time series. Data from time intervals in which the soil conditions were changed are not shown. During dry soil condition, SNRs were

low for both signals, while they were increasing coherently with the terrain moistening. A good sensitivity of the receiver was reached, as it can be obtained from the data shown in Table 5-2. The statistics showed good complementarities of figures (in terms of mean values plus corresponding standard deviation) related to the three soil conditions. Changing from 'wet' to 'soaking wet' conditions, the area of interest was increased a lot. In the ‘wet’ case, the First Fresnel Zone related to the PRN 24 reflection was entering into the wet area (a mixture of dry/wet conditions was present). In the ‘soaking wet’ case, a bigger wet area was present in particular towards PRN 24 points (see Figure 5-15 for reference). This can explain the higher SNRs change estimated for the PRN 24, in comparison to the one characterizing the PRN 15.

Table 5-2 Statistics of observed SNR value (data are in dB) for the a] experiment

		DRY	**WET**	**SOAKING WET**
PRN15	median	-7.07	5.10	7.72
	mean	-6.87	4.91	8.05
	std	0.86	1.48	0.88
PRN24	median	-7.05	1.71	8.92
	mean	-7.06	1.72	8.82
	Std	0.53	1.50	1.08

The retrieved dielectric constant from averaged SNR in each time slot is presented in Figure 5-17.

Note here that in Figure 5-17, the obtained dielectric constant was retrieved directly from calculated SNR without the calibration as done in the flight measurement. Therefore, possible wrongly evaluated system parameters such as the receiver noise will influence the final accuracy of the results. However, as the aim of the static measurement is to verify the receiver sensitivity in terms of SNR, the retrieved dielectric constant is mainly used to check the dielectric constant variation caused by SNR sensitivity to different soil moisture, and also due to the reason that it was not well controlled and the in-situ measurement of soil moisture was missing, the results are shown as a reference and supplement. Anyway, the

changing trend of dielectric constant shown by Figure 5-17 is seen to be matched with the SNR behavior shown in Figure 5-16, except for the third time slot, where the dielectric constant difference between PRN 15 and 24 is much larger that the SNR difference. It is because that the relationship between dielectric constant and signal power expressed by Eq. 5-20 for the retrieval from LHCP reflected signals is not linear, which leads to an amplification of dielectric constant difference in higher SNR value region.

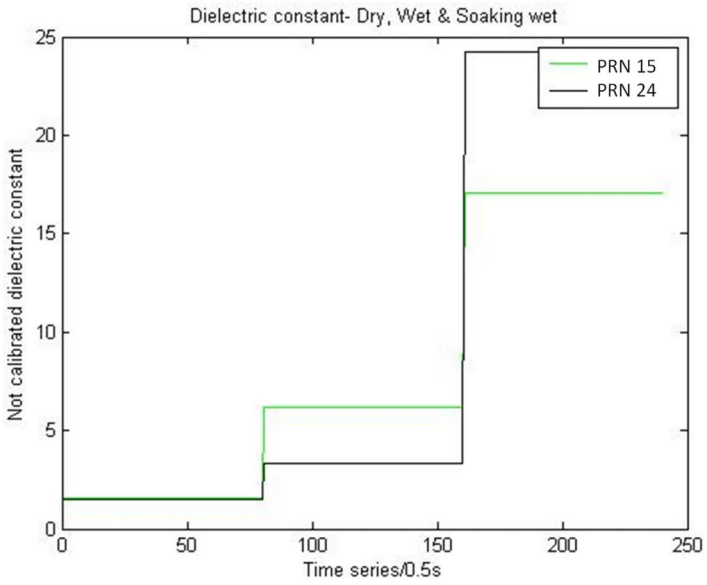

Figure 5-17 Retrieved dielectric constant from averaged SNR in each time slot

5.2.3.3 Static measurement b]

The b] experiment was very similar to the first one. But, in this case, the data acquisition was started with wet soil condition. In the second time slot, the wet area was increased moistening close to the boundary, and finally, in the third time slot, water was added into the overall area. Figure 5-18 shows the estimated specular point positions (in this case signals coming from the PRN 25, red dots and PRN 29, yellow dots, were analyzed).

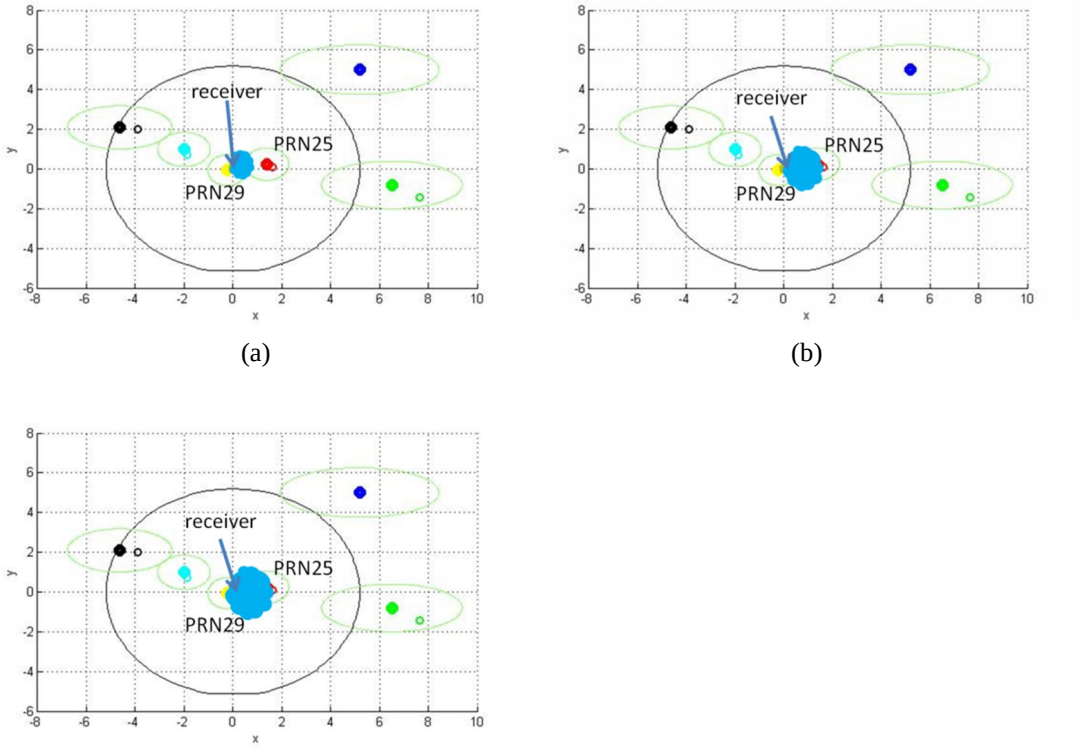

Figure 5-18 Relative positions of specular points and wet soil area for the b] experiment. (a) First time slot (b) second time slot (c) third time slot.

The corresponding SNRs time series are reported in Figure 5-19.In the first time slot, reflection points of satellite PRN 25 were on the boundary of the wet area, while the Fresnel zones of the satellite PRN 29 was falling in the completely wet area (see Figure 5-18). During the second time slot, the wet area was increased mostly toward PRN 25 reflection points maintaining the previous moisture level all over the other portion of the wet area (the SNR values associated to PRN 29 signal reflections were not significantly varied). This explains the strong increase of SNRs of more than 10 dB, a similar result was obtained during the a] experiment for the PRN 24 case. Finally, during the third time slot, more water was spilled in the overall area. In this case, an increase of SNR was found for the PRN 29 signal only. The statistics figures provided in Table 5-3 demonstrate again that both the reflected signal and the receiver seem to be enough sensitive to variations in the soil moisture.

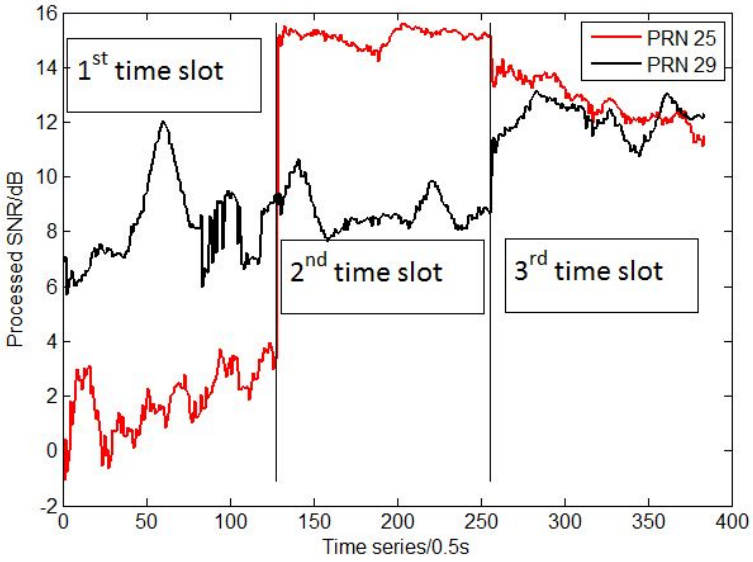

Figure 5-19 SNR time series of b] experiment, red line indicates signal from PRN 25 and black for PRN 29

Table 5-3 Statistics of observed SNR value (data are in dB) for the b] experiment

		DRY	WET	SOAKING WET
SV25	median	2.05	15.19	12.72
	mean	1.89	15.13	12.75
	std	1.10	0.27	0.76
SV29	median	8.12	8.57	12.21
	mean	8.26	8.76	12.14
	std	1.56	0.65	0.58

Similar with the a] experiment, dielectric constant was also retrieved and shown in Figure 5-20. Similar comments can be made to Figure 5-20 as done to Figure 5-17, dielectric constant generally reflects the change of SNR (for the same incident angle), but it is examined to be less sensitive to SNR change when SNR is lower and vice verse.

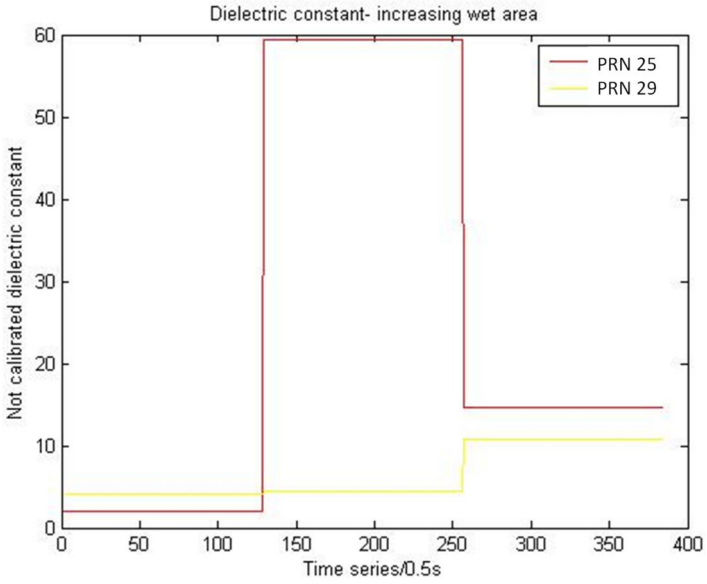

Figure 5-20 Retrieved dielectric constant from averaged SNR in each time slot

5.3 Dielectric constant retrieval through cross polarization ratio

One of the first studies about using cross polarization ratio for soil moisture remote sensing was carried out by [Zavorotny, 2000(a)], showing that the ratio of two orthogonal polarizations (*hh*/*vv* or *lh*/*rh*) does not depend on surface roughness and is sensitive to the soil moisture content.

A recent research done by [Egido, 2012] also applied both receptions of reflected LHCP and RHCP by a piece of agriculture field. The field was divided into two independently cultivated fields and the reflectivity of LHCP and RHCP from each field was averaged and recorded everyday during an entire crop growing season. As the two fields were worked and plowed in different ways for different crops, the roughness of these two fields was different during certain periods. The reflectivity for single LHCP or RHCP was examined to be dependent on soil roughness and sensitive to roughness changes, but the ratio of LHCP over RHCP reflectivity showed to be independent of surface roughness and sensitive with soil moisture changes.

Therefore, the study of cross polarization ratio draws our interest and it could utilize the same system structure as described in the previous static measurements,

except that an additional RHCP antenna plus one receiver is needed for receiving both reflected LHCP and RHCP signals simultaneously. The system configuration is shown in Figure 5-21.

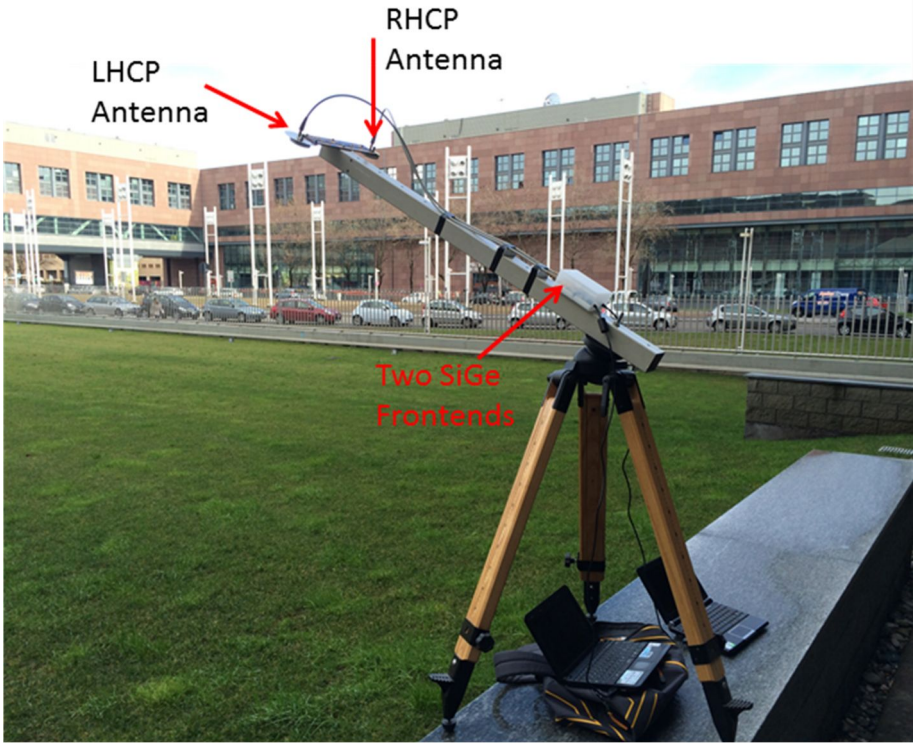

Figure 5-21 System setup for cross polarization of reflected LHCP and RHCP measurement

As shown in Figure 5-21, LHCP and RHCP antenna are fixed close to each other and pointing to the ground. Each antenna is connected with a SiGe frontend which is further connected to one PC. The data collection is done concurrently for LHCP and RHCP. Each piece of data (LHCP or RHCP) is post processed by the approach explained in Chapter 4 in order to get SNR time series. The remaining work is left to the derived dielectric constant retrieval algorithms shown in the following sections. However, due to the unpredictable problem of these two antennas, no available data were obtained by now, but the simulation results of retrieval algorithms are given in Section 5.3.4

5.3.1 Power and bistatic radar cross section

Radar cross section, as a scalar number, is a function of the polarization of the incident and received wave. A more complete description of the interaction of the incident wave and the target is given by the polarization scattering matrix (PSM),

which relates the scattered electric field vector $\mathbf{E}^s$ to the incident field vector $\mathbf{E}^i$. As $\mathbf{E}$ can be decomposed into two independent directions or polarizations, the polarization scattering matrix S is a 2 x 2 complex matrix [Knott, 2004]:

$$\begin{bmatrix} \mathbf{E}_1^s \\ \mathbf{E}_2^s \end{bmatrix} = \begin{bmatrix} S_{11} & S_{12} \\ S_{21} & S_{22} \end{bmatrix} \begin{bmatrix} \mathbf{E}_1^i \\ \mathbf{E}_2^i \end{bmatrix} \tag{5-22}$$

where $\mathbf{E}^s$ and $\mathbf{E}^i$ are the scattered and incident fields, each with independent vector components $\mathbf{E}_1$ and $\mathbf{E}_2$. The components of S are related to the square root of cross section [Knott, 2006]:

$$S_{ij} = \sqrt{\frac{\pm_{ij}}{4\pi R_2^2}} \tag{5-23}$$

where R_2 is the distance between the target (scattering point) and the receiver as a general definition in bistatic radar equations such as in Eq. 2-5, Eq. 2-6, and the scattering coefficient S is therefore a measurement of scattered field at the receiver with respect to its incident field right before scattering taking place. $\sqrt{\pm}$ is recognized as a complex number that can be described through a certain amplitude and a certain phase. In circular polarization, the electric field vector rotates in the plane perpendicular to propagation. Transmitted circular polarization can be defined in terms of horizontal and vertical polarizations, where circular polarization circulation view is from an observer located at the transmitter [Knott, 2004]:

$$\begin{bmatrix} \mathbf{E}_r^t \\ \mathbf{E}_l^t \end{bmatrix} = \frac{1}{\sqrt{2}} \begin{bmatrix} 1 & +j \\ 1 & -j \end{bmatrix} \begin{bmatrix} \mathbf{E}_h^t \\ \mathbf{E}_v^t \end{bmatrix} \tag{5-24}$$

where the superscript *t* denotes “transmitted”. The inverse transform for transmitted linear in terms of transmitted circular is obtained by taking the matrix inverse of Eq. 5-24:

$$\begin{bmatrix} \mathbf{E}_h^t \\ \mathbf{E}_v^t \end{bmatrix} = \frac{1}{\sqrt{2}} \begin{bmatrix} 1 & 1 \\ -j & +j \end{bmatrix} \begin{bmatrix} \mathbf{E}_r^t \\ \mathbf{E}_l^t \end{bmatrix} \tag{5-25}$$

Received polarization can also be defined in a similar way, except that the LHCP and RHCP definitions change because the viewer is now looking in the

direction of propagation, which is from the target toward the receiver and the radar system has defined LHCP and RHCP as looking away. Therefore, the similar expression as Eq. 5-5 and Eq. 5-6 in matrix is:

$$\begin{bmatrix} \mathbf{E}_r^r \\ \mathbf{E}_l^r \end{bmatrix} = \frac{1}{\sqrt{2}} \begin{bmatrix} 1 & -j \\ 1 & +j \end{bmatrix} \begin{bmatrix} \mathbf{E}_h^r \\ \mathbf{E}_v^r \end{bmatrix} \tag{5-26}$$

The circular polarization PSM contains no more information that the linear PSM. If one has computed or measured a linear PSM, the corresponding circular PSM can be obtained by using Eq. 5-24, Eq. 5-25 and Eq. 5-26 to get:

$$\begin{bmatrix} S_{ll} & S_{lr} \\ S_{rl} & S_{rr} \end{bmatrix} = \frac{1}{2} \begin{bmatrix} 1 & +j \\ 1 & -j \end{bmatrix} \begin{bmatrix} S_{hh} & S_{hv} \\ S_{vh} & S_{vv} \end{bmatrix} \begin{bmatrix} 1 & 1 \\ -j & +j \end{bmatrix} \tag{5-27}$$

Eq. 5-27 can be expanded into:

$$\begin{bmatrix} S_{ll} & S_{lr} \\ S_{rl} & S_{rr} \end{bmatrix} = \frac{1}{2} \begin{bmatrix} (S_{hh} - S_{vv}) - j(S_{vh} + S_{hv}) & (S_{hh} + S_{vv}) - j(S_{vh} - S_{hv}) \\ (S_{hh} + S_{vv}) + j(S_{vh} - S_{hv}) & (S_{hh} - S_{vv}) + j(S_{vh} + S_{hv}) \end{bmatrix} \tag{5-28}$$

The cross-polarized scattering coefficient $\pm_{qp}$ is zero by neglecting the multiple scattering and by considering only the first order of bistatic scattering coefficients. This assumption holds for the 3 models of KGO, KPO and SPM, for scattering in the specular direction (see Section 5.3.3 for detailed expressions) [Ulaby, 1982], [Ticconi, 2011]. These 3 models have been introduced in Chapter 2, and are used to derive the retrieval algorithms for different surface roughness conditions. Under this assumption and simplification, the condition $\pm_{hv} = \pm_{vh} = 0$ can be obtained, and by considering Eq. 5-23, Eq. 5-28 can be simplified as:

$$\begin{bmatrix} S_{ll} & S_{lr} \\ S_{rl} & S_{rr} \end{bmatrix} = \frac{1}{2} \begin{bmatrix} (S_{hh} - S_{vv}) & (S_{hh} + S_{vv}) \\ (S_{hh} + S_{vv}) & (S_{hh} - S_{vv}) \end{bmatrix} \tag{5-29}$$

Taking the two elements of *lr* and *rr* which are of our interest, and combining Eq. 5-23, the equations of radar cross section of circular polarization expressed by HP and VP radar cross sections are:

$$\sqrt{\pm_{lr}} = \frac{1}{2}(\sqrt{\pm_{hh}} + \sqrt{\pm_{vv}}) \tag{5-30}$$

$$\sqrt{\pm_{rr}} = \frac{1}{2}(\sqrt{\pm_{hh}} - \sqrt{\pm_{vv}}) \tag{5-31}$$

The remaining problem is to relate the power density of *lr* and *rr* which are our key outputs from post-processing to the radar cross sections of *hh* and *vv*, for the reason that these two radar cross sections have been extensively studied and modeled by several different scattering models such as KGO, KPO and SPM as mentioned in Chapter 2. Applying Eq. 5-22, for the LHCP and RHCP scattering the PSM is expressed:

$$\begin{bmatrix} \mathbf{E}_l^s \\ \mathbf{E}_r^s \end{bmatrix} = \begin{bmatrix} S_{ll} & S_{lr} \\ S_{rl} & S_{rr} \end{bmatrix} \begin{bmatrix} \mathbf{E}_l^i \\ \mathbf{E}_r^i \end{bmatrix} \tag{5-32}$$

In our specific GNSS-R case, incident LHCP electric field doesn't exist since the GPS satellites only transmit RHCP signals, which is:

$$\mathbf{E}_l^i = 0 \tag{5-33}$$

Therefore, the scattered fields of *lr* and *rr* are given by:

$$\mathbf{E}_{lr}^s = S_{lr}\mathbf{E}_r^i \tag{5-34}$$

$$\mathbf{E}_{rr}^s = S_{rr}\mathbf{E}_r^i \tag{5-35}$$

Recalling Eq. 5-11, which expressed the relationship of power density and electric field, and taking into account Eq. 5-34 and Eq. 5-35, scattered *lr* and *rr* power density has these expressions:

$$\sqrt{P_{lr}^s} = |S_{lr}|\sqrt{P_r^i} \tag{5-36}$$

$$\sqrt{P_{rr}^s} = |S_{rr}|\sqrt{P_r^i} \tag{5-37}$$

Note here that the scattered power P^s is the power density at the receiver point but before being received, incident power P^i is the power density at the scattering point. Therefore, power after being received by the receiver is:

$$P_{lr}^r = \frac{\text{a}^2 G^r}{4®} P_{lr}^s \tag{5-38}$$

$$P_{rr}^{r} = \frac{\lambda^2 G^r}{4\pi} P_{rr}^{s} \tag{5-39}$$

where λ is the wavelength and G^r is the receiver gain. The incident power is related to the transmitted power by:

$$P_r^i = \frac{G^t}{4\pi R_1^2} P_r^t \tag{5-40}$$

where G^t is the transmitter gain and R_1 is the distance between transmitter and scattering point. Connecting these equations shown in Eq. 5-36 to Eq. 5-40, the received *lr* and *rr* power with respect to transmitted power can be expressed by:

$$P_{lr}^{r} = \frac{G^t G^r \lambda^2 |\sigma_{lr}|}{(4\pi)^3 R_1^2 R_2^2} P_r^t \tag{5-41}$$

$$P_{rr}^{r} = \frac{G^t G^r \lambda^2 |\sigma_{rr}|}{(4\pi)^3 R_1^2 R_2^2} P_r^t \tag{5-42}$$

These two equations have similar form as the general bistatic radar equation shown by Eq. 2-4, except that the bistatic radar cross section σ is a complex number here and has to be made modulus. This similarity has proven the correctness of retrieval process up to this point. Now that the relationships of circular polarization radar cross section and radar cross section of *vv* and *hh* are given in Eq. 5-30 and Eq. 5-31, the square root of the ratio between P_{lr}^r and P_{rr}^r are made and expressed as:

$$\frac{\sqrt{P_{lr}^r}}{\sqrt{P_{rr}^r}} = \frac{\sqrt{P_{lr}^s}}{\sqrt{P_{rr}^s}} = \frac{|S_{lr}|}{|S_{rr}|} = \frac{\left|\sqrt{\sigma_{lr}}\right|}{\left|\sqrt{\sigma_{rr}}\right|} = \frac{\left|\sqrt{\sigma_{hh}} + \sqrt{\sigma_{vv}}\right|}{\left|\sqrt{\sigma_{hh}} - \sqrt{\sigma_{vv}}\right|} \tag{5-43}$$

Now, the link between the cross-polarization power ratio and radar cross section of *hh* and *vv* has been established. P_{lr}^r and P_{rr}^r are the power measurements that can be achieved from signal processing, σ_{hh} and σ_{vv} are radar cross sections of *hh* and *vv* which depend on dielectric constant, incident and scattered angles, surface roughness parameters in terms of statistical properties of surface height, and are given in different ways for different models and surface roughness

conditions. However, generally the surface roughness parameters are polarization independent and are unique for *hh* and *vv* polarization states [Zavorotny, 2000(a)], [Ulaby 1982]. The ratio shown in Eq. 5-43 can eliminate the surface roughness effect and leave only the effect of dielectric constant and scattering geometry, which makes this equation much easier to be solved and makes the cross polarization measurement roughness independent.

Another note to Eq. 5-43 is that P^s can represent the power scattered by a signal scatterer know as a facet and the corresponding $\pm$ is therefore the radar cross section of this scatterer. Or P^s can be defined as the total scattered power and in this case $\pm$ is seen as an average value over the entire illuminated area - the glistening zone. Thus, it's convenient to introduce the concept of the normalized radar cross section, which is defined as:

$$\pm_{qp}^{o} = \left\langle \frac{\pm_{qp(i)}}{\Delta A_i} \right\rangle \tag{5-44}$$

where $\pm_{qp}^{o}$ is the normalized or averaged radar cross section, $\pm_{qp(i)}$ is the radar scattering cross section of the *i*'th scatterer, and ΔA_i is the small scattering area associated with the reflecting facets of the *i*'th scatterer. The symbol $\langle\ \rangle$ represents the averaging process. Hence, the radar cross section can be given in the form of the product of normalized radar cross section and the illuminated area:

$$\pm_{qp} = \pm_{qp}^{o} A \tag{5-45}$$

where A is the total illuminated area, in another word, the glistening zone in GNSS-R geometry. Taking Eq. 5-45 into Eq. 5-43, we obtained this relation:

$$\frac{\sqrt{P_{lr}^r}}{\sqrt{P_{rr}^r}} = \frac{\left|\sqrt{\pm^{o}_{hh}} + \sqrt{\pm^{o}_{vv}}\right|}{\left|\sqrt{\pm^{o}_{hh}} - \sqrt{\pm^{o}_{vv}}\right|} \tag{5-46}$$

Up to here, the power ratio of cross polarization has linked to the normalized radar cross sections of *hh* and *vv*. The evaluation of $\pm^{o}$ is difficult since the scattering geometry changes by means of incident and scattering angles with different scatterers. However, the special case of $\pm_{qp(spec)}^{o}$ in the specular direction can be used to substitute the normalized $\pm_{qp}^{o}$ in Eq. 5-46 as a good approximation,

due to the reason that the specular point locates almost in the geometry center of the glistening zone. And $\pm^{o}_{qp(spec)}$ should be proportional to $\pm^{o}_{qp}$, the ratio operation made by Eq. 5-46 will cancel out the difference between $\pm^{o}_{qp(spec)}$ and $\pm^{o}_{qp}$ and remain unchanged by substituting $\pm^{o}_{qp}$ with $\pm^{o}_{qp(spec)}$.In this case, the scattering geometry shown by Figure 2-5 turns out to be: $^{-}_{i} = ^{-}_{s}$ and $^{\cdot\cdot}_{i} = ^{\cdot\cdot}_{s} = 0$. This assumption extremely simplifies the retrieval process for different scattering models which are shown in the following sections.

5.3.2 Retrieval process for specular reflection

Section 5.3.1 only deals with incoherent components caused by diffuse scattering, and the retrieval results have shown to be roughness independent. However, this cross polarization power ratio method can also be used to specular reflection case, even with the attenuation factor due to slight surface roughness, without the need to neglect the term of $\exp\left[-\left(4\pi\pm\cos^{-}/\lambda\right)^2\right]$, as what has been done in the retrieval process of a single LHCP shown in Section 5.2.1. The assumption of a perfectly smooth surface used in the retrieval in Section 5.2.1 is limited, since most of the time the surface height distribution doesn't satisfy the Rayleigh criterion as shown in Eq. 2-10, and it would cause errors for the retrieval of dielectric constant for a not "perfectly smooth" surface.

Similar with Eq. 5-19, the received power of *rr* polarization $P_{rr}^{\ r}$ can be obtained:

$$\sqrt{P_{rr}^{\ r}} = \frac{1}{2}\sqrt{\frac{P^t G^t}{4\pi(R_1+R_2)^2}\frac{G^r\lambda^2}{4\pi}}\sqrt{\exp\left[-\left(\frac{4\pi\pm\cos^{-}}{\lambda}\right)^2\right]}\left(\left|\Gamma_{hh}\right|-\left|\Gamma_{vv}\right|\right) \quad (5\text{-}47)$$

The term $\exp\left[-\left(4\pi\pm\cos^{-}/\lambda\right)^2\right]$ is identical with that in Eq. 5-19, since it's defined by Eq. 2-8 and is the same for both *hh* and *vv* polarization states. By making a ratio between Eq. 5-19 and Eq. 5-47, the cross polarization power ratio is directly linked to *hh* and *vv* Fresnel reflection coefficients:

$$\frac{\sqrt{P_{lr}^{\ r}}}{\sqrt{P_{rr}^{\ r}}} = \frac{\left(\left|\Gamma_{hh}\right|+\left|\Gamma_{vv}\right|\right)}{\left(\left|\Gamma_{hh}\right|-\left|\Gamma_{vv}\right|\right)} \quad (5\text{-}48)$$

where Γ is the Fresnel reflection coefficient given by Eq. 5-17 and Eq. 5-18. Similar to the solving of Eq. 5-10, dielectric constant can be solved through Eq.

5-48 as a real number. In order to separate the real and imaginary part of $£_r$, the [Hallikainen, 1985] model can be applied, and together with Eq. 5-4a, 5-4b and Eq. 5-21 the complex $£_r$ can be obtained for a certain known type of soil.

5.3.3 Retrieval process for diffuse scattering

In this section, three most used scattering models are studied and their expressions of radar cross sections are especially focused on. They are the Kirchhoff Approximation in stationary-phase approximation (Kirchhoff Geometrical Optics, KGO), Kirchhoff Approximation in Physical Optics Approximation (KPO) and Small Perturbation Method (SPM). These three models are representative since they cover different surface roughness conditions in a big range.

5.3.3.1 KGO

The validity limits of KGO model used for Gaussian surface is $k\pm > 2$, where k is the wave number and $\pm$ is the standard deviation of surface height, as has been defined in Section 2.3.1. Therefore, KGO is generally used for moderate to rough surfaces. The general reflected bistatic radar cross section for HP or VP is defined by [Ulaby, 1982]:

$$\pm_{qp}^{o} = \frac{\left(kq\left|U_{qp}\right|\right)^2}{2q_z^4\pm^2\left|°''(0)\right|}\exp\left[-\frac{q_x^2+q_y^2}{2q_z^2\pm^2\left|°''(0)\right|}\right] \tag{5-49}$$

where the only polarization sensitive parameter is U_{qp}, the other parameters are roughness parameters which can be canceled after taking Eq. 5-49 into Eq. 5-46:

$$\frac{\sqrt{P_{lr}^r}}{\sqrt{P_{rr}^r}} = \frac{\left\|U_{hh}\right|+\left|U_{vv}\right\|}{\left\|U_{hh}\right|-\left|U_{vv}\right\|} \tag{5-50}$$

Using the equations given in [Ulaby, 1982] for U_{qp} and setting the geometry parameters $¯_i = ¯_s$ and $¨_i = ¨_s = 0$ (see Figure 2-5), the U_{qp} for each polarization state is obtained:

$$\left|U_{hh}\right| = \left|2\cos¯ * \Gamma_{hh}\right| \tag{5-51}$$

$$\left|U_{vv}\right| = \left|2\cos¯ * \Gamma_{vv}\right| \tag{5-52}$$

$$\left|U_{hv}\right| = \left|U_{vh}\right| = 0 \tag{5-53}$$

where Γ is the Fresnel reflection coefficient with the same form as given in Eq. 5-17 and Eq. 5-18. Cross polarization terms U_{hv} and U_{vh} are 0, which indicates that $\pm^{o}_{hv}$ and $\pm^{o}_{vh}$ are 0 for KGO model in the specular direction. Using Eq. 5-51 and Eq. 5-52 to Eq. 5-50:

$$\frac{\sqrt{P_{lr}^{\ r}}}{\sqrt{P_{rr}^{\ r}}} = \frac{\left|\left|\Gamma_{hh}\right| + \left|\Gamma_{vv}\right|\right|}{\left|\left|\Gamma_{hh}\right| - \left|\Gamma_{vv}\right|\right|} \tag{5-54}$$

The similar result is gotten with the specular reflection condition shown by Eq. 5-48. The only difference between Eq. 5-54 and Eq. 5-48 is that in Eq. 5-48 the final ratio doesn't have a modulus operation. However, these two equations are equal since $\left|\Gamma_{hh}\right|$ is always greater than $\left|\Gamma_{vv}\right|$ for different grazing angles and different ε_r, as shown by the simulation in Figure 5-22.

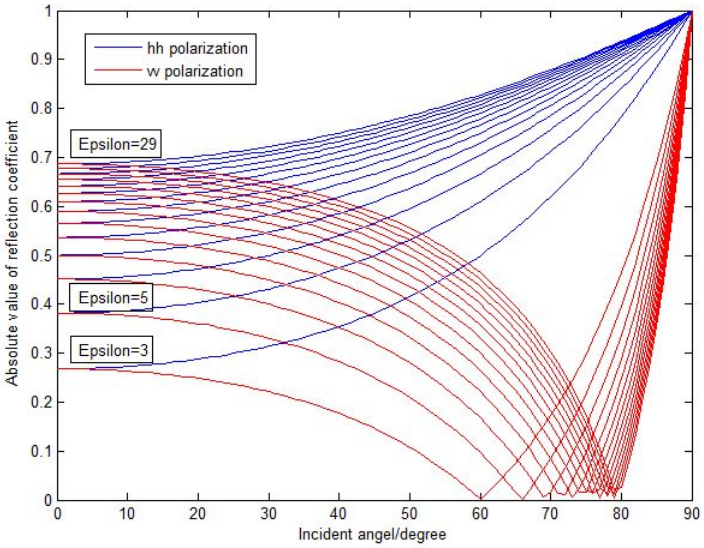

Figure 5-22 $\left|\Gamma_{hh}\right|$ and $\left|\Gamma_{vv}\right|$ in function of incident angle and dielectric constant

As shown in Figure 5-22, $\left|\Gamma_{hh}\right|$ always precedes $\left|\Gamma_{vv}\right|$ for any incident angle and any dielectric constant value. The dielectric constants ε_r used in the figure are real numbers for the simplification of the simulation ranging from 3 to 29 with interval of 2, and it can be seen as the modulus of the complex ε_r where the real part plays the dominant role. Another point that should be paid attention to is for

each ε_r, the *vv* polarization turns to be 0 at a certain incident angle, which is the so called Brewster Angle. Lower than this angle, $|\Gamma_{vv}|$ tends to decrease while $|\Gamma_{hh}|$ always grows with the increase of incident angle.

5.3.3.2 KPO

The validity limits of KPO model used for Gaussian surface is $k\sigma < 1$ and $m < 0.25$ (the rms of slope, see the definition in Section 2.3.1). This KPO model is therefore used for less rough surfaces. The incoherent part of bistatic radar cross section is [Ticconi, 2011]:

$$\sigma_{qp}^{o\ inc} = \left(|a_0| kl/2\right)^2 e^{-q_z^2\sigma^2} \sum_{n=1}^{\infty} \frac{\left(q_z^2\sigma^2\right)^n}{n!n} e^{-\frac{\left(q_x^2+q_y^2\right)l^2}{4n}} \tag{5-55}$$

The polarization-dependent coefficient a_i can be found in [Ulaby, 1982]. The expressions of the coefficient a_0 are reported below for the specular direction which are the key parameter in Eq. 5-55.

For *hh* polarization:

$$a_0 = -2\Gamma_{hh}(\theta_i)\cos\theta_i \tag{5-56}$$

For *vv* polarization:

$$a_0 = 2\Gamma_{vv}(\theta_i)\cos\theta_i \tag{5-57}$$

For *vh* and *hv* polarization:

$$a_0 = 0 \tag{5-58}$$

where θ_i is the incident angle, Γ is the Fresnel reflection coefficient given in Eq. 5-17 and Eq. 5-18. The coefficient a_0 is 0 for cross polarization of *hv* and *vh*, which again shows that σ_{hv}^o and σ_{vh}^o are 0 for KPO model in the specular direction. Taking Eq. 5-55, Eq. 5-56 and Eq. 5-57 into Eq. 5-46:

$$\frac{\sqrt{P_{lr}^r}}{\sqrt{P_{rr}^r}} = \frac{\left||\Gamma_{hh}| + |\Gamma_{vv}|\right|}{\left||\Gamma_{hh}| - |\Gamma_{vv}|\right|} \tag{5-59}$$

The same result comes out as given by Eq. 5-54.

5.3.3.3 SPM

The SPM is applied with a surface height standard deviation much less than the incident wavelength (5 percent or less) and an average surface slope comparable to or less than the surface standard deviation times the wave number. For a surface with Gaussian correlation function, such two conditions can be expressed analytically as [Ticconi, 2011]: $k\pm < 0.3$ and $\sqrt{2}\pm / l < 0.3$. Therefore, the SPM is used for slightly rough surfaces. The bistatic radar cross section is already given in Eq. 2-15, 2-16, 2-17 and 2-18. The only parameter that depends on polarization is $\sim_{qp}$ and the other surface roughness parameters are canceled out by taking Eq. 2-15, 2-16, 2-17 and 2-18 into Eq. 5-46:

$$\frac{\sqrt{P_{lr}{}^{r}}}{\sqrt{P_{rr}{}^{r}}} = \frac{\left\| \sim_{hh} \right| + \left| \sim_{vv} \right\|}{\left\| \sim_{hh} \right| - \left| \sim_{vv} \right\|} \tag{5-60}$$

where $\sim_{qp}$ for different polarization state can be calculated in specular direction considering the geometry parameters $\bar{}_i = \bar{}_s$ and $\ddot{}_i = \ddot{}_s = 0$ through expressions provided by [Ulaby, 1982]:

$$\sim_{hh} = \frac{-(£_r - 1)}{\left(\cos\bar{} + \sqrt{£_r - \sin^2\bar{}}\right)^2} \tag{5-61}$$

$$\sim_{vv} = \frac{(£_r - 1)\left(£_r - \sin^2\bar{} - £_r \sin^2\bar{}\right)}{\left(£_r \cos\bar{} + \sqrt{£_r - \sin^2\bar{}}\right)^2} \tag{5-62}$$

$$\sim_{hv} = \sim_{vh} = 0 \tag{5-63}$$

Combining Eq. 5-63 and Eq. 2-15, we have $\pm^{o}_{hv} = \pm^{o}_{vh} = 0$ for SPM in specular direction. Dielectric constant can be solved by putting Eq. 5-61 and Eq. 5-62 into Eq. 5-60.

5.3.4 Conclusions on cross polarization ratio retrieval

In Section 5.3, the retrieval of dielectric constant based on the power ratio of cross polarization is established for both specular reflection case and diffuse scattering case. Final expressions for these two cases are similar in the form of:

$$\frac{\sqrt{P_{lr}^{r}}}{\sqrt{P_{rr}^{r}}} = f(\theta, \varepsilon_r) \tag{5-63}$$

where f represents a function that is only dependent on incident angle θ and dielectric constant ε_r, the roughness effect is totally eliminated no matter what the form it is. The function f has the same expression for specular reflection, KGO model and KPO model given as Eq. 5-48, Eq. 5-54 and Eq. 5-59, whilst f is expressed differently for SPM.

In the retrieval, two most important approximations are used. The first is to use $\sigma^{o}_{qp(spec)}$ to substitute σ^{o}_{qp} in Eq. 5-46, which makes the whole retrieval simplified. Based on concerning only the scattering geometry in the specular direction, the cross polarization components of bistatic radar cross sections for all the three scattering models KGO, KPO and SPM are all calculated as 0: $\gamma_{hv} = \gamma_{vh} = 0$, which has proven the other approximation during the simplification from Eq. 5-28 to Eq. 5-29.

For the solving of the complex dielectric constant for the three scattering models, the same approach can be applied as has been used to the specular reflection case: addressing the empirical dielectric constant mode given by Eq. 5-4a and Eq. 5-4b described in Section 5.1 and choosing appropriately the soil composition parameters of S and C, the real and imaginary part of ε_r and also soil moisture m_v can all be solved. However, this is only one of the possible solutions, there are many widely used dielectric constant models and the only problem left is to choose a proper one that is fit for solving the equations.

Simulations of cross polarization power ratio in function of soil moisture content for SPM and other models are made and shown in Figure 5-23. The dielectric constant model of soil moisture applied the empirical model by [Hallikainen, 1985], and totally five different soil types are considered as listed in Table 5-1. For each soil type, 4 incident angles are simulated: 15°, 30°, 45° and 60°, and both results from SPM model and other models are plotted in the same figure, since the expressions of the power ratio of cross polarization for specular reflection and KGO / KPO scattering models are identical except for the one of SPM. As shown in Figure 5-23, for each soil type, the SPM results are overlapped with the results of the other models, which means that the retrieval algorithms applying SPM

model generate the same results with the other models and therefore, all the retrieval algorithms are uniformed no matter what the model is used and what the surface roughness is. This is an important conclusion which enables us to retrieve dielectric constant using the cross polarization method without considering the surface roughness and which model that should be used. All the retrieval algorithms have lead to a unique solution as shown by Eq. 5-59.

For a given soil moisture, the cross polarization power ratio increases with the decrease of incident angel. It has to be noticed that, the description is correct only when the incident angle is smaller than the Brewster Angle, here the minimum Brewster Angle is about 60°. With the same incident angle, ratio of *lr/rr* is shown to be sensitive with the soil moisture content, it has a changing range of about 6 dB to 7 dB from a dry soil (5% moisture content) to a wet soil (30% moisture content). These results are coherent with the results given by [Zavorotny, 2000(a)].

Finally, simulated results among different soil types don't differ much between each other except for (e). It's because that for the Silty Clay condition shown by (e), the sand percentage is much smaller than the other types of soil whilst its clay percentage is extremely high comparing with the others' and these two compositions strongly affect the dielectric constant value. Therefore, for a non-high-precision retrieval process, the only knowledge needed for the measured soil is whether it contains more clay or more sand. If the answer is clay, then apply the dielectric model for (e). For the other conditions, whatever the dielectric model is chosen among (a) to (d), the retrieval results tend to be similar without much difference.

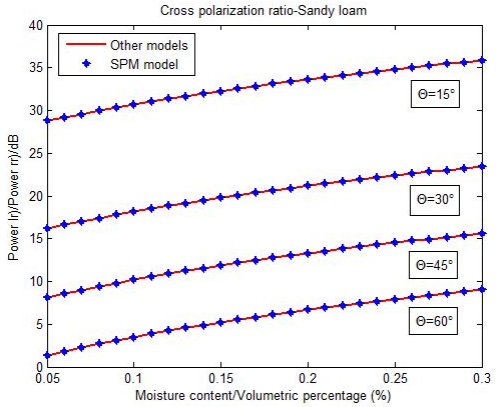

(a)

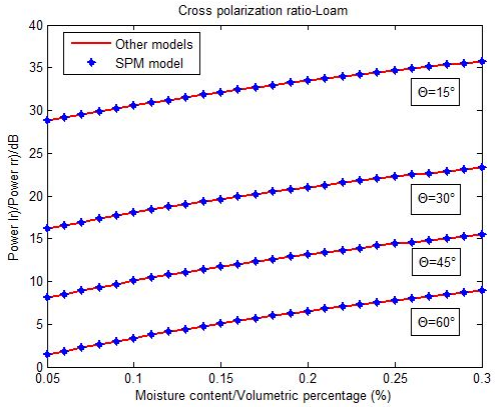

(b)

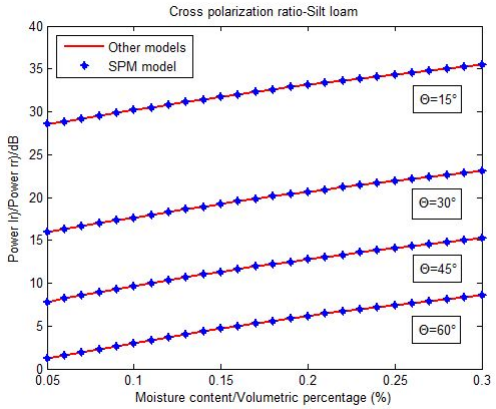

(c)

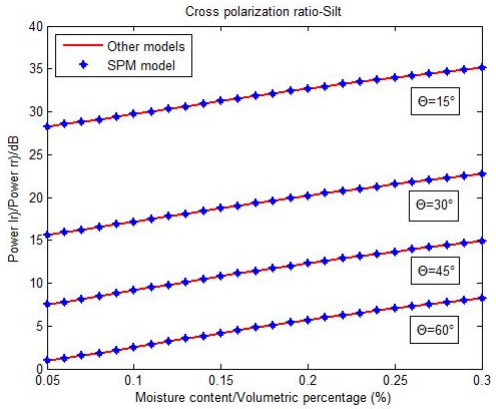

(d)

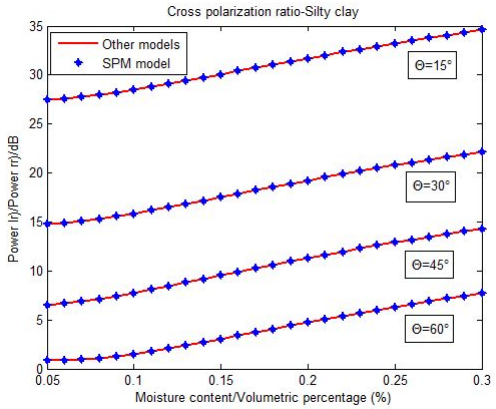

(e)

Figure 5-23 Sensitivities of power ratio of *lr/rr* to the soil moisture content for different types of soil: (a) Sandy Loam, (b) Loam, (c) Silt Loam, (d) Silt and (e) Silty Clay.

Chapter 6 Buried object detection and results

6.1 Theoretical background and introduction

As has been illustrated in Chapter 1, GNSS-R technique has been widely studied as a remote sensing method for various applications, such as soil moisture retrieval, snow depth detection, ice topography and depth monitoring, vegetation coverage and so on. A new application based on the possibility of detecting the presence of an object on the terrain or just under it, exploiting the penetration capabilities of electromagnetic energy within the soil, which are inversely proportional to the carrier frequency, is analyzed in this chapter. One current application is in the military field, in particular, to detect the presence of improvised explosive devices (IEDs) and pressure-activated mines. Mines and IEDs are often hidden on the terrain or inside the vegetation or are buried within the first few centimeters below the surface, since their devastating effects depend of course on their insertion depth.

L band signals (GNSS carrier frequencies are within this band) are not impacted by atmospheric attenuation and normally have a good penetration through vegetation [Wang, 1980]. At 1.5 GHz, the penetration depth varies from approximately 10 cm to 1 m for soil condition ranging from saturated to dry. In practice, the L band signal can interact with the first 10 cm, depending on the soil moisture level and incidence direction [Njoku, 1982], [Njoku, 1996]. In particular, in the case of almost dry soil, the penetration depth of active systems like GPS or a SAR was found to be around 10 cm [Larson, 2010] or 7 cm [Nolan, 2003] respectively. The penetration depth in function of wavelength for different soil moisture content given by [Njoku, 1996] is shown in Figure 6-1.

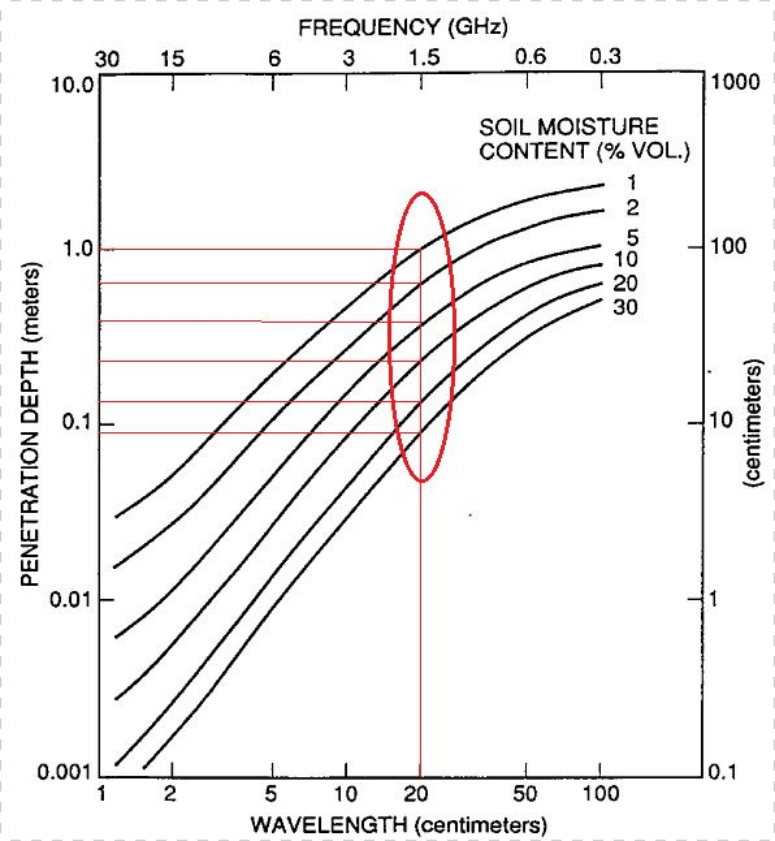

Figure 6-1 Penetration depth in function of wavelength for different soil moisture content [Njoku, 1996].

In Figure 6-1, the wavelength of 20 cm which is the GPS L1 wavelength is marked with a vertical line intersected with the penetration depths curves for different soil moisture content. According to Figure 6-1, for passive L band remote sensing, the penetration depth varies from 10 cm to 1 m depending on whether the soil is wet or dry. These values are upper-bound values that can be used when the soil is homogeneous, as in the case of the static measurements shown in Chapter 5 (dry or wet sand). With a non-uniform moisture profile, a 'soil moisture sensing depth' definition [Njoku, 1996] could be used and its approximation of one tenth of a wavelength in the medium would lead to less than 2 cm at 1.4 GHz. However, the penetration depth is strongly influenced by the soil density, soil moisture, and composition, and many models of soil can be considered and more realistic evaluation can be performed.

The dielectric properties of wet soil have been studied by several authors (e.g. [Wang, 1980], [Dobson, 1985]). These properties depend on water content and soil texture and on the carrier frequency of the signal used for monitoring purposes. The

high dielectric constant of water significantly increases both the real and imaginary parts of the soil's dielectric constant as the water volumetric concentration increases. The dependence on soil type (or 'texture') is due to the different percentages of water bound to the surface of the different particles characterizing the soil. Bound water particles exhibit less freely molecular rotation at microwave frequencies and hence are characterized by smaller dielectric effects than the free water in the pore spaces. This is most evident in clay soils, which have greater particle surface areas and affinities for binding water molecules and hence are capable of holding greater percentages of bound water. The dependence of dielectric constant for a sandy soil on the signal carrier frequency is reported in [Njoku, 1977] (see Figure 6-2). The real part is almost constant below 5 GHz, while the imaginary part is strongly frequency dependent. As reported in [Njoku, 1996], this frequency dependence can be taken into account considering the penetration depth which depends on the moisture volumetric concentration and on the wavelength. At the L1 carrier frequency of the GPS signal (1,575.42 MHz), penetration depths decrease from 1 m to 10 cm, from dry soil to 30% water concentration. The penetration depth also depends on the elevation angle of the incident microwave. Since the nadir incidence is the best case, in our experiments, the antenna boresight was aligned very close to the nadir direction (approximately 5° off the nadir).

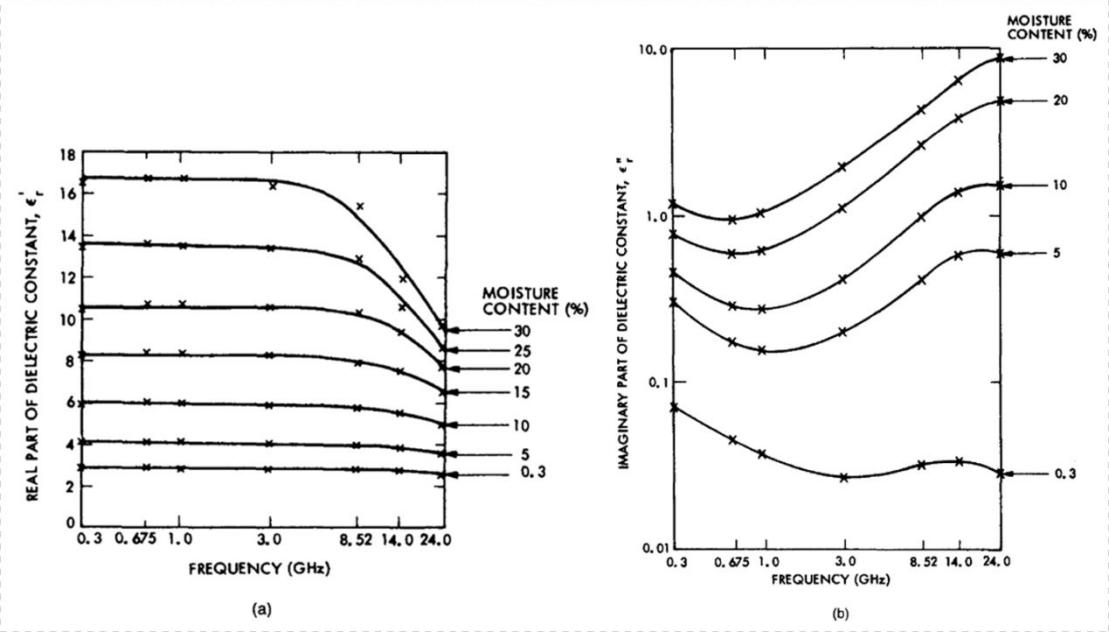

Figure 6-2 Dielectric constant behavior (real and imaginary part) in function of frequency for different moisture contents [Njoku, 1977].

For the detection of mines that are hidden in the superficial layer of the ground (explosive devices are hidden in the first few cm below the surface in order to make their devastating effects as effective as possible), this penetration capability is enough. Generally, complicated and expensive devices are used to detect explosive objects [Perrin, 2004], [Frezza, 2007]; most of them work very well, but they need the human presence on the field to move the detector.

In this research, the capability of GNSS-R signals to detect buried metallic objects is investigated through the use of the Hackberry board based receiver. This receiver is relatively light and can be mounted on board a remotely controlled unmanned aerial vehicle (UAV), thus avoiding the human presence in the field. The second measurement campaign involved in the determination of object dimension applied the PC based receiver. Either receiver was connected to a LHCP antenna to collect signals reflected from the ground. Surface roughness was not taken into account and the reflected signal power was estimated considering only coherent power. The open-loop approach was used for deriving SNR time series related to the reflected GPS signals as been explained in Chapter 4.

A couple of measurement campaigns were carried out with and without a metal object (a metal plate). The first measurement campaign described in this work was performed in static conditions on sandy terrain to check the functionality of the system and the sensitivity to the presence of the metal obstacle. In the second measurement campaign, the antenna moved along a given path, mimicking a flight.

6.2 Buried object detection measurements

In this section, the results of two experiments performed during the 2013 summer season are discussed:

A. Piazza d'Armi, Turin, Italy, 16 July, 2013, antenna in a static position, Hackberry board based receiver, sandy terrain.

B. Montoro, Avellino, Italy, 22 August, 2013, moving antenna, PC-based receiver, grass terrain.

Both the experiments were carried out considering as a target a circular metal disk (28-cm diameter) object. The dimensions of this object are comparable to those of an improvised explosive device or a pressure-activable mine.

Every measurement was carefully planned using the georeferencing program described in Chapter 4. The antenna used was the commercial antenna shown in Figure 3-14. It is an active L1/L2 RH/LH antenna (PN 4261215), characterized by a HPBW of 114° (maximum gain 3.5 dB). In the static measurement, the antenna was fixed on a plastic-wood structure in order to perform the measurements at a constant height (3 m) from the ground and in far field conditions.

6.2.1 Piazza d'Armi experiment

This experiment was performed in order to evaluate the sensitivity of the system to the presence of a metal object above or just under a dry or a completely wet sandy terrain (the metal plate was buried 5 to 10 cm under the surface). The Hackberry board based receiver was used. The antenna was mounted at 3 m height from the ground on top of a wooden rod fixed to a static tripod. The antenna beam axis was moved 5° away from the nadir position in order to avoid interference with the tripod structure and with the receiver itself, which was fixed to the same wooden rod (see Figure 6-3).

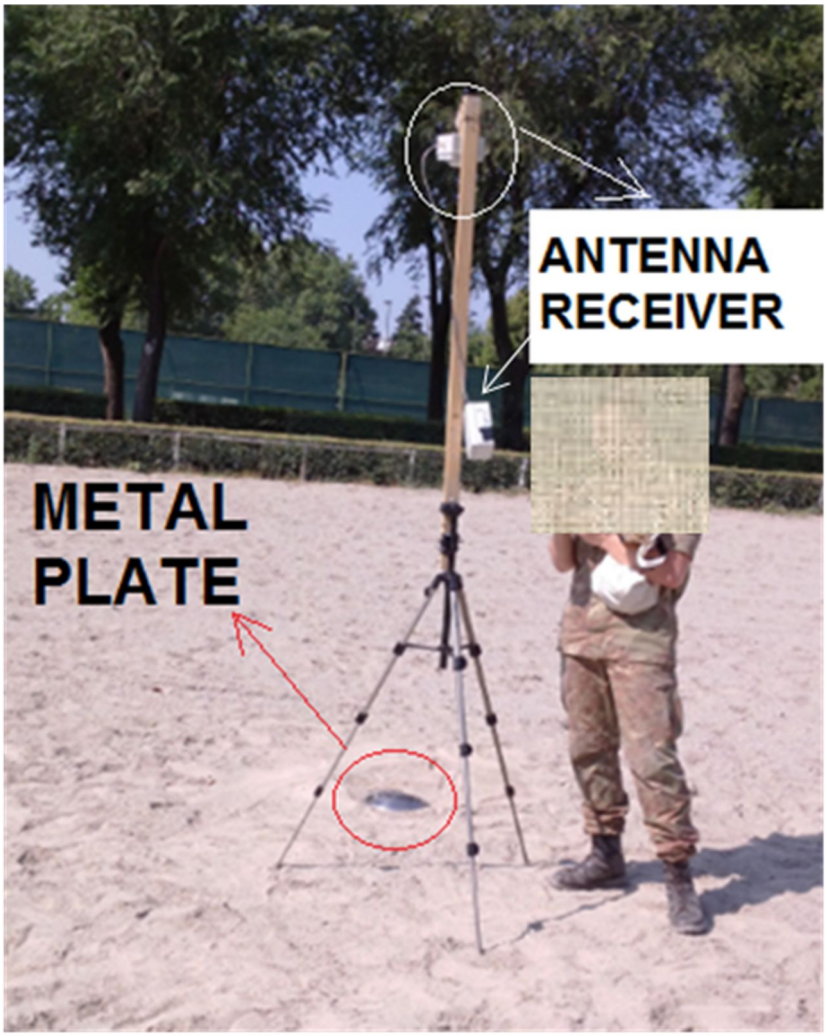

Figure 6-3 Experiment A: Static measurement setup. Tripod and wood-rod support for the receiver and the antenna.

The experiment geometry was carefully designed considering the prediction of the specular reflection point positions (see Figure 6-4). The positions of each specular reflection point were plotted in the *x-y* plane map with a sample time of 5 min for an overall experiment length of 50 min, are shown for each reflected signal (coming from different GPS satellites). Blue ellipses depict the first Fresnel zone boundaries evaluated from geometry for the first specular point of each series (identified by the bold colored specular reflection point). The antenna footprint is defined by the black line. The plot shows distances in meters, considering the receiving antenna (pink dot) in the origin of the reference system.

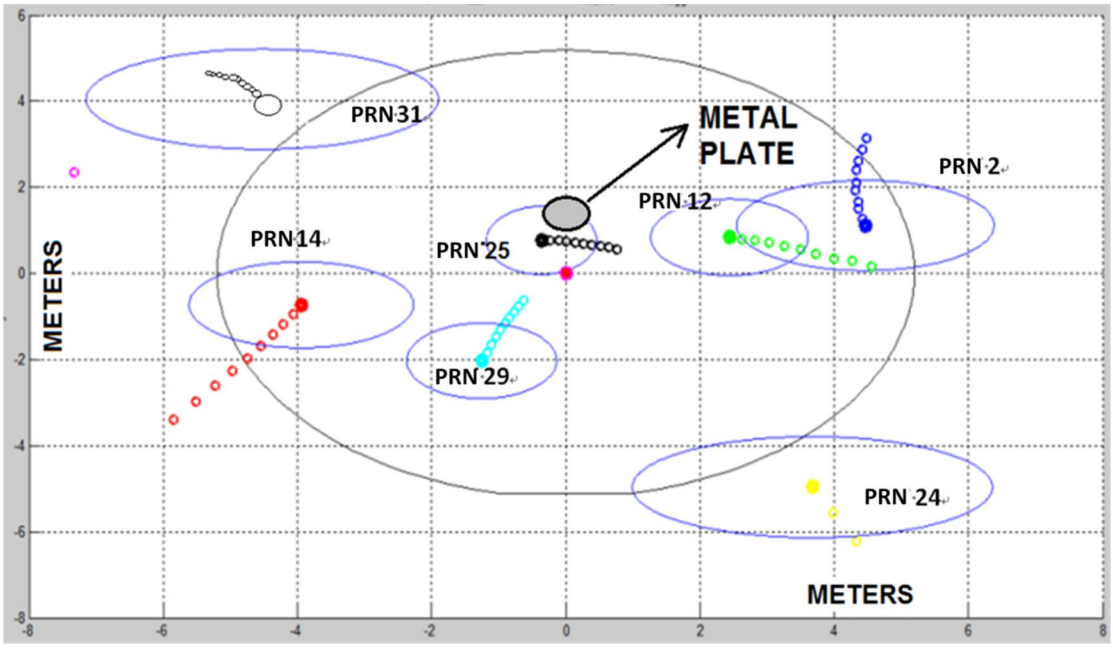

Figure 6-4 Experiment A: Prediction of reflection points on a *x*-*y* plane

The Google Maps is shown in Figure 6-5, while the estimated positions of the specular points are shown in Figure 6-4. The sample time of each point in Figure 6-4 was 5 min, and 10 positions for each specular reflection point were plotted, based on predicted orbits.

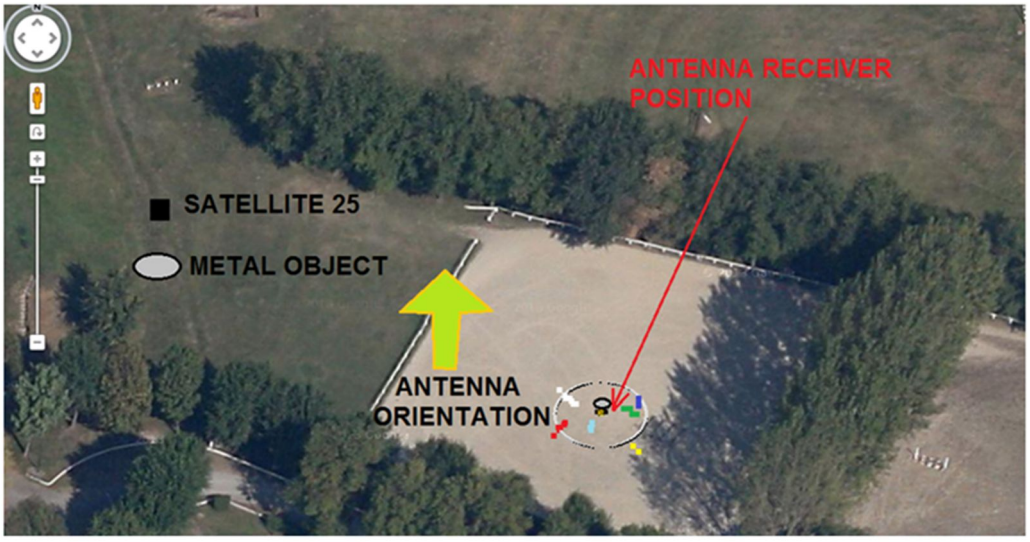

Figure 6-5 Experiment A: Prediction of reflection points on Google Maps

We started the simulation at 2:40 p.m., and we ended the prediction after 50 min (10 different specular reflection points are therefore shown). The experiment started at 2:55 p.m. and lasted 20 min. This means that the predicted reflection

point positions during the experiment are from the third to the eighth point (the Fresnel zones should be shifted). Five continuous 40-s raw data time series were taken, and the configuration of the target and of the surrounding terrain was changed (leaving the metal plate always in the same position with respect to the antenna's boresight). In particular, the following five time slots were considered:

A1 - from 2:55 to 2:56 p.m. (local time), the metallic plate was placed on dry soil far away from the expected first Fresnel zone.

A2 - from 3:00 to 3:01 p.m., the metallic plate was removed from the antenna footprint.

A3 - from 3:09 to 3:10 p.m., the metallic plate was buried under the dry soil.

A4 - from 3:12 to 3:13 p.m., the metallic plate was placed on dry soil.

A5 - from 3:14 to 3:15 p.m., the metallic plate was buried under completely wet soil.

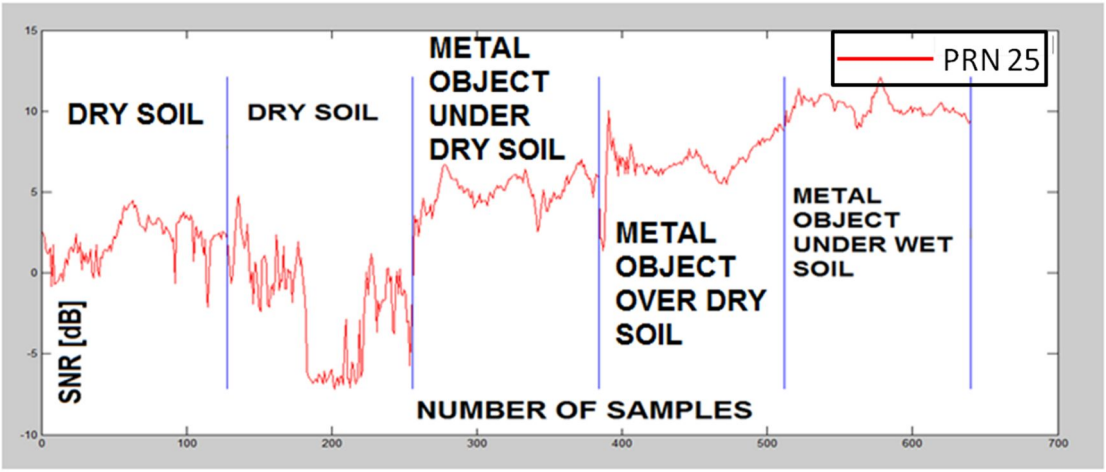

Figure 6-6 Experiment A: SNR time series for PRN 25

The five SNR time series coming from GPS PRN 25 (the satellite interacting with the metal plate, as shown in Figure 6-6) were connected, and the overall trace is shown in Figure 6-6. For each time series, some statistical indicators are summarized in Table 6-1. The first two measurements (A1 and A2) were performed to verify the correct operation of the software receiver in terms of data acquisition. In the first one (A1), the metal plate was not inside the first Fresnel zone, but it was in the antenna footprint. Therefore, the SNR estimate of +2 dB (mean value) also takes into account some of the power scattered out from the specular direction by the metal plate. During the second time slot (A2), the object was removed, but an

unexpected event occurred in the receiver hardware around the 200th sample. In this case, a more realistic statistical figure for the estimated SNR would be around −1 dB (also the std figure shown in Table 6-1 is not representative). The presence of the metallic plate over dry soil (A4) or just buried under it (A5) produces a significant increase in the received power (from around −1 dB without any object to 5 or 7 dB). This increase in the SNR should be produced by the metallic object only, since the ground in the (coherent) Fresnel zone (and in the noncoherent - glistening - zone) did not change. In conclusion, in the case of dry terrain, where the penetration depth allows more electromagnetic energy to reach the metal plate and to be reflected back towards the receiver, a good sensitivity of the receiver was observed. In fact, a level of 5.1 ± 1 dB was measured when the metal plate was buried under the sand, while there was a stronger 6.9 ± 1.3 dB when it was simply placed above the sand.

Table 6-1 Statistical characterization of the SNR estimates of Experiment A

		A1 - metal object on dry sand not in the Fresnel zone	A2 - dry sand	A3 - metal object under dry sand	A4 - metal object over dry sand	A5 - metal object under wet sand
PRN 25	Median	2	−1	5	6	10
	Mean	2	−2	5	6	10
	Std	1	3	0	1	0

A noticeable increase of a further 5 dB was observed in the case of completely wet sand (A5). This higher contribution to the received power is probably due to the increase of the dielectric constant of the terrain due to the presence of water. Several experiments were done before (but not reported here), but in all of them, the increase of the real part of the dielectric constant due to the water content strongly impacts the detection capability of the receiver.

6.2.2 Montoro experiment

Since the received signal was proved to be sensitive for buried object detection, in this second experiment, the evaluation of the dimension of the metal plate was investigated by setting up a moving experiment. A kind of unmanned aircraft System (UAS), flying 2.5 m over a 6- m strip of terrain, was simulated as shown in Figure 6-7.

Figure 6-7 Moving measurement setup for experiment B

Two plastic boxes forming the receiver support were joined together and fixed to two pulleys between two trees on the terrain. A cable allowed the receiver support to be moved along a rectilinear path. In this second experiment, the PC-based configuration was used. The prediction of the reflection points for this experiment is shown in Figure 6-8.

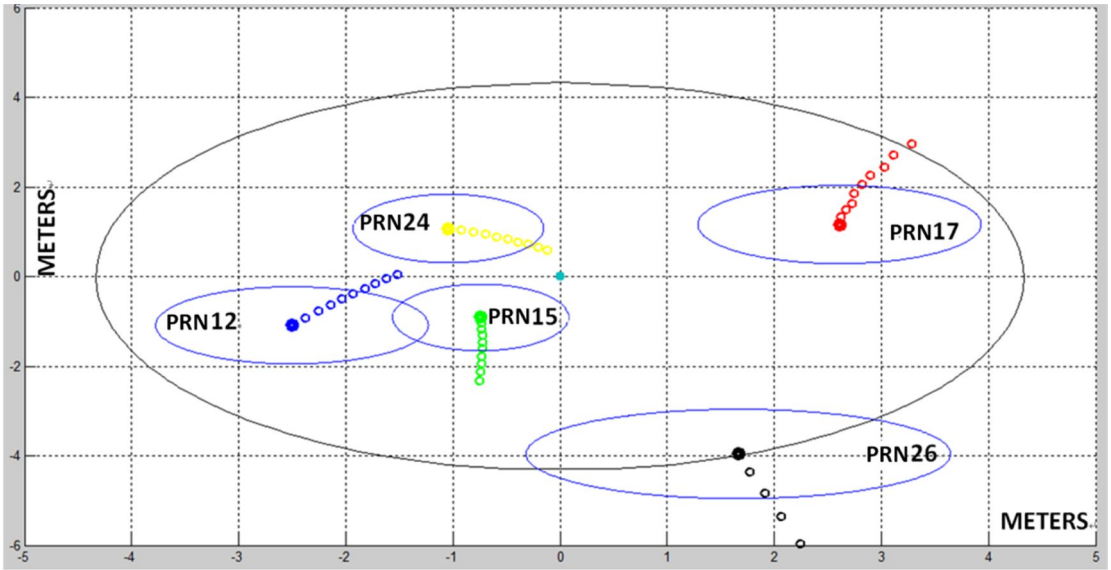

Figure 6-8 Experiment B: Prediction of reflection points on *x*-*y* plane.

The metal plate was positioned 5 m away from the starting point (1 m away from the ending point) on a portion of ground on which a contribution to the reflection of the signal coming from PRN 24 was expected. In this case, the effects due to vegetation canopy and grass coverage should be taken into account. The estimation of the quantitative impact is very difficult, being a combination of incident angle, wavelength, biomass volume, height, and loss component induced by the dielectric constant of water-containing stalks and leaves. In addition to the theoretical approach described by [Ulaby, 1982], [Ulaby, 1985], a detailed analysis is presented in [Ferrazzoli, 2010], [Egido, 2012]. As a first approximation, an average reduction of the SNR of 2 dB due to the effect of vegetation will be taken into account.

Three ‘flights’ were performed:

B1 - from 8:50 to 8:51 a.m., without the 28-cm-diameter metal plate.

B2 - from 8:52 to 8:53 a.m., with the metal plate placed on the soil.

B3 - from 8:54 to 8:55 a.m., with the metal plate buried approximately 4 cm under the soil.

As expected, a strong ‘dynamic’ on the SNR time series (approximately 8 dB in this case, from −6 dB to around 2 dB) was estimated when reflections occurred with or without the metallic plate, for the signal corresponding to PRN 24 shown in Figure 6-9

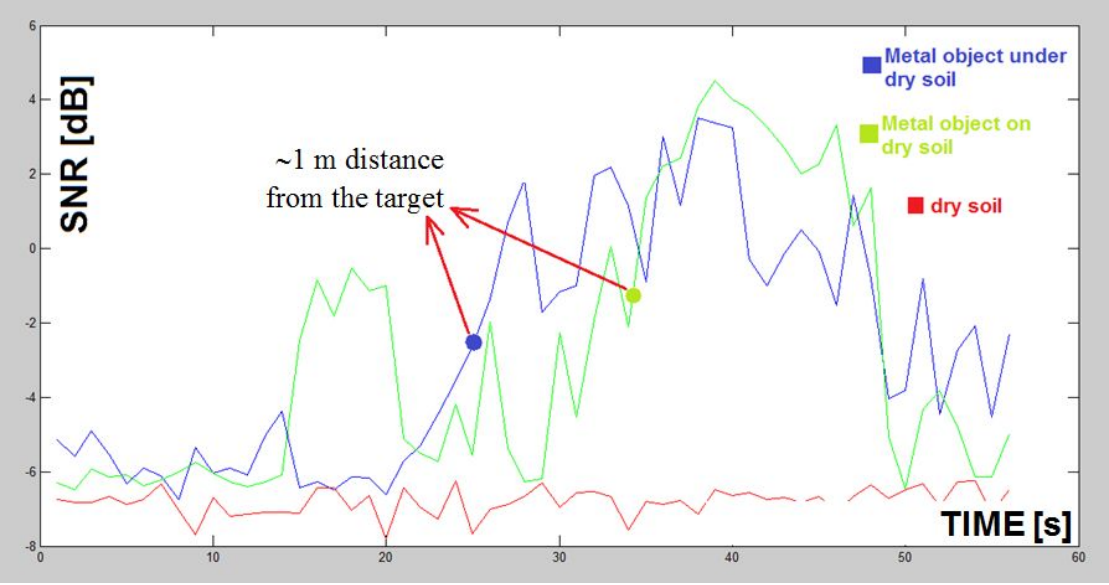

Figure 6-9 Experiment B: Time series of SNR.

In Figure 6-9, the red plot is the time series evaluated without any object (during the first flight), while the green and the blue lines represent the results obtained when the metal plate was placed above and under the terrain (second and third flight). A difference of approximately 2 dB between these two cases was estimated. This result is coherent with the SNR difference experienced in the first experiment when the metal plate was moved from the ground below it. The approximately 5-dB increase observed around the 20th sample in the SNR, estimated when the object was placed on the soil (green line), was unexpected. Since the receiver was manually moved, this signal could be related to some strong oscillation caused by the payload 'pulling.' Another important aspect to be taken into account is that the signal due to the presence of the metallic plate was expected to rise between 30 and 40 s. In fact, a mean velocity of 10 cm/scan was estimated (the entire 6-m track was completed in approximately 57 s for all the experiments), and the object placed at approximately 5 m from the starting point and the first Fresnel zone dimension was approximately equal to 1.5 m, as shown in Figure 6-8. The times when the signal started to rise are identified with the green and blue points in the time series shown in Figure 6-9. They were computed considering the time when the signal increased by 3 dB from the background value. The rising time of 35 s is quite correct for the experiment performed with the metal plate over the soil (green line). For the other case (blue line), the payload velocity during the first half of the experiment was probably greater than that during the second part. Also in this second example, an approximately 2-dB difference in the maximum signal available after reflection from the metal plate placed over (green line) or buried in (blue line) the soil was detected.

Thanks to this experiment, an estimate of the dimension of the metal plate was also possible. Since the SNR is related to the energy coherently reflected by the presence of a metal object inside a moving first Fresnel zone, the corresponding time series must be related to the spatial convolution between the Fresnel Zone and the area of the target. In fact, as expected, a trapezoid-shaped SNR time series was observed. As the metal plate was smaller than the dimension of the first Fresnel zone, it is clear that the overall rising time is related to the object dimension (the diameter of the metal plate). This rising time can be empirically evaluated considering the time the SNR needs to increase from a minimum of +3 dB to a

maximum of −3 dB.

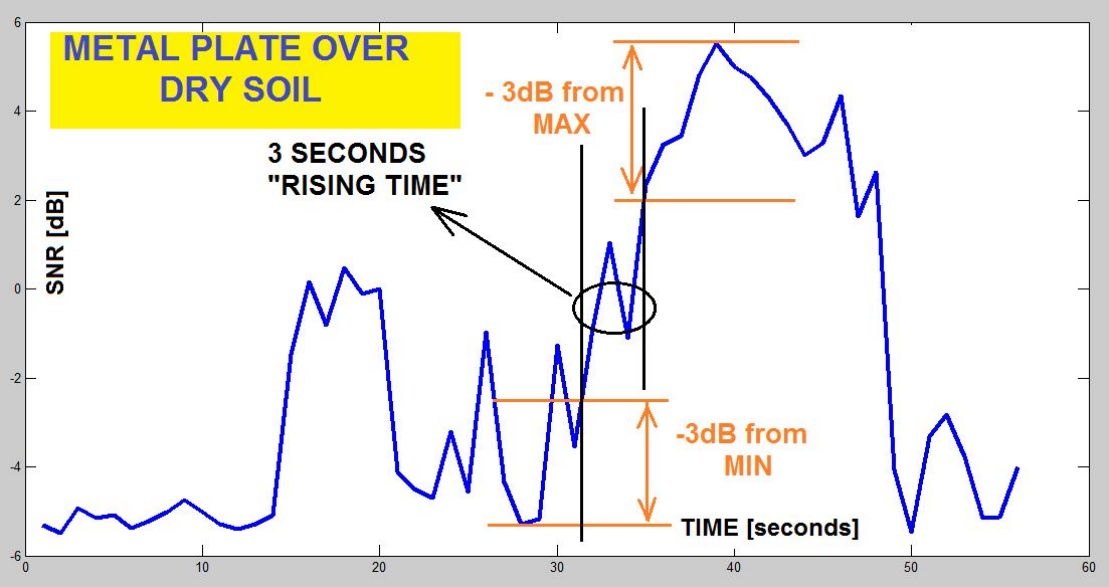

Figure 6-10 Experiment B: SNR time series evaluated for the object on the soil (green line in Figure 6-9).

In Figure 6-10, this concept is highlighted on the time series evaluated for the object over the soil (green line in Figure 6-9), for which a rising time of approximately 3 s can be identified. Considering an average payload speed of 0.1 m/s, the dimension of the target can be estimated to be approximately 30 cm which is close to the diameter of the metal plate.

6.2.3 Conclusion

In this chapter, a new application of GNSS-R technique for the detection of buried objects was investigated. An LHCP antenna was used to collect reflected GPS signals by a software-defined radio GPS receiver. The effects of surface roughness and vegetation canopy were neglected and the reflected signal power estimated considering only coherent power.

Two measurement campaigns were carried out and the variation of the SNR level due to the presence of a metallic object was investigated. The first measurement campaign was performed in a static condition on a sandy terrain to check the functionality of the system. Note that the presence of the metallic object was detected also in the case of wet terrain. In this case, the effect due to the increase of the dielectric constant characterizing the ground may hide the effect

derived from the metallic object. In the second measurement campaign, the antenna was moving along a given path and the possibility of detecting the object dimensions was highlighted. The results show the possibility of adopting this technique on board an UAV, remotely controlled. In this case, the flying direction could be modified in order to better understand the position and shape of the object.

Chapter 7 Snow depth measurements

7.1 Description

In the spring of 2013, snow depth measurement was done trying to figure out the relation between SNR and snow depth. The meadow in front of the GM building was covered by different depths of snow during February 20th to February 22nd. We made five periods of measurements in those three days to analyze the signals reflected from the meadow covered by snow.

Figure 7-1 Measurement setup on the roof top

Figure 7-1 shows the setup used for the snow measurement on the roof. The commercial antenna is fixed on the front of the signal receiving equipment with the elevation of 45° while the box is the compact Hackberry based receiver. The meteorological parameters corresponding to the five measurement periods are significant and are shown in Table 7-1.

Table 7-1 Meteorological information of the experiment periods

Day	Time	Weather	Snow Level	Humidity
Feb 20th	16:35—17:05	Foggy	null	70%
Feb 21st	13:35—14:15	Snow	1cm	93%
Feb 22nd	09:55—11:05	Snow	2cm	97%
Feb 22nd	11:55—12:35	Snow	3cm	87%
Feb 22nd	16:05—17:05	Snow	0.5cm	78%

7.2 Results and Data Analysis

The SNR time series for each single measurement is shown in Figure 7-2 to Figure 7-6. Due to the use of the compact receiver, data were not recorded continuously but with a 40 s of recording time for each piece. Around 80 s of time interval between two pieces was expected for the writing of data from ram to SD card. Occasionally some piece was lost, but all the pieces were arranged at the time when they were received.

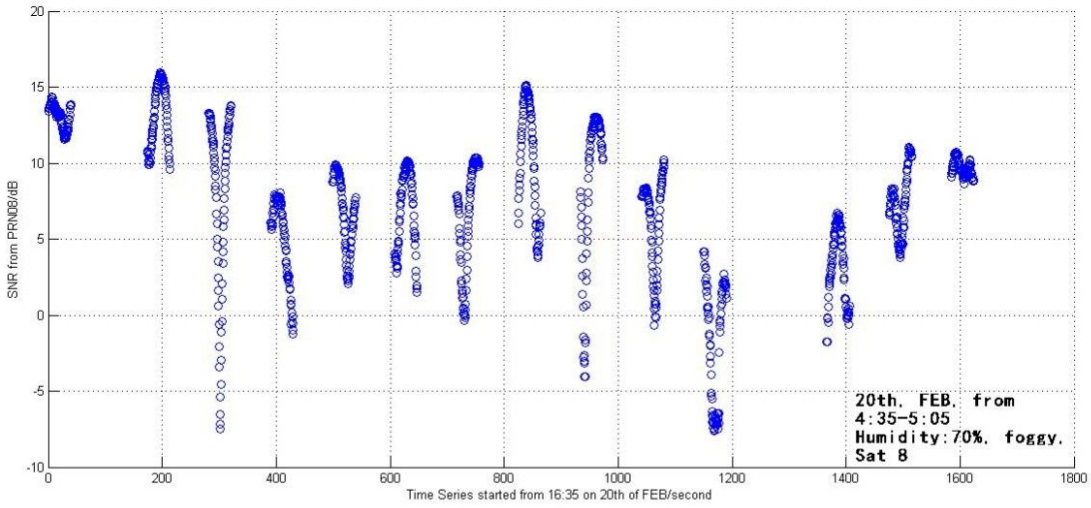

Figure 7-2 SNR of the measurement on 20th Feb, from 16:35-17:05

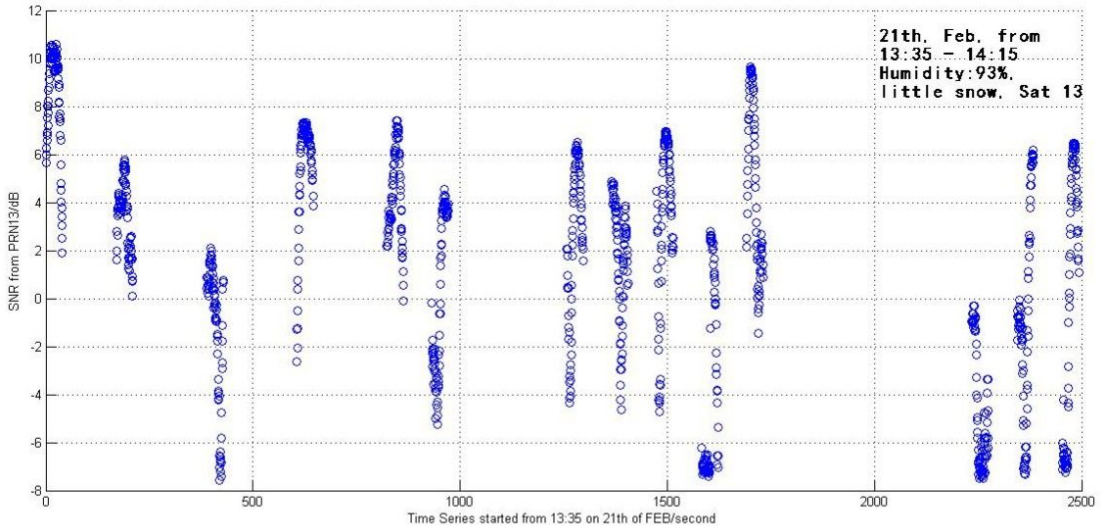

Figure 7-3 SNR of the measurement on 21st Feb, from 13:35 – 14:15

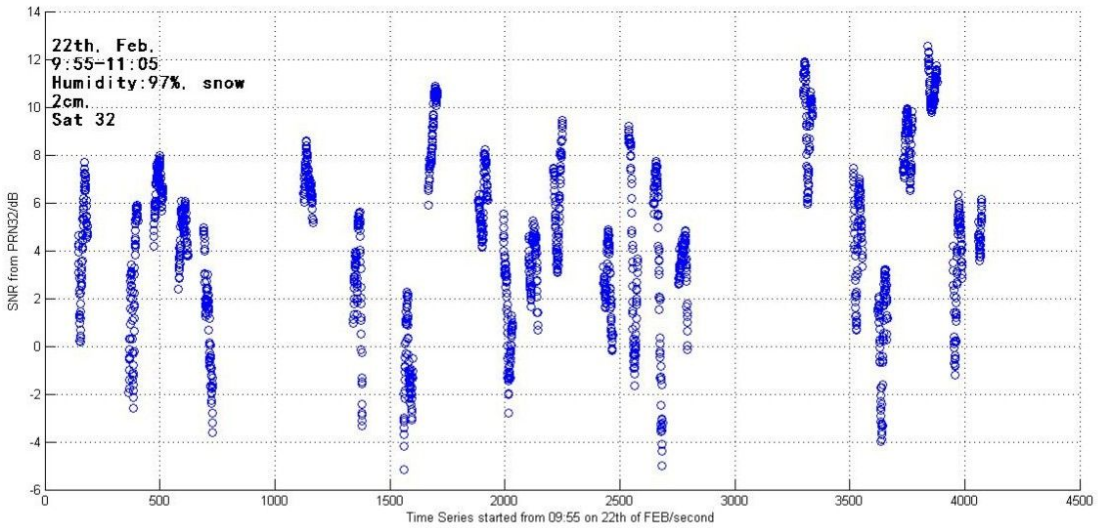

Figure 7-4 SNR of the measurement on 22nd Feb, from 9:55- 11:05

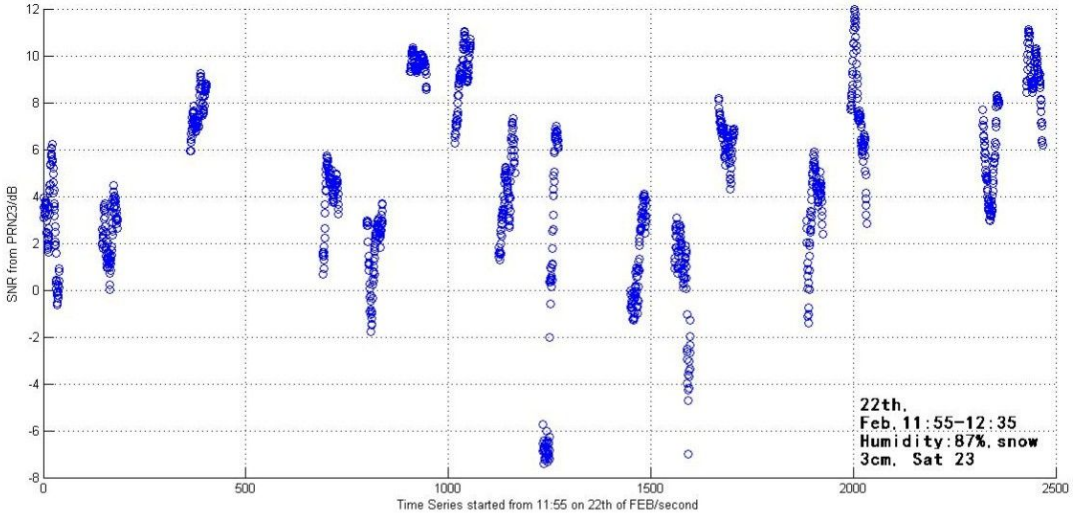

Figure 7-5 SNR of the measurement on 22nd Feb, from 11:55-12:35

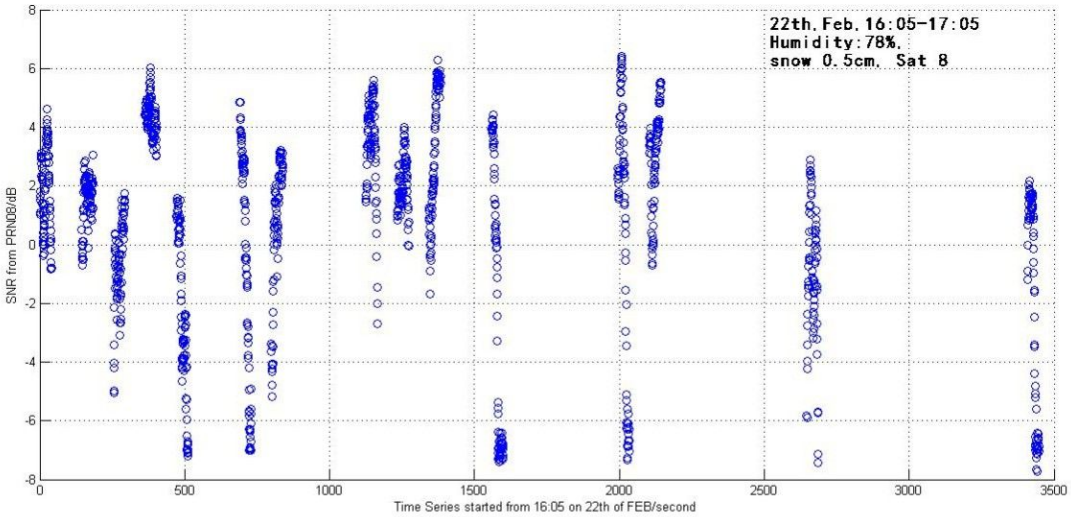

Figure 7-6 SNR of the measurement on 22nd Feb, from 16:05-17:05

What are shown in Figure 7-2 to Figure 7-6 are consecutive 40 s SNR time series, every dot represents the SNR calculated with 500 ms non coherent integration time. Statistics evaluated by grouping each 40 s SNR for all the five measurements are shown in Figure 7-7, which contain information of mean, standard deviation, maximum and minimum value of each time slot.

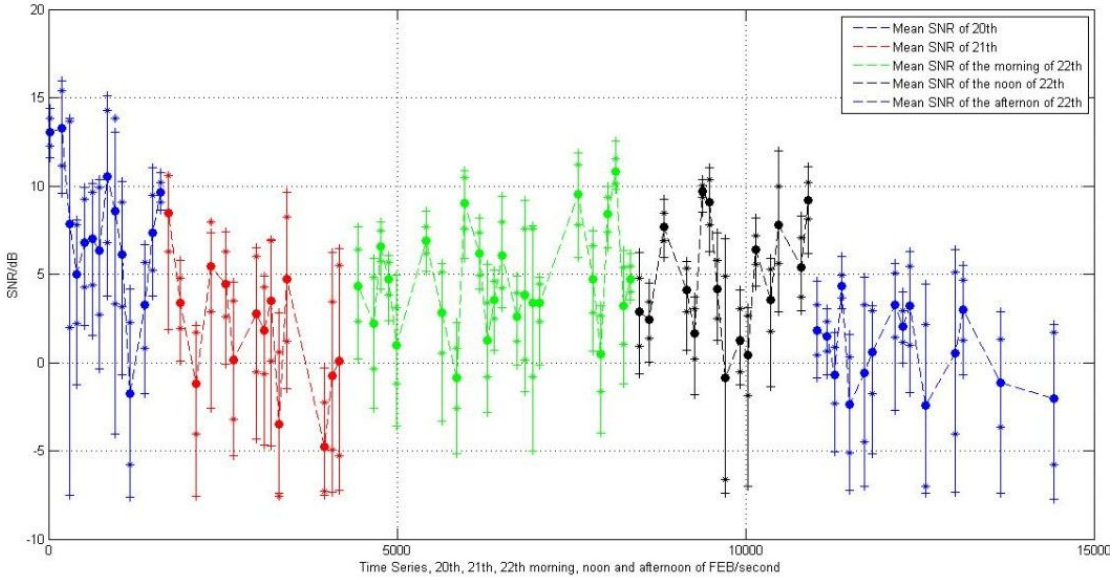

Figure 7-7 Statistics of SNR for the five measurements

As the SNRs have sinusoid-like behavior which can be seen from Figure 7-2 to 7-6, possible interference due to the multipath caused by the buildings was studied using parallel multipath model or two-ray model and the simulated interference frequency was verified to be close to that revealed by FFT of the SNR series. After that, signal amplitude A1 was tried to be extracted from each group of SNR assuming the interference signal had a rotating phase with respect to the specularly reflected signal which lead to this sinusoid-like SNR performance. The signal amplitude A1 was then made a second order polynomial fit with the measured snow depth as shown in Figure 7-8

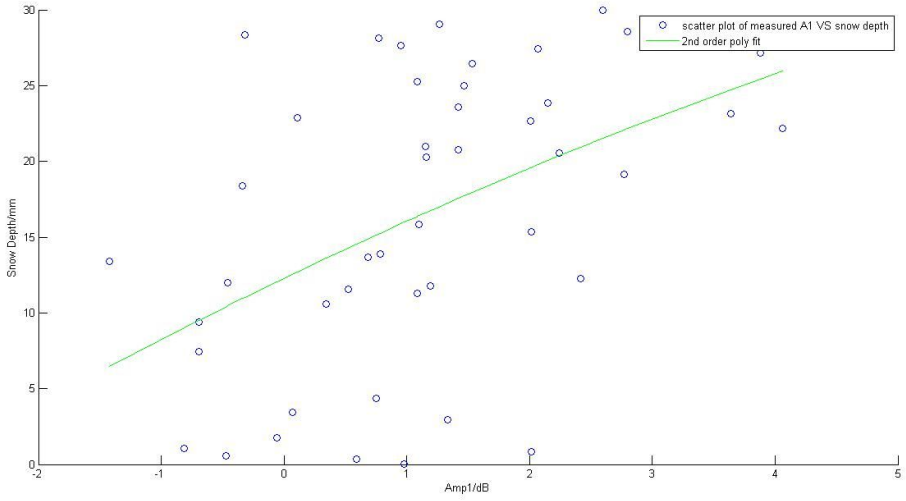

Figure 7-8 Second order polynomial fit between reflected signal amplitude and snow depth

Comments should be made here that the study was not rigorous and the data availability was limited. It was just a trial measurement aiming at observing the effect of snow to the reflected LHCP SNR. The sinusoid-like behavior of SNR could either be caused by multipath of buildings as illustrated above or could be brought by the interaction of the GPS signal with the snow layer (see [Rodriguez-Alvarez, 2011(b)], [Gutmann, 2012]). The polynomial fit shown in Figure 7-8 didn't seem well matched and the research on snow depth was interrupted due to the insufficient theory exploration and limited data (there is very few snow events). The study of snow depth is not currently focused on and it is temporarily out of the scope of this research. Results shown here can be used as a reference and more rigorous study is expected for the possible future work.

Chapter 8 Summary and future work

8.1 Summary

In this research, mainly two applications utilizing GNSS-R were carried out: the soil moisture retrieval and buried objection detection.

For the soil moisture retrieval, two types of receivers were applied and the compact receiver solution was developed in our group. It was validated to work well through the static measurement results. The receiver was verified to be sensitive to the different soil moisture contents in terms of processed SNR from restored raw data. The first static experiment had three different moisture contents from dry to soaking wet by pouring water eventually to the surface. The second static experiment dealt with increasing wet surface areas. Both of these two experiments showed the received SNR had good sensitivity to different surface conditions also by considering the statistics of SNR, where the mean SNR +/- the standard deviation of SNR for each condition is still separated from each other.

Antennas used for receiving reflected signals were also concerned. The helix LHCP antenna was designed and manufactured, and it was tested in the anechoic chamber. Results showed that the helix antenna could reach the designed goals but due to its big dimension, it was barely used for measurements. Several patch antennas are still in designing phase in order to meet the requirement of cross polarization level. A couple of possible types have been simulated and to be manufactured in the near future. Twin commercial antennas which were bought for the regional project of SMAT-F2 for the cross polarization power ratio (LHCP/RHCP) research on soil moisture were further examined their characterizations in the anechoic chamber since they were suspected to be working in bad manners. Results demonstrated that they didn’t reach the cross polarization level which is strongly required by our application, and the other characterizations are worse than what is reported in the official data sheet.

The signal processing of reflected data for getting SNR (time series) was successfully achieved. It was realized by a software defined radio approach, which

generates the DDM and DW and extracts information from them. The signal power can then be computed given the noise power. Programs for georeferencing specular points on either Google Maps or an *x-y* plane were proved to be useful for planning a static measurement and for showing the results. The fly dynamics was taken into account and studied for a flight measurement, which can compensate the antenna gain variation due to the incident angle changes over time.

The first dielectric constant retrieval algorithm was derived from LHCP reflected signal power, which assumes the surface to be perfectly smooth and neglects the roughness effect. The flight measurement made for rice fields' flooding states detection has shown that processed SNR was sensitive to water/on-water conditions and even to soil moisture changes occurred between flooded field and dry field, field and boundary or road. Before deriving dielectric constant of fields, the system parameters were calibrated first by considering the pure water condition whose dielectric constant is known as around 80 when the signals were reflected by Lake Viverone. Results of dielectric constant obtained after the calibration process showed the similar results as been revealed by SNR. Dielectric constant was checked to be reasonable by comparing the results with the real time images taken by the onboard co-located video camera. However, due to the lack of in-situ measurement on soil moisture, the results could not be further evaluated.

The second dielectric constant retrieval algorithm applied the dual polarization (LHCP and RHCP) receptions of reflected signals simultaneously to make the ratio between the cross polarization powers. Retrieval process was done for specular reflection and diffuse scattering including three widely used models: KGO, KPO and SPM. All the final derived expressions clarified that the cross polarization power ratio is dependent on only dielectric constant and incident angle, with the surface roughness term eliminated. It proves the idea that by making the ratio between LHCP and LHCP, roughness effect can be neglected. Another important conclusion obtained through the simulation results was that the expressions of cross polarization ratio for the three scattering models and for the specular reflection case turned out to be unified, which means that for the LHCP and RHCP receiving scheme, an identical equation can be used for solving dielectric constant no matter what the surface roughness is or what the scattering model is applied.

An innovative idea of detecting buried metal object using GNSS-R was brought

and tested in this research. The receiver scheme is the same as the single LHCP solution for soil moisture retrieval, and the indicator is the processed SNR of reflected signals. The first static measurement verified the sensitivity of SNR to the presence of metal object on or under a few centimeters of the surface, even in a wet soil condition. The second measurement was a simulated flight measurement, which not only detected the presence of metal object, but also provided the possibility to evaluate the dimension of the object.

An attempt to relate the reflected LHCP signal SNR to snow depth was also carried out and a second order polynomial fit was implemented. However, due to the limited data and theory support, and even possible multipath interference, the research in this field was interrupted.

8.2 Future work

The future work relating to soil moisture covers hardware, software and algorithm aspects. A reliable LHCP and RHCP dual polarization patch antenna is to be manufactured and tested, which is expected to have low cross polarization level. Also in cooperation with ISMB and NAVSAS Group in the framework of SMAT-F2 project, a new scatterometer is under development, which is specifically designed to be small and lightweight, and to be mounted on board a UAV. It is characterized by the use of low-cost equipment, enabling, at the same time, a flexible and reconfigurable solution thanks to the use of a software defined radio technology [Gamba, 2013]. Post processing programs are therefore required an update according to the on board signal processing level. Both of the retrieval algorithms for LHCP scheme and LHCP/RHCP scheme are going to be verified in a better controlled condition, especially for the later one. For the cross polarization ratio method, multiple variables need to be changed and controlled, such as incident angle, soil moisture content, surface roughness in order to compare with the simulation results. Several flight measurements equipping the new scatterometer are foreseen to be done in the upcoming months, and retrieved dielectric constant will be compared with the in-situ measurements.

The altimetry study utilizing GNSS-R is now starting. Theoretical research has begun and eventually altimetry measurements will be done using code delay and

carrier phase delay methods. Snow depth detection is another research interest which can be done in the mountain region with a lot of snow coverage, and to establish the relationship between received reflected signal and snow depth.

References

Antcom Corperation, www.antcom.com

P. Beckmann and A. Spizzichino, "The scattering of electromagnetic waves from rough surfaces," *Artech House*, Norwood, MA, 1963.

G. Berginc, "Small-slope approximation method: a further study of vector wave scattering from two-dimensional surfaces and comparison with experimental data," *Progress In Electromagnetics Research*, vol. 37, pp. 251-287, 2002.

E. Cardellach, G. Ruffini, D. Pino, A. Rius, A. Komjathy, and J. L. Garrison, "Mediterranean balloon experiment: ocean wind speed sensing from the stratosphere, using GPS reflections," *Remote Sensing of Environment*, vol. 88, no. 3, pp. 351-362, 2003.

E. Cardellach and A. Rius, "A new technique to sense non-Gaussian features of the sea surface from L-band bi-static GNSS reflections," *Remote Sensing of Environment*, vol. 112, no. 6, pp. 2927-2937, 2008.

E. Cardellach, F. Fabra, O. Nogues-Correig, S. Oliveras. S. Ribo, and A. Rius, "GNSS-R ground-based and airborne campaigns for ocean, land, ice, and snow techniques: application to the GOLD-RTR data set," *Radio Science*, vol. 46, RS0C04, doi:10.1029/2011RS004683, pp. 1-16, 2011.

E. Ceraldi, G. Franceschetti, A. Iodice, D. Riccio, and G. Ruello, "On the use of the specular direction copolarised ratio for the retrieval of soil dielectric constant," *in Proc. IGARSS*, pp. 4144-4146, 2003.

E. Ceraldi, G. Franceschetti, and D. Riccio, "Estimating the soil dielectric constant via scattering measurements along the specular direction," *IEEE Trans. Geosci. Romote Sens.*, vol. 43, no. 2, pp. 295-305, 2005.

J. Dampf, T. Pany, N. Falk, B. Riedl, and J. Winkel, "Galileo altimetry, using AltBOC and RTK techniques," *Inside GNSS*, vol. 8, no. 1, pp. 54-63. 2013.

S. Dawoud, “GNSS principles and comparison,” *Potsdam University*, 2012.

R. D. De Roo and F. T. Ulaby, “Bistatic specular scattering from rough dielectric surfaces,” *IEEE Transactions on Antennas and Propagation*, vol. 42, no. 2, pp. 220-231, 1994.

Developer Shop by Miniand, Hackberry A10 Dev Board, https://www. miniand .com/products/Hackberry%20A10%20Developer%20Board

M. C. Dobson and F. T. Ulaby, “Microwave Dielectric Behavior of Wet Soil-Part II:Dielectric Mixing Models,” *IEEE Trans. Geosci. Romote Sens.*, vol. GE-23, no. 1, pp. 35-46, 1985.

M. C. Dobson and F. T. Ulaby, “Active microwave soil moisture research,” *IEEE Transactions on geosciences and remote sensing*, no. 1, pp. 23-36, 1986.

A. Egido, M. Caparrini, G. Ruffini, S. Paloscia, E. Santi,L. Guerriero, N. Pierdicca and N. Floury, “Global navigation satellite systems reflectometry as a remote sensing tool for agriculture,” *Remote Sens.*, no. 4, pp. 2356-2372, 2012.

M. Fantino, A. Molino, P. Mulassano, M. Nicola, and M. Pini, “N-Gene: A GPS and Galileo fully software receiver,” *Proceedings of SDR-Italy’09 Workshop - From Software Defined Radio to Cognitive Networks*, Pisa, Italy, 2-3 July 2009.

P. Ferrazzoli, L. Guerriero, N. Pierdicca, and R. Rahmoune, “Forest biomass monitoring with GNSS-R: theoretical simulations,” *Advances in Space Research*, 10.1016/j.asr.2010.04.025, 2010.

F. Frezza, P. Martinelli, L. Pajewski, and G. Schettini, “Short-pulse electromagnetic scattering by buried perfectly conducting cylinders,” *IEEE Geosci. Remote Sens. Lett.*, vol. 4, no. 4, pp. 611–615, 2007.

A. Fung, “Microwave scattering and emission models and their applications,” *Artech House*, 1994.

M. T. Gamba, S. Ugazio, Y. Pei, L. L. Presti, R. Notarpietro, M. Pini, and P. Savi. “A new SDR GNSS receiver prototype for reflectometry applications: ideas and design,” *In proceeding of 4th International Colloquium Scientific and Fundamental*

Aspects of the Galileo Programme. Prague, Czech Republic, pp. 1-8, Dec 4-6, 2013.

J. L. Garrison, S. J. Katzberg, and M. I. Hill, "Effect of sea roughness on bistatically scattered range coded signals from the global positioning system," *Geophysical Research Letters*, vol. 25, pp. 2257-2260. 1998.

J. L. Garrison, and S. J. Katzberg, "The application of reflected GPS signals to ocean remote sensing," *Remote Sensing of Environment*, vol. 73, pp.175-187, 2000.

J. L. Garrison, A. Komjathy, V. U. Zavorotny, and S. J. Katzberg, "Wind speed measurement using forward scattered GPS signals," *IEEE Transactions on Geoscience and Remote Sensing*, vol. 40, pp. 50-65, 2002.

S. Gleason, S. Hodgart, Y. Sun, C. Gommenginger, S. Mackin, M. Adjrad, and M. Unwin, "Detection and processing of bistatically reflected GPS signals from low earth orbit for the purpose of ocean remote sensing,", *IEEE Transactions on Geoscience and Remote Sensing*, vol. 43, no. 6, pp. 1229-1241, 2005.

S. T. Gleason, "Remote sensing of ocean, ice and land surfaces using bistatically scattered GNSS signals from low earth orbit," *PhD Thesis. University of Surrey*. 2006.

Glenn Research Center, "Aircraft rotations, body axes," http://www.grc.nasa.gov/WWW/K-12/airplane/rotations, 2014.

GNSS @ Colorado Center for Astrodynamics Research, http://ccar.colorado.edu/gnss/

Google Maps API, https://developers.google.com/maps/

T. Grelier, A. Ghion, J. Dantepal, L. Ries, A. DeLatour, J. L. Issler, and G. W. Hein,. "Compass signal structure and first measurements," *In ION GNSS*, vol. 2007, pp. 3015-3024, 2007.

H. D. Griffiths, "Bistatic and multistatic radar," *University College London Dept. Electronic and Electrical Engineering*, 2004.

P. D. Groves, "Principles of GNSS, inertial and multisensory integrated navigation systems," *Artech House*, boston|London, 2008.

E. D. Gutmann, K. M. Larson, M. W. Williams, F. G. Nievinski, and V. Zavorotny, "Snow measurement by GPS interferometric reflectometry: an evaluation at Niwot Ridge," *Colorado.Hydrological Processes*, vol. 26, no. 19, pp. 2951-2961, 2012.

M. T Hallikainen, F. T. Ulaby, and M. C. Dobson, "Microwave dielectric behavior of wet soil-part 1: empirical models and experimental observations," *IEEE Trans. Geosci. Romote Sens.*, vol. GE-23, no. 1, pp. 25-34, 1985.

C. Hall and R. Cordey, "Multistatic scatterometry," *Proc. IEEE Int. Geosci. Remote Sensing Symp.*, Edinburgh, Scotland, 13-16 Sept. pp. 561-562, 1988.

A. Helm, "Ground-based GPS altimetry with the L1 OpenGPS receiver using carrier phase delay observations of reflected GPS signals," *Scientific Technical Report/Deutsches Geoforschungszentrum Potsdam GFZ*, 2008.

Japan Association of Remote Sensing, http://wtlab.iis.u-tokyo.ac.jp/~wataru/lecture/rsgis/rsnote/cp3/cp3-4.htm, 1996.

Y. Jia, "Characterizations of GNSS-R antennas," *SMAT-F2 Activity Report*, 2014.

S. Jin and A. Komjathy, "GNSS reflectometry and remote sensing: New objectives and results," *Advances in Space Research*, vol. 46, pp. 111-117, 2010.

S. Jin, G. P. Feng, and S. Gleason, "Remote sensing using GNSS signals: Current status and future directions," *Advances in Space Research*, vol. 47, pp.1645-1653, 2011.

S. Jin, E. Cardellach, and F. Xie, "GNSS remote sensing: Theory, methods and applications," *Springer*, 2014.

S. J. Katzberg and J. L. Garrison Jr. "Utilizing GPS to determine ionospheric delay over the ocean," *National Aeronautics and Space Administration*, Langley Research Center, 1996.

S. J. Katzberg, O. Torres, M. S. Grant, and D. Masters, "Utilizing calibrated GPS reflected signals to estimate soil reflectivity and dielectric constant: Results from SMEX02," *Remote Sens. of Environment*, no. 100, pp. 17-28, 2005.

E. F. Knott, J. Shaeffer, and M. Tuley, "Radar cross section," *SciTech Publishing*, 2004.

E. F. Knott, “Radar cross section measurements,” *SciTech Publishing*, 2006.

K. M. Larson, J. J. Braun, E. E. Small, V. U. Zavorotny,E. D. Gutmann, and A. L. Bilich, “GPS multipath and its relation to near-surface soil moisture content,” *IEEE Journal of Selected Topics in Applied Earth Observations and Remote Sensing*, vol. 3, no. 1, pp. 91-99. Mar 2010.

S. T. Lowe, C. Zuffada, Y. Chao, P. Kroger, L. E. Young, and J. L. LaBrecque, “5-cm-precision aircraft ocean altimetry using GPS reflections,” *Geophysical Research Letters*, vol. 29, no. 10, 13-1, 2002.

J. F. Marchán-Hernández, N. Rodríguez-Álvarez, A. Camps, X. Bosch-Lluis, I. Ramos-Pérez, and E. Valencia, “Correction of the sea state impact in the L-band brightness temperature by means of delay-Doppler maps of global navigation satellite signals reflected over the sea surface,” *IEEE Transactions on Geoscience and Remote Sensing*, vol. 46, no. 10, pp. 2914-2923, 2008.

M. Martin-Neira, “A passive reflectometry and interferometry system (PARIS): Application to ocean altimetry,” *ESA Journal*, vol. 17, pp. 331-355, 1993.

M. Martín-Neira, M. Caparrini, J. Font-Rossello, S. Lannelongue, and C. S. Vallmitjana, “The PARIS concept: an experimental demonstration of sea surface altimetry using GPS reflected signals,” *IEEE Transactions on Geoscience and Remote Sensing*, vol. 39, no. 1, pp. 142-150, 2001.

D. Masters, P.Axelrada, and S.Katzberg, “Initial results of land-reflected GPS bistatic radar measurements in SMEX02,” *Remote Sens. of Environment*, no. 92, pp. 507-520, 2004.

V. L. Mironov,L. G. Kosolapova, and S. V. Fomin, “Physically and mineralogically based spectroscopic dielectric model for moist soils,” *IEEE Trans. Geosci. Romote Sens.*, vol. 47, no. 7, pp. 2059-2070, Jul 2009.

V. L. Mironov, S. V. Fomin, K. V. Muzalevskiy, A. V. Sorokin, and M. I. Mikhaylov, “The use of navigation satellites signals for determination the characteristics of the soil and forest canopy,” *in Proc. IGARSS*, pp. 7527-7529, 2012(a).

V. L. Mironov and K. V. Muzalevskiy, “The new algorithm for retrieval of soil moisture and surface roughness from GNSS reflectometry,” *in Proc. IGARSS*, pp. 7530-7532, 2012(b).

P. Misra and P. Enge. “Global positioning system: signals, measurements, and performance,” *Ganga Jamuna Press*, ISBN 0-9709544-0-9, 2001.

E. G. Njoku and J. A. Kong, “Theory for passive microwave remote sensing of near-surface soil moisture,” *J. Geophys. Res.*, vol. 82, pp. 3108-3118, 1977.

E. Njoku, and P. O’Neill, “Multifrequency radiometer measurements of soil moisture,” *IEEE Trans. Geosci. Romote Sens.*, vol. GE-20, no. 4, pp. 468-475, Oct 1982.

E. G. Njoku and D. Entekhabi, “Passive microwave remote sensing of soil moisture,” *Journal of Hydrology*, vol. 184, pp. 101-129, 1996.

M. Nolan and D. R. Fatland, “Penetration depth as a DInSAR observable and proxy for soil moisture,” *IEEE Trans Geoscience and Remote Sensing*. vol. 41, pp. 532-537, 2003.

S. Perrin, E. Duflos, P. Vanheeghe, and A. Bibaut,” Multisensor fusion in the frame of evidence theory for landmines detection,” *IEEE Trans System, Man and Cybernetics-Part C Appl Rev*., vol. 34, no.4, pp. 485-498, 2004.

N. Pierdicca, L. Guerriero, R. Giusto, M. Brogioni, A. Egido, and N. Floury, “GNSS reflections from bare and vegetated soils: Experimental validation of an end-to-end simulator,” *in Proc. IGARSS*, pp.4371-4374, 2011.

M. Piles, M.Vall-llossera, A. Camps, M.Talone and A.Monerris, “Analysis of a least-squares soil moisture retrieval algorithm from L-band passive observations,” *Remote Sens.*, vol. 2, pp.352-374, 2010.

N. Pinel and C. Boulier, “Electromagnetic wave scattering from random rough surfaces: asymptotic models,” *ISBN: 978-1-118-57946-6*, *Wiley-ISTE*, 2013.

T. Ren, “Global Navigation Satellite System (GNSS) Reflectometry for moisture retrieval applications: antennas design,” *Master Thesis*, Politecnico di Torino, 2012.

A. Rius, J. M. Aparicio, and E. Cardellach, “Sea surface state measured using GPS reflected signals,” *Geophysical research letters*, vol. 29, no. 23, 2122, doi:10.1029/2002GL015524, pp. 1-4, 2002.

N. Rodriguez-Alvarez, X. Bosch-Lluis, and A. Camps, “Soil moisture retrieval using GNSS-R techniques: experimental results over a bare soil field,” *IEEE Trans. Geosci. Romote Sens.*, vol. 47, no. 11, pp. 3616-3624, 2009.

N. Rodriguez-Alvarez, X. Bosch-Lluis, A. Camps, A. Aguasca, M. Vall-llossera, E. Valencia, I. Ramos-Perez, and H. Park, “Review of crop growth and soil moisture monitoring from a ground-based instrument implementing the Interference Pattern GNSS-R Technique,” *Radio Science*, vol. 46, pp. RS0C03, 2011(a).

N. Rodriguez-Alvarez, A. Aguasca, E. Valencia, X. Bosch-Lluis, I. Ramos-Perez, H. Park, and M. Vall-Llossera, “Snow monitoring using GNSS-R techniques,” *In 2011 IEEE Geoscience and Remote Sensing Symposium (IGARSS)*, pp. 4375-4378, July, 2011(b).

N. Rodriguez-Alvarez, X. Bosch-Lluis, A. Camps, A. Aguasca, M. Vall-Llossera, E. Valencia, I. Ramos-Perez, and H. Park, “Review of crop growth and soil moisture monitoring from a ground-based instrument implementing the Interference Pattern GNSS-R technique,” *Radio Science*, vol. 46, RS0C03, pp. 1-11, 2011(c).

N. G. Ruffini, F. Soulat, M. Caparrini, O. Germain, and M. Martín-Neira, “The Eddy experiment: accurate GNSS-R ocean altimetry from low altitude aircraft,” *Geophysical research letters*, vol. 31, no. 12, 2004.

E. E. Small, K. M. Larson, and J. J. Braun, “Sensing vegetation growth with reflected GPS signals,” *Geophysical research letters*, vol. 37, L12401, pp. 1-5, 2010.

D. Stillman, “Plotting surveying data in Google Earth,” *http://code.google.com/p/google-earth-plotter/*, 2009.

F. Ticconi, L. Pulvirenti, and N. Pierdicca, “Models for scattering from rough surfaces,” *Electromagnetic Waves*, vol. 10, pp. 203-226, 2011.

G. C. Topp, J. L. Davis, and A. P. Annan, “Electromagnetic determination of soil water content: measurements in coaxial transmission lines,” *Water Resour. Res.*, vol. 16, pp. 547-582, 1980.

L. Tsang, J. A. Kong, and K. H. Ding, “Electromagnetic waves, theories and applications,” *Jon Wiley and Sons*, New York, 2000.

L. Tsang and J. A. Kong, “Scattering of electromagnetic waves, advanced topics,” *Jon Wiley and Sons*, New York, 2001.

F. T. Ulaby, R. K. Moore, and A. K. Fung, “Microwave remote sensing: Active and passive, vol. 2,” *Addison-Wesley*, Reading, Massachusetts, 1982.

F. T. Ulaby and E. A. Wilson, “Microwave attenuation properties of vegetation canopies,” *IEEE Trans Geoscience And Remote Sensing.*, vol. GE-23, no. 5, 1985.

F. T. Ulaby, R. K. Moore, and A. K. Fung, “Microwave remote sensing: active and passive”, *Addison Wesley*, vol. 3. 1986.

Y. Urlichich,. V. Subbotin, G. Stupak, V. Dvorkin, A. Povalyaev, S. Karutin, and R. Bakitko, “GLONASS modernization,” *GPS World*, vol. 22, no. 11, pp. 34-39, 2011.

A. G. Voronovich, “Non-local small-slope approximation for wave scattering from rough surfaces,” *Waves in Random Media*, vol. 6, no. 2, pp. 151-168, 1996.

W. Wan, X. Chen, L. Zhao, J. Zhang, and H. Xiao, “Near-surface soil moisture content measurement by GNSS reflectometry: An estimation model using calibrated GNSS signals,” *in Proc. IGARSS*, pp. 7523-7526, 2012.

J. R. Wang and T. J. Schmugge, “An empirical model for the complex dielectric permittivity of soils as a function of water content,” *IEEE Trans. Geosci. Romote Sens.*, vol. GE-18, no. 4, pp. 288-295, Oct 1980.

V. U. Zavorotny and A. G. Voronovich, “Bistatic GPS signal reflections at various polarizations from rough land surface with moisture content,” *In Proc. IEEE Geoscience and Remote Sensing Symposium*, Honolulu, HI, USA, 24-28 July 2000, vol. 7, pp. 2852-2854, 2000(a).

V. U. Zavorotny and A. G. Voronovich, “Scattering of GPS signals from the ocean with wind remote sensing application,” *IEEE Transactions on Geoscience and Remote Sensing*, vol. 38, no. 2, pp. 951-964, March 2000(b).

V. U. Zavorotny, K. M. Larson, J. J. Braun, E. E. Small, E. D. Gutmann, and A. L. Bilich, “A physical model for GPS multipath caused by land reflections: toward bare soil moisture retrievals,” *IEEE Journal of selected topics in applied earth observations and remote sensing*, vol. 3, no. 1, pp. 100-110, Mar 2010.